INFORMATION TO USERS

This manuscript has been reproduced from the microfilm master. UMI films the text directly from the original or copy submitted. Thus, some thesis and dissertation copies are in typewriter face, while others may be from any type of computer printer.

The quality of this reproduction is dependent upon the quality of the copy submitted. Broken or indistinct print, colored or poor quality illustrations and photographs, print bleedthrough, substandard margins, and improper alignment can adversely affect reproduction.

In the unlikely event that the author did not send UMI a complete manuscript and there are missing pages, these will be noted. Also, if unauthorized copyright material had to be removed, a note will indicate the deletion.

Oversize materials (e.g., maps, drawings, charts) are reproduced by sectioning the original, beginning at the upper left-hand corner and continuing from left to right in equal sections with small overlaps.

Photographs included in the original manuscript have been reproduced xerographically in this copy. Higher quality 6" x 9" black and white photographic prints are available for any photographs or illustrations appearing in this copy for an additional charge. Contact UMI directly to order.

ProQuest Information and Learning
300 North Zeeb Road, Ann Arbor, MI 48106-1346 USA
800-521-0600

MOLECULAR DYNAMICS SIMULATION OF UNIAXIAL EXTENSIONAL DEFORMATION OF NEWTONIAN AND NON-NEWTONIAN LIQUID BRIDGES

by

Borislav Busic

A dissertation submitted to the Graduate Faculty in Physics in partial fulfillment of the requirements for the degree of Doctor of Philosophy,The City University of New York

2001

This manuscript has been read and accepted for the Graduate Faculty in Physics in satisfaction of the dissertation requirement for the degree of Doctor of Philosophy.

9/4/01
Date

Professor Joel Koplik
Chair of Examining Commitee

9/4/01
Date

Professor Louis S. Celenza
Executive Officer

Examining Commitee

Professor Andreas Acrivos _____

Professor Morton Denn _____

Professor Jimmy Feng _____

Professor Boris Khusid _____

The City University of New York

MOLECULAR DYNAMICS SIMULATION OF UNIAXIAL EXTENSIONAL DEFORMATION OF NEWTONIAN AND NON-NEWTONIAN LIQUID BRIDGES

by

Borislav Busic

Advisor: Professor Joel Koplik

Abstract

The extensional rheology of Newtonian and non-Newtonian fluids is investigated by molecular dynamics simulations of appropriate model liquids in an extending liquid bridge configuration. The fluids are modeled as molecular species and the polymers as chains of monomers bonded by non-linear springs, both interacting with atomistic solid walls. In the simulations, a cylinder of liquid is placed between solid end-plates which separate at an exponentially increasing rate until the liquid breaks up. A quantitative description of the time evolution of the liquid filament profile and the forces exerted on the end-plates is obtained and can be directly compared to experiment. In addition, monitoring of the atomic displace-

ments and forces during simulation yields information on the internal dynamics of the fluid - the velocity and stress fields, and the molecular configurations. The simulations are in good agreement with laboratory data and with the results of macroscopic numerical simulations of the device based on appropriate rheological models. In particular, in the range of deformations up to Hencky strains of $\varepsilon \approx 0.7$, the dynamic response of the model liquids is well described by a lubrication approximation of Newtonian "reverse squeeze flow". Alignment of polymer chains in the model solution leads to strain-hardening of the filament manifested in a very uniform deformation of the filament over most of the flow regime. The stress fields are both spatially and temporally nonhomogeneous with characteristic layers of high stresses.

Acknowledgements

I would like to express gratitude to my adviser Professor Joel Koplik for his support and the members of the examining commitee for their time and valuable suggestions for the final version of the thesis.

Table of Contents

1 Introduction 1

1.1 Extensional Flow Experiments 3

1.2 Relevant previous Results 9

1.3 Plan of the Thesis 17

2 Model Fluids 20

2.1 Formulation of Model Fluids 21

2.2 Characterization of Model Fluids 31

2.2.1 Surface Tension 31

2.2.2 Shear Viscosity and Normal Stress Coefficients 37

3 Molecular Dynamics Simulation 48

3.1 Preparation of Initial Liquid Bridge Configurations 48

3.2 Geometric Description and Deformation Strategy 50

3.3 Dimensionless Groups 54

3.4 Liquid-Wall Interface 56

3.5 Numerical Algorithm 66

4 Measurement and Calculation Procedures 69

4.1 Sampling and Approximation of Simulation Data 71

4.2 Shape and Minimum Radius of Fluid Filaments 74

4.3 Pressure Tensor 76

4.4 Trouton Ratio 81

5 Results 85

5.1 MODEL NEWTONIAN LIQUID 85

5.1.1 Filament Shape Deformation 85

5.1.2 Force on the End-plates 89

5.1.3 Axial Flow Kinematics 91

5.1.4 Stress Distribution 93

5.1.5 Elongational Viscosity 98

5.2 MODEL SOLUTION 100

5.2.1 Velocity Field 104

5.2.2 Stress Field 105

5.2.3 Transient Elongational Viscosity 110

5.3 MODEL MELTS 112

5.3.1 Stress Fields 118

5.3.2 Elongational Viscosity 124

5.4 Flow Reversal in Uniaxial Stretching Experiment 125

6 Conclusions **129**

References **133**

List of Tables

2.1 Lennard-Jones units 23

2.2 Material properties of the model fluids 47

3.1 Nondimensional groups for typical filament stretching simulations 56

List of Figures

1.1 Uniaxial extension in liquid bridge configuration 4

2.1 Shifted Lennard-Jones potentials 27

2.2 Basic bond potential 27

2.3 FENE potential used with the polymer chains in the dilute solution model liquid. 30

2.4 Molecular dynamics liquid-vapor configuration and corresponding pressure distributions 35

2.5 Lees-Edwards periodic boundary conditions for planar Couette flow. 39

2.6 The calculation of the statistical inefficiency 43

2.7 Steady shear flow material functions for the model fluids 44

3.1 Schematic of the molecular dynamics liquid bridge configuration . 51

3.2 Layered liquid structure at the liquid-solid interface 57

3.3 Temporal and radial variation of the liquid-wall force for the polydisperse melt filament in equilibrium 59

3.4 Influence of the slip at the liquid-solid interfaces on the liquid filament deformation in the filament stretching simulation. 62

3.5 Velocity of the end-plates *vs.* Hencky strain. 64

3.6 Liquid-wall force *vs.* Hencky strain for different structures of liquid-wall interfaces in a case of polydisperse melt filament stretching simulation 65

4.1 Smoothing approximation for the radial distribution of the liquid-wall force 73

4.2 Determination of the shape of a filament 76

4.3 Symmetries of the filament stretched by simultaneous motion of both end-plates and associated transformation of quantities defining the configurational part of the pressure tensor. 79

4.4 An illustration of the results of stress field data analysis 80

5.1 Instantaneous configurations of the N=4 liquid filament 86

5.2 Minimum radius variation for Newtonian filament 87

5.3 Dependence of the Newtonian filament shape deformation on stretching rate 88

5.4 The force on the end-plates in Newtonian simulations 90

5.5 Radial variation of the force on the end-plates 91

5.6 Axial velocity profiles for the Newtonian filament 92

5.7 Distribution of the isotropic stress within Newtonian filament . . . 94

5.8 Distribution of the shear stress within Newtonian filament 96

5.9 Distribution of the radial component of the extra pressure tensor within Newtonian filament 97

5.10 Distribution of the axial component of the extra stress tensor within Newtonian filament 97

5.11 Distribution of the normal stress difference within Newtonian filament 97

5.12 Elongational stress growth coefficient for the Newtonian model fluid 98

5.13 Instantaneous configurations of the solution filament 100

5.14 Minimum radius *vs.* Hencky strain for the solution filament 101

5.15 The force on the end-plates in the solution simulations. 102

5.16 Axial velocity profiles for the solution filament 104

5.17 Distribution of the isotropic stress within the solution filament . . . 106

5.18 Distribution of the shear stress within the solution filament 107

5.19 Normal components of the total extra stress tensor within the solution filament 108

5.20 Normal components of the total extra stress tensor and normal stress difference within the solution filament 109

5.21 Variation of the axial component of the total extra stress tensor $-\pi_{zz}$ along the axis of the solution filament. 109

5.22 Elongational stress growth coefficient for the model solution 110

5.23 Instantaneous configurations of the polydisperse melt filament . . 112

5.24 Instantaneous configurations of the monodisperse melt filament . . 113

5.25 Minimum radius variation for the melt filaments 114

5.26 Axial velocity profiles for the polydisperse melt 115

5.27 Tensile force *vs.* Hencky strain for model melts 116

5.28 Isotropic stress within melt filaments 119

5.29 Shear stress within melt filaments 120

5.30 Axial component of the total extra stress tensor within melt filaments 121

5.31 Radial component of the total extra stress tensor within melt filaments 122

5.32 Normal stress difference within melt filaments 123

5.33 Trouton ratio for the model melts 124

5.34 Velocity fields inside monatomic fluid undergoing uniform stretching 126

5.35 Velocity fields inside monatomic fluid undergoing a constant imposed stretching rate deformation 127

1 Introduction

Polymeric liquids, both in solutions and melts, have very different flow properties than simple liquids whose response to flow deformations is dominated by a single material property, the Newtonian viscosity. In addition to being viscous, a large majority of industrially and biologically important polymeric fluids exhibit properties, in particular elasticity, which lead to highly nonlinear behavior in common flow situations. Consequently these fluids are termed non-Newtonian and their rheological characterization generally requires a set of material *functions* which generally depend on deformation rates and time [1]. In the most common cases, shear flow deformations for example, in contrast to simple liquids the polymeric fluids exhibit a viscosity dependent on both the rate of deformation and imposed strain. Moreover normal stress differences, which are absent in the shear flows of Newtonian fluids, are present. In simple, steady shear flow these effects can be characterized with three material functions, the non-Newtonian viscosity and two normal stress coefficients. Furthermore the material properties charac-

terizing the response of non-Newtonian fluids to shear-free deformations are not immediately related to their shear properties, and have to be determined from the corresponding flow configurations. Among these, the extensional properties of polymeric liquids are of prominent importance for both practical and more fundamental reasons. The extensional component is dominant in many industrial processes, such as fiber spinning, extrusion, film blowing or blow molding. Extensional material functions are needed to model these flows and to discriminate between the numerous constitutive models of non-Newtonian behavior in the literature [2]. However, due to difficulties stemming from the very nature of the extensional flows the extensional properties of non-Newtonian fluids are not as nearly well understood as their shear properties. The experimentally accessible flow geometries are predominantly but not exclusively extensional, and generally do not allow unambiguous determination of the extensional material functions. Therefore, in order to be reliably interpreted, the experimental measurements of the extensional properties of non-Newtonian fluids have to be complemented by additional investigations of underlying dynamics. In this respect the numerical simulations of constitutive models play a crucial role. Besides elucidating the underlying dynamics of a particular process these simulations give a better understanding of models themselves. However the choice of the constitutive model generally depends on the particular liquid used in the experiment and sometimes different models may lead to contradictory results.

In this work we approach this task in a more general and more fundamental way by using microscopic molecular dynamics techniques (Allen and Tildesley (1987) [3]) to simulate a particular measurement technique of extensional properties of liquids which is based on uniaxial stretching of initially cylindrical liquid bridges and initiated by the work of Sridhar *et al.* (1991) [4]. In molecular dynamics, different liquids are simulated by an appropriate choice of the interaction potential energy between classical atoms, which represent the basic constituents of the liquid system, and the physical or rheological properties of interest are calculated directly from atomic trajectories. In this way the simulation of any Newtonian or non-Newtonian, liquid is approached in an unbiased manner. Moreover the molecular dynamics simulations offer an insight into microscopic processes which can not be easily studied by continuum modeling.

1.1 Extensional Flow Experiments

The experimental configuration investigated in this work is designed for the measurement of uniaxial elongational properties of liquids. Essentially, the experiment is an adaptation of a standard tensile test used for solids, in which an initially cylindrical liquid bridge configuration, consisting of a liquid filament attached to movable circular end-plates, is stretched by an appropriate motion of the end-plates (Fig. 1.1). The relevant flow kinematics are best described in cylindrical

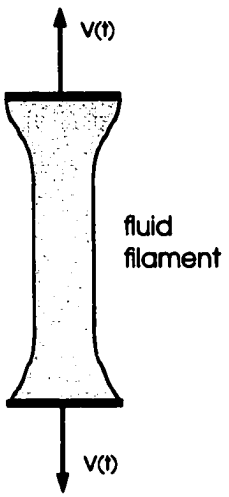

FIGURE 1.1: An initially cylindrical fluid filament during uniaxial extension in the filament stretching device.

coordinates

$$u_z = \dot{\varepsilon}_0 z, \qquad u_r = -\frac{1}{2}\dot{\varepsilon}_0 r, \qquad u_\varphi = 0. \tag{1.1}$$

where $\dot{\varepsilon}_0$ is a constant, the rate of elongation. In such a velocity field the length of a material cylinder ostensibly increases exponentially

$$L(t) = L_0 e^{\dot{\varepsilon}_0 t} \tag{1.2}$$

while its radius decreases exponentially at half the rate

$$R(t) = R_0 e^{-\frac{1}{2}\dot{\varepsilon}_0 t} \tag{1.3}$$

These expressions indicate both the motivation for the experimental design and the fundamental difficulty in experimental treatment of the flow. In this flow the streamlines converge rapidly and high strains are associated with very thin samples. In practice this means that steady stress state most often can not be reached before the sample deforms non-uniformly or ruptures. The appropriate material function for characterization of transient stress in this flow is the *elongational stress growth function* [1],

$$\eta_e^+(\dot{\varepsilon}_0, \varepsilon) = -\frac{\pi_{zz} - \pi_{rr}}{\dot{\varepsilon}_0} \tag{1.4}$$

where π_{zz} and π_{rr} are the normal components of the total extra pressure tensor and

$$\varepsilon = \dot{\varepsilon}_0 t = \ln \frac{L(t)}{L_0} \tag{1.5}$$

is an appropriate strain measure, usually called the Hencky strain.

The desired flow kinematics given in eq. (1.1) generally cannot be fully realized experimentally because of the need for solid boundaries that support any flow geometry in external gravitational field. The no-slip boundary condition at liquid-solid interfaces results in large shear stresses, which in turn prevent generation of purely elongational flows. In the particular case of a liquid bridge configuration, the problem due to presence of the solid end-plates is compounded by the

presence of the free surface interface, which due to no-slip condition at the end-plates deforms non-uniformly as indicated in Fig. 1.1. Furthermore, the presence of gravitational body forces presents additional problems in liquid bridge experiments. In the experimental designs where the configuration is held horizontally, gravity causes sagging of long filaments, while in the designs where the sample is held vertically, gravity may cause non-uniformities in the sample density and shape in the vertical direction. The aforementioned problems are not acute in experiments with very viscous rigid polymer melts, and the liquid bridge technique has been successfully used there for years [5]. However the method had been considered inappropriate for more mobile and less viscous polymer solutions and melts until the work of Matta and Tytus (1990) [6], who showed that in polymer solutions of this type, fluid filaments may be stretched very uniformly provided the end-plates move apart rapidly. In addition, the technique offered an apparently definitive advantage over other available methods for investigation of uniaxial extensional properties of liquids, such as fiber spinning or tubeless siphon (Fano) flow. The latter offers predominantly extensional flows which are steady in the Eulerian but unsteady in the Lagrangian sense, meaning that a liquid particle is subjected to a sequence of deformation regimes,characterized by short residence times, and the extensional results depend greatly on the deformation history of the particle. The apparent advantage of the liquid bridge configuration is that the test sample is deformed from rest. These considerations ignited intensive research

during last decade aimed at design improvements and better understanding of the performance of the device. This work has been motivated and is part of that effort.

The problems originating from the presence of the solid and free surface boundaries and gravitational body forces have been addressed in two essentially different approaches to the design of experiments. In the approach taken by the researchers at the University of Bremen (Germany) [7, 8, 9], the negative influence of the gravitational forces is avoided by carrying out the experiments in microgravity conditions created by free-fall in a drop tower. The non-uniformity of deformation along the filament caused by the no-slip at the fixed end-plates is avoided by use of end-plates with an adjustable diameter. The advantage of this, fundamentally very sound approach is that it can be used for tests of extensional properties of any liquid and any size of the test sample. However only relatively small strains can be achieved due to limitation on the duration of the test imposed by the height of the drop-tower facility and the extent to which the diameter of the end-plates can be reduced. Probably due to these limitations, this method has not been further pursued elsewhere to our knowledge. In the published experiments that involved large liquid bridges with the initial aspect ratio $\Lambda_0 = L_0/2R_0 = 1$ moderate Hencky strains, $\varepsilon \approx 1.4$ were obtained, corresponding to fourfold increase in length and twofold decrease in the radius of the filament.

The other approach initiated by Sridhar and co-workers (1991, 1993) [4, 10] relied initially on a particular deformation pattern exhibited by highly elastic, strain-

hardening, dilute polymer solution filaments. After initial transient these filaments deform in a highly uniform manner indicating the possibility of the formation of a homogeneous uniaxial elongational flow field within the filament. Here gravitational effects are alleviated by using very small test samples (typically $\Lambda_0 \approx 0.3$) and performing the experiment in a neutral buoyancy bath (Plateau tank). The use of small, initially very short test samples is further justified by the strain levels that can be reached: Hencky strains of up to $\varepsilon \approx 6$ have been achieved in this case.

The basic design of the experiment has been adopted and further developed by research groups around the world [11, 12, 13]. Problems with the latter experimental design were recognized from the outset. First, the deformation pattern of a test sample strongly depends on the rheological properties of the fluid. Unlike the constant shear viscosity highly elastic dilute polymer solutions used initially, Newtonian as well as shear thinning, weakly strain-hardening viscoelastic filaments are found to deform non-uniformly throughout stretching. Even in the former case, despite the fact that very long uniformly deformed filaments can be generated over most of the flow regime, the local rate of elongation, determined from the variation of the minimum radius of the filament, never exactly matches the nominal rate of extension corresponding to pure elongational flow within filament and implied in the relative motion of the end-plates. Instead, two distinct regimes of radial deformation are present during stretching experiments [4, 11]. In the first, usually lasting half the duration of the experiment, the local rate of

elongation exceeds the imposed stretching rate significantly (up to 50%) as a consequence of nonuniform necking deformation along the filament. In the second regime, which corresponds to axially uniform deformation of the filament, the rate of thinning is typically smaller (up to 50%) than the overall stretch rate.

1.2 Relevant previous Results

As a part of preparation for their microgravity experiment Kröger *et al.* (1992) [7] systematically investigated liquid bridge device performance in the neutral buoyancy conditions on a fairly large sample of carefully chosen pairs of Newtonian and viscoelastic liquids with matching zero-shear rate viscosities. The liquid filaments were stretched by *uniform* motion of one of the end-plates giving non-constant, monotonically decreasing imposed strain rates,

$$\dot{\varepsilon}(t) = \frac{\dot{\varepsilon}(0)}{1 + \dot{\varepsilon}t} \tag{1.6}$$

these experiments gave valuable insight into relative importance of inertial, surface tension and viscous forces in the process of stretching deformations of liquid filaments. An overall similarity in the deformation patterns of pairs of liquids with matching (zero-)shear viscosities was observed. The more viscous samples were found to deform in a more uniform manner, especially in the experiments performed at higher velocities of the moving end-plate. The breakup of the viscoelas-

tic samples was generally slower than the breakup of the corresponding Newtonian filaments. It was also found that at the onset of high velocity stretching, inertial effects can lead to a necking deformation of the filament, which is asymmetric with respect to the mid-plane of the filament. The influence of this asymmetry on the applicability of the technique to the measurement of the uniaxial extensional properties of fluids has not been understood to date. However the possibility of the development of this asymmetry, especially in the high imposed strain rate experiments, strongly suggests a preference for an elongational strategy in which both end-plates are moved simultaneously, over elongation of the filament induced by the motion of one of the end-plates. In another set of experiments with the same samples and under same conditions Kröger and Rath (1995) [8] observed that the nonuniform necking deformation of the filaments was accompanied by nonuniform distributions of rate of elongation and considerable shearing. Also in small capillary number stretching experiments it was found that surface tension effects can become so important as to lead to a flow reversal at late stage of deformation, characterized by a well-developed depression in the middle of the filament.

Since the details of the underlying dynamics of the liquid bridge deformations in these filament stretching experiments were and still are experimentally largely intractable, these experiments were complemented by numerical simulations of the devices. Spinnability, the property of being able to be drawn out into long, uniformly deformed thin filaments, of branched polymer melts was investigated

in a numerical simulation by Chang and Lodge (1971) [14]. The first experiment of Sridhar *et al.* (1991) [4] was accompanied by a numerical simulation of the experiment by Shipman *et al.* (1991) [15]. Their group used a free-surface finite element method and the Oldroyd-B constitutive model for the liquid. The study gave an intriguing explanation of the initial high rate thinning of viscoelastic dilute polymer solution filaments, which had led to large discrepancies between the local and imposed stretching rates. It was found that under the combined influence of gravitational and surface tension forces a reverse flow develops near the end-plates, leading to accelerated thinning of the midsection of the filament. Gaudet *et al.* (1996) [16] performed a fairly detailed analysis of the dynamics of Newtonian liquid bridges under uniform stretching, roughly corresponding to the experiments of Kröger *et al.* [7, 8]. They used the boundary element method with the fluid dynamics governed by the linear Stokes equations. The dependence of deformation on initial aspect ratio and capillary number was examined and the viscous force exerted on the stationary end-plate as a function of strain was calculated. As in the experiments of Kröger and Rath (1995) [8], a flow reversal was found in the advanced stages of filament deformation in low capillary number stretching. Sizaire and Legat (1997) [17] studied the extensional response of a Boger fluid in a finite element simulation using the Chilcott-Rallison version of the finitely extensible non-linear elastic dumbbell model (FENE-CR). This model gives the typical deformation pattern exhibited by Boger fluids in stretching experiments. The re-

sults were compared with the experimental measurements of Spiegelberg *et al.* (1996) [11] and qualitative agreement was found, but the underlying dynamics of filament stretching was not investigated.

A detailed investigation of extensional deformations of highly elastic, viscous dilute polymer solution filaments in uniaxial stretching experiments involving the quantitative description of the evolution of the filament profile, the kinematics within the filament and the evolution of the shear and axial normal components of the total extra stress tensor was conducted by Yao and McKinley (1998) [18]. The investigation was based on a finite element numerical simulation of the Oldroyd-B model, and principally compared to the experiments of Spigelberg *et al.* (1996) on two Boger fluids, exhibiting nearly-constant shear viscosities. The response to the stretching deformation of viscoelastic filaments was compared to the response of Newtonian filaments for a wide range of imposed rates of deformation and initial aspect ratios. Good agreement with the experimental measurements was achieved in the results for the experimentally available quantities. At the beginning of deformation the Newtonian and dilute solution filaments deform very similarly, indicating the dominating role of the Newtonian solvent in governing the dynamics of deformation of the viscoelastic filaments at small strains. In agreement with the experimental observations, the filaments deform in highly nonuniform manner with the local rates of extension far exceeding the imposed stretching rate. The finding of Spiegelberg *et al.* (1996) [11] that this behavior can be described satis-

factorily as a "reverse squeeze flow" of a Newtonian fluid (within the lubrication approximation) was reiterated. The model predicts a non-homogeneous deformation of the filament with the maximum elongation occurring in the middle of the filament. This leads to an effective local rate of extension based on the variation of the filament radius in the middle of the filament that exceeds the imposed rate of elongation typically by $\sim$ 50%. At higher strain levels, the deformations of the two types of liquid filaments differ dramatically. The viscoelastic filaments strain-harden in the axial midsection where the strains are largest and deform in a more uniform manner leading to formation of long cylindrical section. In contrast Newtonian filaments do not exhibit strain hardening and continue to deform non-uniformly, developing a concave shape characterized by a narrow neck in the midsection of the filament and quasi-static reservoirs near the end-plates. As a consequence, Newtonian filaments eventually break at a point near the center of the filament. As had been demonstrated in the experiments of Kröger *et al.* (1992) the precise position of the filament failure depends on the interplay of inertial, viscous and surface tension forces. Strain hardening of dilute solution filaments leads to a quite different breakup mechanism. The cylindrical portion of the filament forms during stretching by taking liquid from the quasi-static reservoirs near the end-plates. As a consequence of the fast drainage of the reservoirs, the surface deforms sharply near the end-plates. The variation of the filament shape at large Hencky strains with characteristic very large curvature at the 'foot' area of the

filament was reproduced in the simulation, in qualitative agreement with the experimental observations [11] at early stages of the flow, prior to the onset of a local elastic instability manifested by the breakup of axial symmetry of the filament near the end-plates, accompanied by the development of rich fibrillar structure. Due to numerical difficulties originating from the large curvatures of the filament shape near the end-plates, the simulation could not be continued to include the filament breakup. The simulation predicts a non-homogeneous stress distribution for both Newtonian and viscoelastic filaments. At small strains the stress distributions in the Oldroyd-B and the Newtonian filaments are almost identical. The axial component of the total extra stress tensor, π_{zz}, has a parabolic profile along the centerline of the filament with zero magnitude at the end-plates and a local maximum at the mid-plane, in agreement with the lubrication model. In addition a region of high stress concentration develops at the surface around the mid-plane of the filament. This 'surface boundary layer' of high axial stress concentration persists in the case of the Oldroyd-B fluid throughout deformation. Moreover due to strain hardening of the fluid at the midsection of the filament and subsequent formation of the long cylindrical column connecting two quasi-static reservoirs near the end-plates, additional stress layers are predicted in the latter regions. For Newtonian liquids the simulation predicts the decay of the surface boundary layer at higher strains. The time evolution of the shear stress distribution within stretching filaments was also calculated in the simulation. At small strains, large shear stresses are predicted

for both Newtonian and viscoelastic cases, with the maximum concentration at the thin surface boundary layers at the surface areas of maximum axial curvature. Again a stress decay is predicted for the Newtonian case, and persistence of the high stress surface boundary layers for the Oldroyd-B fluid case.

Although the impetus for intensive development of the experimental technique came from the particular deformation pattern exhibited by low-viscosity, highly elastic dilute polymer solution filaments, it has been recognized that the technique can be equally well applied to measurement of uniaxial extensional properties of other low-viscosity viscoelastic fluids such as concentrated solutions and polymer melts. The non-uniformities in the underlying extensional dynamics of strain-hardening fluid filaments indicated by experimental observations, and elucidated in the numerical investigations of the device, required a careful investigation of the interpretation of experimental data. The central question in this regard was how, in view of the non-homogeneity of extensional dynamics, the measured quantities, in particular the force maintaining the imposed stretch rate, were related to transient extensional properties of test fluids. A fairly broad treatment of this question was given by the joint efforts of Szabo and Kolte *et al.* (1997) [19, 20]. Szabo derived a complete force balance for the liquid filament under extension that includes the effects of inertia and surface tension, and the relative importance of normal stress differences and shear stresses within deforming filament as well as asymmetries due to gravity were discussed. It was found that the measured force on the

end-plate(s) can reliably be related to extensional viscosity of the test fluids provided that filament shape measurements are available. In an accompanying paper, Kolte *et al.* analyzed the performance of the device and the merits of different approaches to the analysis of experimental data. A Boger fluid and a shear-thinning semi-dilute solution were simulated by an Oldroyd-B four-mode model, and the PSM (Papanastasiou, Scriven and Macosko) model, respectively. The model parameters were taken from the fluids used in the experiments by Tirtaatmadja and Sridhar (1993) [10]. With the reservation that the simulation was performed on just two specific fluids, it was found that, with the appropriate approach to analysis of the measurements, the filament stretching device can provide very accurate prediction of the uniaxial extensional properties of a constant shear viscosity, strain-hardening Boger fluid and a shear-thinning weakly strain-hardening fluid. The distribution of the isotropic stress within viscoelastic filaments was given: at very high Hencky strains, $\varepsilon \gtrsim 5$, the surface layers of high stress were found at the areas of high axial curvature in the case of the Boger fluid. In the case of the shear-thinning fluid, a different distribution pattern without surface layers was found, where the stress distribution across the filament was fairly constant. The maximum stresses were localized in the center, in the mid-filament plane. An experimental investigation of the filament stretching device performance in the case of shear-thinning, weakly strain-hardening viscoelastic filaments complemented with the numerical finite-element simulations using single and multi-mode Giesekus con-

stitutive equation was performed by Yao *et al.* (2000) [21]. Excellent agreement between the numerical predictions and experimental results for the extensional stress growth function was found.

Experimental data on the uniaxial extensional properties of the shear-thinning viscoelastic fluids are scarce. The experiments of Kröger *et al.* (1992), Tirtaatmadja and Sridhar (1993) and Yao *et al.* (2000) on a limited number of viscoelastic fluids indicate a range of different responses of these fluids to extensional deformation in the filament stretching device. A common feature of the observed filament deformation patterns is that the deformation of weakly strain hardening viscoelastic fluids is much more similar to that of Newtonian fluids than to the deformation pattern of highly elastic strain hardening dilute polymer solutions, such as Boger fluids. The rate of necking in the middle of a low viscosity shear-thinning fluid filament may be smaller, as in the case of fluids used in Tirtaatmadja and Sridhar experiments and reproduced in the PSM numerical simulation by Kolte *et al.* (1997), or larger than in the Newtonian case, as in the case of the fluid used in Yao *et al.* (2000) experiments.

1.3 Plan of the Thesis

In this work we present a complete small-scale molecular dynamics simulation of the filament stretching device, based on a liquid bridge configuration with microscopic model fluids which exhibit generic rheological properties of both New-

tonian and viscoelastic fluids. In particular, with simple model fluids based on non-crossable linear sequences of spherical atoms connected by finitely extensible nonlinear elastic (FENE) springs, we qualitatively reproduce many aspects of the complex viscoelastic response observed in experiments. These results pertain to the uniaxial stretching of a range of polymeric liquids, including nearly constant shear viscosity dilute polymer solutions (Boger fluids) and complex shear thinning polymer melts. Since molecular-scale calculations of full macroscopic experiments are well beyond our capabilities, we rely on the principle of similitude and compare experiment and simulation at similar values of the relevant non-dimensional groups, such as the capillary and Deborah numbers.

The main goal of the present work is to investigate the power of simple, microscopic fluid models to reproduce the observed experimental behavior, in combination with the inherent capability of molecular dynamics to access some of the experimentally intractable microscopic aspects of the dynamics of the process. For that reason we have focused on cases and parameter ranges where complications due to inertial and gravitational effects are either minimized or entirely avoided. While these additional effects are straightforward to include in simulations, they simply mask the response of fluid test samples to stretching deformations. Furthermore, our simulations correspond to the experiments in which the end-plates separate at an exponentially increasing velocity. Now macroscopic numerical simulations of filament stretching (*e.g.* Kolte *et al.* (1997) [20]) indicate that the most

accurate assessment of the extensional properties of polymeric fluids is obtained when the relative motion of the end-plates is adjusted to have an exponential radial deformation of the mid-filament fluid element, characterized by a constant rate of deformation. However, the stretching protocol we use has the advantage that the response of different fluid formulations to identical external perturbations can be directly compared. A further limitation in our results is that due to the small size of fluid filaments, only modest Hencky strains, $\varepsilon \sim 1.5$, could be obtained, thus limiting both the duration of deformations and the dynamic range of the stretching rates.

The thesis is structured as follows. The molecular fluid models and their properties are discussed in Chapter 2. The molecular dynamics aspects of the filament stretching simulation, and the numerical algorithm are elaborated in Chapter 3. The measurement and evaluation procedures are described in Chapter 4. The exposition of the results in Chapter 5 is followed by concluding remarks in Chapter 6.

2 Model Fluids

In this chapter we will describe the molecular dynamics model liquids used in our simulations. We focus on model fluids of several distinctive types, which exhibit qualitative agreement with the filament stretching experiments involving relatively low viscosity, mobile liquids. These include

- model Newtonian fluid consisting of short linear chains of $N = 4$ atoms,
- model polymer solution, where three linear chains with $N = 40$ are embedded in the $N = 4$ solvent,
- model monodisperse polymer melt comprised of linear chains with $N = 20$
- and a model polydisperse melt.

We have also experimented with a number of alternative microscopic models, but these either presented practical difficulties or did not exhibit any qualitatively new behavior. For example, a monatomic Newtonian fluid has a high vapor pressure and a very diffuse interface, significantly longer chain molecules require excessive

computer time, and various mixtures of molecules behaved similarly to the fluids above.

2.1 Formulation of Model Fluids

It has been found in numerous molecular dynamics simulations that many fundamental rheological properties of polymeric liquids can be successfully reproduced by simple molecular modeling incorporating the most basic physical requirements of connectivity of sequences of monomer units and non-crossability of polymer chains. Examples include an early non-equilibrium molecular dynamics (NEMD) simulation of the behavior of polymer melts in planar Couette flow by Hess (1987) [22], which observed strongly shear thinning viscosities and non-zero normal stress differences with systems of molecular chains formed from a Lennard-Jones atomic liquid with an enhanced force between neighbors on the chains. The same generic properties of polymeric liquids were observed in NEMD simulations of the rheological properties of liquid n-hexadecane by Berker *et al.* (1992) [23], where the chains were modeled in much greater detail through the use of torsional, bond-stretching and bond-bending potentials, as well as in the exhaustive simulations of the rheological and structural properties of monodisperse polymer melts using a finitely extensible nonlinear elastic (FENE) spring chain

model by Kröger *et al.* (1993) [24, 25]. This bonding potential takes the form

$$U_{FENE}(r) = \begin{cases} -\frac{1}{2}k_F r_0^2 \log\left[1 - \left(\frac{r}{r_0}\right)^2\right] & \text{for} \quad r \leq r_0 \\ \infty & \text{for} \quad r > r_0. \end{cases} \tag{2.1}$$

In addition to the chain bonding potential an intermolecular interaction potential is required, and the usual choice is an interaction between all atoms in the system of the 12-6 Lennard-Jones potential form,

$$U_{LJ} = \begin{cases} 4\varepsilon_{LJ}\left[a_r\left(\frac{\sigma_{LJ}}{r}\right)^{12} - a_a\left(\frac{\sigma_{LJ}}{r}\right)^{6}\right] & \text{for} \quad r \leq r_c \\ 0 & \text{for} \quad r > r_c \end{cases} \tag{2.2}$$

In order to have computation times which are linear rather than quadratic in the system size, it is convenient to truncate U_{LJ} at an interparticle distance $r = r_c$, where the value of the cutoff r_c is chosen on case by case basis based upon both physical and practical considerations. The potential provides strong repulsion at short distances due to the $+r^{-12}$ term, effectively equivalent to spherical, non-overlapping particles with a radius near σ_{LJ}. While this particular form of short-range repulsion in the potential is mostly a matter of convenience, the second $-r^{-6}$ term has a physical origin in reasonably approximating the attractive polarization interactions of neutral spherically symmetric atoms. The constants a_r and a_a in the potential allow the simulations of multicomponent systems. An ex-

quantity	unit
mass	m
length	σ_{LJ}
energy	ε_{LJ}
temperature, k_BT	ε_{LJ}
density	σ_{LJ}^{-3}
time	$\tau_{LJ} = [m\sigma_{LJ}^2/\varepsilon_{LJ}]^{\frac{1}{2}}$
velocity	$[\varepsilon_{LJ}/m]^{\frac{1}{2}}$
stress	$\varepsilon_{LJ}/\sigma_{LJ}^3$
viscosity	$[\varepsilon_{LJ}m/\sigma_{LJ}^4]^{\frac{1}{2}}$
normal stress coefficient	m/σ_{LJ}

TABLE 2.1: The system of Lennard-Jones units. The basic quantities are mass, length and energy, and k_B is Boltzmann's constant.

ample is the above-mentioned simulation by Hess [22] where the bonding of the atoms on polymer chains was achieved by the choice $a_r = a_a = 10$. The energy ε_{LJ} and length σ_{LJ} parameters of the potential, along with the mass of the liquid atoms m, serve as a basis for a convenient system of units commonly used in molecular dynamics simulations of liquids, the reduced Lennard-Jones units. We present an outline of the Lennard-Jones units for the quantities used hereafter in this work in Table 2.1.

The basis for all our model liquids is a freely-jointed bead-spring model of linear polymer molecules, such as the one used by Kröger *et al.* [24, 25]. Generally the bead-spring models are useful approximations of real linear polymers designed to avoid treatment of the fast, complex local motions and still capture the essential

large-scale properties responsible for viscoelastic behavior. The physical basis of these models is the independence of large-scale and local motions, which originates in the large differences in their respective characteristic relaxation times. In a bead-spring model, a real linear polymer molecule is arbitrarily divided into $N-1$ equal segments (e.g. Kuhn segments) and represented by a chain of N beads connected by $N-1$ massless springs. The beads can be then thought of as small spheres on which the mass of segments and the interactions with the environment are localized. If a model does not explicitly constrain the relative orientation of the consecutive bonds, the model chain is said to be freely-jointed. A freely-jointed bead-spring model of linear polymer molecules is particularly simple to implement in molecular dynamics simulations, since it only requires the bonding of neighboring beads on a chain by an attractive force.

In modeling liquids used in our simulations we adopted the FENE spring-bead model first because it has a plausible theoretical basis [1] and second because it has been widely and successfully used in simulations of structural and rheological properties of polymeric liquids, and consequently is well documented in literature. In particular we were guided by the model of monodisperse polymer melt systems used in the work of Kremer and Grest [27] and Kröger *et al* [24, 25]. Besides the above mentioned generic properties of polymeric liquids in shear flow, the model exhibits the dynamical crossover from Rouse to reptation diffusive mo-

[1]The FENE potential is a convenient analytical approximation to Langevin function springs of the freely-orienting chain model of linear polymer molecules introduced by Warner (1972) [26].

tion with an entanglement length $N_e \approx 35$ [27]. Also the experimentally observed rheological crossover manifested in a change of power law dependence of the zero shear viscosities on the melt molecular weight was found in NEMD simulations at chain lengths $N_c \approx 100$ [25]. The consistency of the model is reflected in the ratio $N_c/N_e \approx 3$, which is in a good agreement with theoretical prediction given by Bueche in 1952 [28]. The choice of parameters in the FENE and LJ potentials requires discussion. In the papers cited above, the spring constant and the maximum extension of the FENE springs were set to $k_F = 30$ and $r_0 = 1.5$, respectively, in order to ensure non-crossability of molecular bonds. The requirement of the non-crossability of the polymer chains is the minimal condition that has to satisfied in model melts in order to generate the conditions for the confinement and reptating motion of long chains. The excluded volume and intermolecular interactions in the model are given by the purely repulsive Weaks-Chandler-Anderson (WCA) potential, which is derived from the Lennard-Jones potential (eq. (2.2)) with the value of the cutoff set to the position of the potential minimum $r_c = 2^{1/6}$ and parameters $a_r = a_a = 1$ were used. This model is convenient for simulations of the bulk properties of polymer melts, where the fluid can be completely enclosed in a rectangular simulation cell and periodicity in all three directions assumed. In this case the small value of the cutoff reduces the number of pairwise interactions between the beads, and speeds up the computation considerably.

In the situation considered here, the liquid has a free surface and an attrac-

tive interaction between different molecules is required to have a cohesive liquid. Although the WCA potential could still be used as the excluded volume interaction within molecules, it is computationally simpler to have a universal form for all of the non-bonding interactions, so we adopt the Lennard-Jones potential (eq. (2.2)) truncated at the standard cutoff distance $r_c = 2.5$. The only difference is an inessential modification of the properties of individual molecules, and since we do not attempt to model specific chemical properties anyway, this is a minor detail. We do however modify the interaction by adding an additional linear term [3],

$$U^{shift}(r, r_c) = \begin{cases} -U_{LJ}(r_c) - (r - r_c)\left[\dfrac{dU_{LJ}}{dr}\right]_{r_c} & \text{for} \quad r \leq r_c \\ 0 & \text{for} \quad r > r_c \end{cases} \tag{2.3}$$

so that the force vanishes smoothly at the cutoff. The parameters of the FENE potential used in our Newtonian and polymer melt model liquids are the same as those used by Kremer and Grest and Kröger *et al.*, $k_F = 30\varepsilon_{LJ}/\sigma_{LJ}^2$ and $r_0 = 1.5\sigma_{LJ}$. The remaining parameters in the Lennard-Jones potential are $a_r = 0.8$ and $a_a = 1$. The potentials are shown in Figs. 2.1 and 2.2. In Fig. 2.1 the shifted Lennard-Jones potential with $a_r = 0.8$ is compared to the usual shifted Lennard-Jones potential with $a_r = 1$. Fig. 2.2 shows the full bonding interaction potential. The coefficient $a_r \neq 1$ had been retained in the Lennard-Jones potential in order

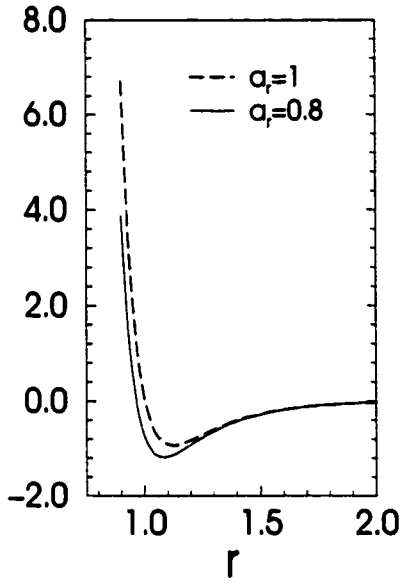

FIGURE 2.1: Shifted Lennard-Jones potentials with $a_r = 1$ and $a_r = 0.8$

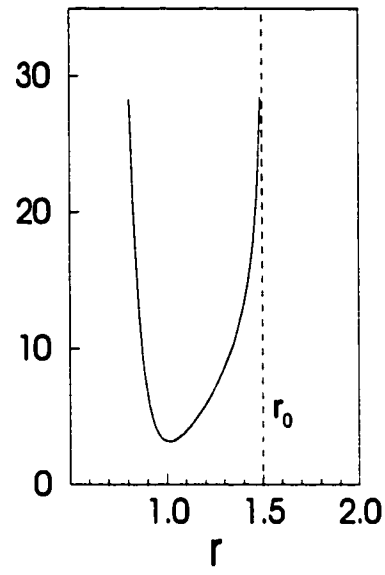

FIGURE 2.2: The bond $U_{LJ}(a_r = 0.8) + U_{FENE}$ potential

to manipulate the density of our model liquids. This would be unnecessary in a simulation of the bulk properties where with a given number of atoms any desired density is obtained by appropriate choice of the size of the simulation cell. All our systems were prepared and the filament stretching simulations started at a reduced temperature $T \approx 0.85$. At this temperature, our choice of the strength of the repulsion leads to liquid systems with density $\rho \approx \sigma_{LJ}^{-3}$ as compared to typical densities of standard Lennard-Jones monatomic liquids $\rho \approx 0.84\sigma_{LJ}^{-3}$. An interesting consequence of the high density of the $N = 20$ melt system observed in equilibrium, where we have an approximately cylindrical filament configuration, is that the chain bonds were compressed, even though the hydrostatic pressure

inside the filament was small, $P \approx 0.05\sigma_{LJ}^3/\varepsilon_{LJ}$. This effect had already been observed in the aforementioned MD simulations of dense polymer melts by Gao and Weiner [29, 30] and entirely related to complex steric interactions which are present at high molecular densities. The interactions are found to be insensitive to hydrostatic pressure and the effect present even when $P = 0$. Our result, obtained with a different model fluid in a different configuration supports this idea.

The models for the Newtonian liquid and for the polydisperse polymer melt were obtained by appropriately connecting and cutting the chains of length $N = 20$ in the monodisperse melt. To be more precise, a polydisperse melt is obtained from an equilibrated state of the monodisperse melt in two steps. First a giant ring chain is formed by connecting the ends of the linear chains. Even at the high densities this is achieved easily by use of an linear elastic potential. In the second step the giant chain is cut so as to generate the desired polydispersity. Of course, the newly created system has to be re-equilibrated. The short chain, $N = 4$, fluid is obtained by simply cutting the $N = 20$ chains of the initial system. Strictly speaking it could be argued that this system is a model for a low molecular weight linear polymer melt. However the chains are short enough as not to give non-Newtonian behavior at reasonably low deformation rates, as was found in our simulations of the shear properties of the model fluids which will be discussed shortly. The particular structure of the molecules in this model is just a consequence of convenience of the manner in which the fluid had been generated. In that light we prefer not

to think of this structure as a FENE linear polymer but rather as a simple device to obtain a non-volatile, viscous fluid. The same device had already been used by Yang, Koplik and Banavar (1992)[31] in a model Newtonian fluid comprised of dimers bound by an $\sim r^{+6}$ potential. For this purpose the exact form of the bonding potential is entirely irrelevant.

For the bonding potential in the case of polymer chains used in our dilute solution model we made somewhat unusual choice which is a FENE potential analog to an elastic Fraenkel potential

$$U_{FF}(r) = \begin{cases} -\frac{1}{2}k_{FF}r_0^2 \log\left[1 - \left(\frac{r-a}{r_0}\right)^2\right] & \text{for} \quad |\, r-a \,| \leq r_0 \\ \infty & \text{for} \quad |\, r-a \,| > r_0 \end{cases} \tag{2.4}$$

where $a = 2\sigma_{LJ}$ is the zero-force distance, $r_0 = 0.5\sigma_{LJ}$ is the finite extensibility (compressibility) of the bond and $k_{FF} = 60$. This potential is shown in Fig. 2.3. The motivation for this choice comes from the simulations of Dünweg and Kremer [32] of dilute polymer solutions in a monatomic solvent where the parameters of the FENE potential were relaxed to $k_F = 7\epsilon_{LJ}/\sigma_{LJ}^2$ and $r_0 = 2\sigma_{LJ}$. In these simulations only one polymer chain was used and non-crossability was not an issue. The practical difference between this choice of parameters as compared to the standard one was that the bonds were slightly longer and the chain more flexible. As Fig. 2.2 shows, the bonding potential in this case is asymmetric and at short

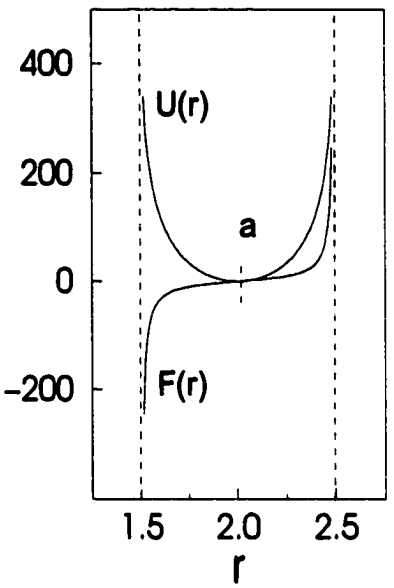

FIGURE 2.3: FENE potential used with the polymer chains in the dilute solution model liquid.

distances dominated by the Lennard-Jones part of the potential. Furthermore, the average distance between neighbors on the chain does not differ significantly from the average distance between the closest neighbors in the monatomic Lennard-Jones liquid solvent. With the potential U_{FF}, the relative distribution of the beads on the chains is fully dominated by the FENE potential and the particular choice of the zero-force distance renders the Lennard-Jones part of the interaction between the nearest neighbors on the chain irrelevant. The behavior of the solution of these chains in the $N = 4$ solvent in the filament stretching simulation is very different from that of the analogous solution with standard FENE chains having the same number of beads. It is not clear whether the differences come from the difference in the bond lengths, or the greater flexibility of the chains.

2.2 Characterization of Model Fluids

The essential characterization of the model fluids, with a view toward description of their response to deformation in the filament stretching experiment, involves calculation of surface tensions and the basic material functions which characterize liquid response to simple shear deformation, i.e., shear viscosities and normal stress coefficients. Calculations of these properties require somewhat different, although well established, molecular dynamics techniques. The surface tension calculation is a typical equilibrium problem which involves a careful definition of a molecular dynamics configuration that allows for unambiguous interpretation of the simulation results. The calculation of the material functions that characterize fluid response to shear deformation on the other hand requires application of a non-equilibrium molecular dynamics (NEMD) technique designed specifically for efficient calculation of these properties [33, 34, 35]. In the following we will give the definitions of relevant quantities accompanied with short descriptions of corresponding molecular dynamics calculations.

2.2.1 Surface Tension

Surface tension α characterizes the interface between two systems in contact in thermodynamic equilibrium. If work δW is done in a reversible change of the

interfacial area δA, the surface tension is then

$$\alpha = \frac{\delta W}{\delta A}. \tag{2.5}$$

A liquid-vapor system with a planar interface is particularly convenient for a molecular dynamics measurement of the surface tension, because in this geometry the surface tension can be expressed in terms of readily measurable quantities. In equilibrium the pressures on either side of the interface are equal and their gradients are zero. The interface however introduces a preferred direction, and the condition for equilibrium takes more general form

$$\nabla_\alpha P_{\alpha\beta} = 0 \qquad \text{where} \qquad \alpha, \beta = x, y, z \tag{2.6}$$

If the interface lies in the xy-plane, none of the pressure components depend on x and y and eq. (2.6) implies

$$P_{xx}(z) = P_{yy}(z) = P_T(z), \qquad \text{and} \qquad P_{zz}(z) = P_N$$

where $P_T(z)$ and P_N are the tangential and normal components of the pressure tensor (with respect to the interface), respectively. The normal component P_N is constant and equal to the bulk pressure. The tangential component differs from P_N only at the surface. Consider a reversible deformation in which a slab of liquid

of thickness dz and surface A is squeezed. Since the volume of the slab remains unchanged

$$\delta V = dz\delta A + A\delta(dz) = 0$$

the work done in deformation is given by

$$\begin{aligned}\delta W &= -P_T dz\delta A - P_N A\delta(dz) \\ &= \delta A(P_N - P_T)dz\end{aligned}$$

Hence we obtain the following expression for the surface tension of a planar interface

$$\alpha = \int_{z_1}^{z_2} dz[P_N(z) - P_T(z)]. \tag{2.7}$$

The limits of integration z_1 and z_2 lie on opposite sides of the interface, and can be extended to infinity since $P_N = P_T$ outside of the interfacial region. The utility of this definition of the surface tension depends on the availability of a local expression for the pressure tensor. The pressure tensor is the same as the momentum flux tensor, and contains a kinetic contribution due to the thermal motion of molecules and a configurational contribution due to intermolecular forces. In a homogeneous

fluid the pressure is a scalar quantity given by

$$P = \rho k_B T + \frac{1}{6} \int d^3 r r F(r) \rho^{(2)}(r) \tag{2.8}$$

where $\rho^{(2)}$ is the two-body distribution function which depends only on the particle separation r. This expression can not be uniquely generalized to the non-homogeneous fluid since there are many consistent ways of deciding which forces contribute to the pressure. In this work we employ the commonly-used expression for the microscopic pressure tensor due to Irving and Kirkwood [36]. In discretized local form, applicable to equilibrium and non-equilibrium atomistic calculations, it is given by,

$$V_B P_{\alpha\beta}(\vec{r}_B) = \sum_{i \epsilon B} \left[m_i (\dot{r}_{i\alpha} - u_\alpha(\vec{r}_B))(\dot{r}_{i\beta} - u_\beta(\vec{r}_B)) + \frac{1}{2} \sum_{j>i} r_{ij\alpha} F_{ij\beta}) \right]. \tag{2.9}$$

V_B is the volume of the sampling bin B whose position is centered at $\vec{r}_B$ and $\vec{u}(\vec{r}_B)$ is the Eulerian velocity of the fluid in bin B, defined as the average velocity of the N_B particles contained in the bin,

$$\vec{u}(\vec{r}_B) = \frac{1}{N_B} \sum_{i=1}^{N_B} \dot{\vec{r}}_i. \tag{2.10}$$

Here, $\vec{r}_i$ is the position of particle i and $\vec{r}_{ij}$ and $\vec{F}_{ij}$ are the separation and force between particles i and j respectively; particle j may or may not be in the same bin.

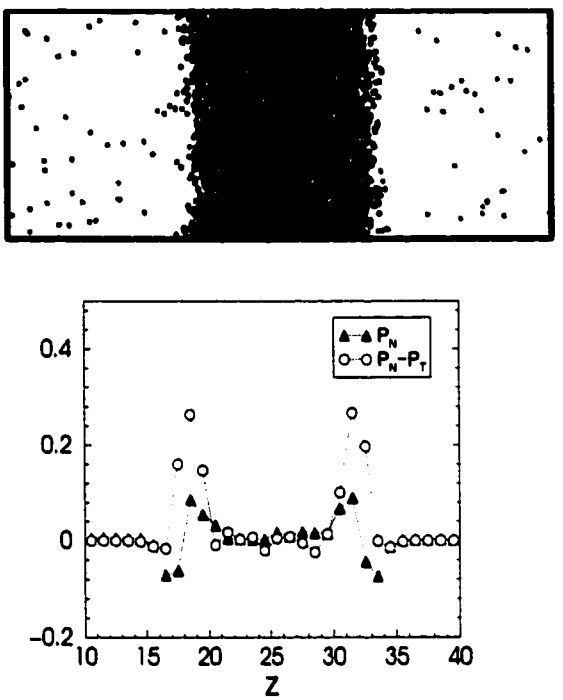

FIGURE 2.4: An instantaneous configuration of an atomic liquid-vapor system in molecular dynamics surface tension simulation and the distribution of the normal component, P_N, and the difference of the normal and tangential components, $P_N - P_T$, of the pressure tensor across the liquid element.

The particle velocity with respect to the Eulerian velocity $\vec{u}(\vec{r}_B)$ which appears in the pressure tensor is sometimes referred to as the particle peculiar velocity.

A snapshot of a molecular dynamics simulation with a planar interface, which has the symmetry needed to take advantage of the simplicity of eq. (2.7) is shown in Figure 2.4. In order to avoid the difficulties associated with the use of constraining surfaces, a double-sided liquid slab is placed so as to span the simulation box, and periodic conditions in all three directions are implemented. With such periodic conditions, a particle which leaves the simulation box is replaced by its image

which enters the box through the opposite face, and interparticle forces are computed from the nearest image particle. Typically approximately 2000 particles were used in these simulations.

The pressures $P_N(z)$ and $P_T(z)$ are measured as the space and time averages of the Irving-Kirkwood tensor in the thin slices parallel to the average interface, and the surface tension can be calculated from the discretized version of eq. (2.7)

$$\alpha = \frac{1}{2}\sum_B (P_N - P_T)\Delta z \tag{2.11}$$

The factor $\frac{1}{2}$ accounts for the two interfaces involved in the simulation. The variation of the normal component of the pressure tensor and the difference $P_N - P_T$ across the liquid slab is shown in Fig. 2.4. In equilibrium the normal pressure P_N should be constant throughout the system. Our simulation however reveals the variation of P_N across the surface. The form of this variation does not contradict the constancy of P_T macroscopically since across the surface it averages out to the mean value of P_N in the liquid bulk. Similar variation is observed in the variation of radial component of the pressure tensor, P_{rr}, across the cylindrical surface. This variation may originate from the microscopic irregularities in the free surfaces which result in an effective contribution of the tangential components of interparticle interactions to the measured normal components of the pressure tensor. The measurement of the pressure tensor distribution entailed in the determination

of the surface tension through eq. (2.11) allows a detailed characterization of the surface properties. However if one is interested only in the measurement of the surface tension, eq. (2.11) can be cast into a more convenient form. With

$$P_{\alpha\alpha} = \rho(z)kT + \frac{1}{2}\sum_{i,j>i} r_\alpha F_{ij,\alpha}, \qquad P_T(z) = \frac{1}{2}(P_{xx} + P_{yy})$$

and

$$F_\alpha = -\frac{\partial V(r)}{\partial r_\alpha} = -\frac{dV(r)}{dr}\frac{r_\alpha}{r}$$

one gets [2]

$$\begin{aligned} 2\alpha &= -\frac{1}{4A}\sum_B \sum_{\substack{i\epsilon B \\ j\neq i}} [3z_{ij}^2 - r^2]\frac{1}{r}\frac{dV}{dr} \\ &= \frac{1}{2A}\sum_{i,j>i} [r^2 - 3z_{ij}^2]\frac{1}{r}\frac{dV}{dr} \end{aligned} \tag{2.12}$$

The results for surface tensions of the model liquids are presented along with the shear properties of the model fluids in Table 2.2 at the end of the next section.

2.2.2 Shear Viscosity and Normal Stress Coefficients

Shear viscosity and normal stress differences are most easily calculated from a molecular dynamics simulation of a steady, planar Couette flow. In order to avoid the surface effects or non-uniformities introduced by the presence of the bound-

[2] This expression differs by factor 2 from the expression given in Rowlinson and Widom [37].

ing solid surfaces, used to generate the flow in real experiments, the simulation is performed in a rectangular simulation cell with periodicity assumed in all three directions. The flow is generated and maintained by a simple adaptation of the ordinary orthogonal periodic boundary conditions in equilibrium molecular dynamics simulations. Consider a steady, planar Couette flow in the x-direction with the velocity gradient in the z-direction,

$$u_x = \dot{\gamma} z, \qquad u_y = 0, \qquad u_z = 0 \tag{2.13}$$

where $|\dot{\gamma}|$ is the shear rate. The material functions appropriate for this flow are [1] the shear viscosity

$$\eta(\dot{\gamma}) = -\frac{P_{xz}}{\dot{\gamma}} \tag{2.14}$$

and the normal stress coefficients Ψ_1 and Ψ_2,

$$\begin{aligned} \Psi_1(\dot{\gamma}) &= -\frac{P_{xx} - P_{zz}}{\dot{\gamma}^2} \\ \Psi_2(\dot{\gamma}) &= -\frac{P_{zz} - P_{yy}}{\dot{\gamma}^2}. \end{aligned} \tag{2.15}$$

The appropriate flow is generated by the imposition of boundary conditions corresponding to perfect shear relative motion between particles and their images in the z-direction. In a simulation cell of height Z, the relation between the positions

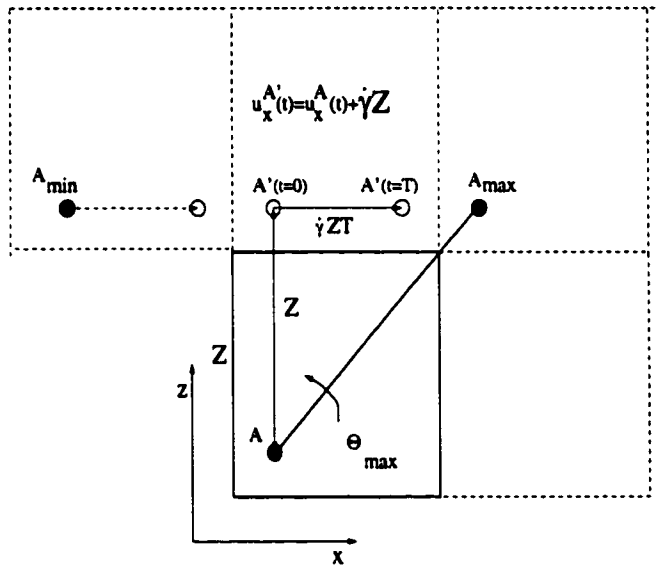

FIGURE 2.5: Lees-Edwards periodic boundary conditions for planar Couette flow.

of the particle and its first image in the +z-direction is given by

$$
\begin{aligned}
&x' = x + \dot{\gamma}Zt; \qquad && y' = y; \qquad && z' = z + Z; \\
&u'_x = u_x + \dot{\gamma}Z; \qquad && u'_y = u_y; \qquad && u'_z = u_z,
\end{aligned}
\tag{2.16}
$$

where t is the elapsed time from the beginning of the simulation. The periodic conditions (2.16), illustrated in Fig. 2.5, are known as Lees-Edwards boundary conditions [33]. Although conceptually simple, some care must be exercised in their actual implementation into an efficient molecular dynamics code. Fig. 2.5 shows the relation of a particle A and its image A', whose position changes in course of time. If A' is the position of a particle that crosses the boundary at $z = Z$ it is to be replaced into the simulation cell at the position A. In a long simulation the relative distance between a particle and its image increases linearly with time, which

implicitly leads to very distorted simulation cell. It is convenient to replace the particle image followed in the simulation at appropriate time intervals. In our implementation an image of particle A is followed until it reaches the position A_{max} when the focus is transferred to its image at A_{min} Of course with appropriate replacement of particles which leave the simulation cell according to eq. (2.16) the simulation cell does not deform. In shear flow, work is continuously done on the system and Any heat generated has to be removed since otherwise a steady state could not be realized. Furthermore, since the fluid temperature would rise, any measurement of a transport coefficient would give its temperature average. There are quite a few methods available to maintain constant temperature in molecular dynamics with various degrees of theoretical foundation. It is somewhat surprising that the results for viscosities generally do not depend, within statistical uncertainties, on the particular method (Evans *et al.* (1985) [38]). In our implementation of the shear flow simulations we keep the dynamic temperature constant and uniform by locally applying, the so-called Nosé-Hoover thermostat. In this approach the equations of motion for individual particles are extended to include a friction coefficient ξ

$$\frac{d^2 r_\alpha}{dt^2} = F_\alpha - \xi v_\alpha^p \tag{2.17}$$

where v_α^p are components of the peculiar velocity of a particle. The friction coefficient satisfies the following equation of motion,

$$\frac{d\xi}{dt} = \frac{T(t) - T_c}{Q^2} \tag{2.18}$$

where $T(t)$ is the running and T_c desired temperature. Q is an arbitrary thermostat relaxation time which defines the strength of the thermostat. The local streaming velocities, which are necessary for the accurate calculation of the peculiar velocities of the particles and, by extension, the running local temperatures are the long time averages of the peculiar velocities of the particles contained in thin rectangular bins parallel to the xy-plane. This particular algorithm has the conceptual advantage that one can show that it leads to a statistical ensemble in local thermodynamic equilibrium.

In course of simulations the components of the pressure tensor were measured as time averages over time intervals $\Delta t = 100\tau_{LJ}$,

$$< P_{\alpha\beta} >_n = \frac{1}{n} \sum_{i=1}^{n} P_{\alpha\beta}, \tag{2.19}$$

where n is the number of integration time steps in Δt. If the data points were uncorrelated the variance in the run average

$$< P_{\alpha\beta} >_N = \frac{1}{N} \sum_{i=1}^{N} < P_{\alpha\beta} >_n, \tag{2.20}$$

would simply be given by [3]

$$\sigma^2(< P_{\alpha\beta} >_N) = \frac{1}{N}\sigma^2(P_{\alpha\beta}) \tag{2.21}$$

where

$$\sigma^2(P_{\alpha\beta}) = \frac{1}{N}\sum_{i=1}^{N}(< P_{\alpha\beta} >_n - < P_{\alpha\beta} >_N)^2. \tag{2.22}$$

In case of correlated data, which could be expected for the model melts characterized with long relaxation times, a more general expression for the variance in the run average

$$\sigma^2(< P_{\alpha\beta} >_N) = \frac{s}{N}\sigma^2(P_{\alpha\beta}) \tag{2.23}$$

must be used. Here s is the statistical inefficiency given by [3]

$$s = \lim_{n_b \to \infty} \frac{n_b \sigma^2(< P_{\alpha\beta} >_b)}{\sigma^2(P_{\alpha\beta})} \tag{2.24}$$

where

$$\sigma^2(< P_{\alpha\beta} >_b) = \frac{1}{N_b}\sum_{i=1}^{N_b}(< P_{\alpha\beta} >_b - < P_{\alpha\beta} >_N)^2. \tag{2.25}$$

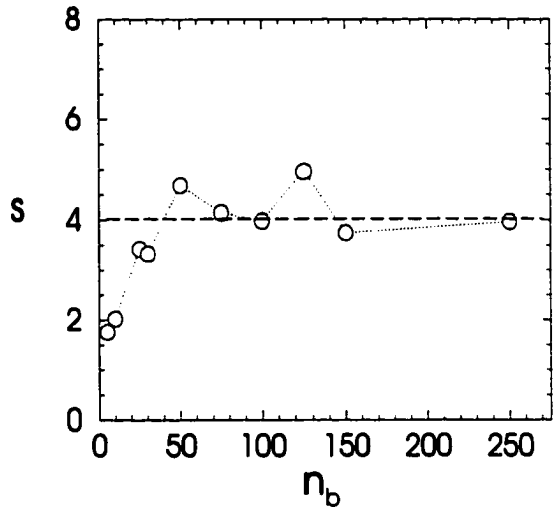

FIGURE 2.6: The calculation of the statistical inefficiency

is the variance of the run average associated with the blocks of n_b data points,

$$(2.26) \qquad < P_{\alpha\beta} >_b = \frac{1}{n_b} \sum_{i=1}^{n_b} < P_{\alpha\beta} >_n, \qquad \text{and} \qquad N = N_b n_b.$$

A typical example of the calculation of the statistical inefficiency is shown in Fig. 2.6, for the measurement of the viscosity of the monodisperse polymer melt at the shear rate $\dot{\gamma} = 10^{-4}$.

The results of the shear flow simulations for the dependence of viscosities and normal stress coefficients on shear rate are shown in Fig. 2.7. The error bars smaller than the size of the symbols are not shown. Results are shown for the N=20 and N=4 model liquids and for a 20% solution of chains of length N=20 in an N=4 solvent. This solution was dropped from our simulations of the filament stretching and will not be further discussed in this work. However it is the only polymer

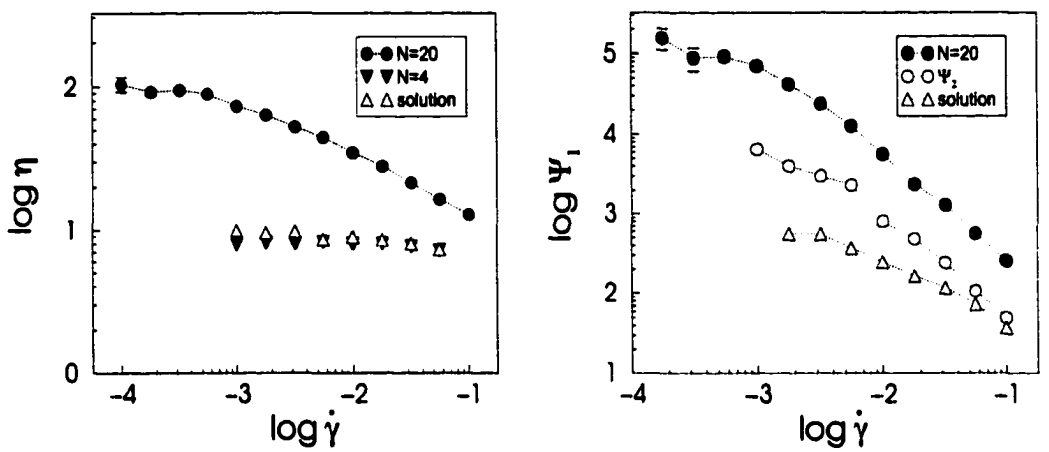

FIGURE 2.7: Steady shear flow material functions for the model fluids

solution for which we have performed shear flow simulations, and we show its properties to illustrate the differences in the shear properties of the pure solvent and a (semi)-dilute solution. Similarly we do not have data for the polydisperse melt, whose extensional behavior is discussed below. The reason is that a meaningful calculation of the viscosities and normal stress differences requires very long simulation runs, which by far exceed the time needed for the basic purposes of our work. In the following discussions the shear properties of the polydisperse melt and the solution model liquids will be assumed to be similar to the properties of the N=20 monodisperse melt and the 20% solution discussed here, respectively

In the figures, we see that the viscosity of the $N = 4$ model liquid is approximately constant up to a fairly large shear rate, $\dot{\gamma} = 0.1$, and can be considered as an acceptable model of a Newtonian liquid, in view of the fact that at shear rates of order $\mathcal{O}(10^{-1})$ even the viscosities of monatomic Lennard-Jones liquids

exhibit shear thinning behavior [35]. The viscosity of the solution, in comparison, is somewhat larger and shows very weak shear thinning. The significant difference between the two is revealed in the first normal stress coefficient: while the solution exhibits a non-zero, positive first normal stress coefficient with the typical, experimentally observed, power-law variation, the first normal stress coefficient for the $N = 4$ model liquid simply shows large fluctuations around zero (not displayed here). Both the viscosity and the first normal stress coefficient for the $N = 20$ monodisperse model liquid decrease significantly with shear rate and exhibit a power-law variation. In addition, in this case we were able to measure the experimentally less tractable and generally less understood second normal stress coefficient Ψ_2. In accordance with fairly scant experimental evidence [1], we found a negative Ψ_2 with the ratio $-\frac{\Psi_2}{\Psi_1} \approx 0.2$ within the range of the experimental values. Moreover $-\Psi_2$ exhibits a similar variation with shear rate as Ψ_1. This result is supported neither by experiments nor by theoretical Predictions, but is in qualitative agreement with the NEMD simulation results for the melt systems of long polymer chains of Berker *et al.* [23] and Kröger *et al.* [24]. The value $-\frac{\Psi_2}{\Psi_1} \approx 0.2$ is also in a fair agreement with the prediction of Doi and Edwards [39], $-\frac{\Psi_2}{\Psi_1} = 2/7$.

In the power-law region, the viscosity of a fluid may be expressed as

$$\eta = A\dot{\gamma}^{n-1} \tag{2.27}$$

where A is a measure of the consistency of the fluid and n is a measure of the degree of non-Newtonian behavior [40]. An analogous expression describes the power-law region in the variation of the first normal stress coefficient with shear rate. The slopes for viscosity and the first normal stress coefficient for the $N = 20$ model melt are -0.39 and -1.3, respectively. Again these values fall well within range of typical values for polymeric liquids and are very similar to the n-hexadecane NEMD simulation results, -0.45 and -1.4, of Berker *et al.* [23].

Besides qualitatively ascertaining the nature of the model liquids, the purpose of the shear flow simulations was to determine characteristic time constants of the fluids, which could be used to construct Deborah numbers which characterize the filament stretching simulations. In experimental work, the time constants of investigated fluids are usually determined based either on a single relaxation time assumption in which the time constant is derived from the shear rate at which the crossover from linear to nonlinear behavior occurs,

$$\lambda = \frac{1}{\dot{\gamma}} \tag{2.28}$$

or on an relaxation time found in linear viscoelasticity

$$\lambda = \lim_{\dot{\gamma}\to 0} \frac{\Psi_1}{2\eta} = \frac{\Psi_{1,0}}{2\eta_0} \tag{2.29}$$

None of the two give well defined time constants for our model liquids since we

FLUID	shear viscosity η_0	surface tension α	relaxation time λ
N=20	97.0 ± 2	1.2758 ± 0.0001	~ 450
solution	9.7 ± 0.2	0.6458 ± 0.0005	~ 30
N=4	8.0 ± 0.1	0.6223 ± 0.0005	0

TABLE 2.2: Material properties of the model fluids

were not able to perform long enough runs at small enough shear rates to determine the zero-shear-rate values for viscosities and the first normal stress coefficients nor, in case of the $N = 20$ model melt, a careful examination of the variation of viscosity in the transition region from linear to power-law behavior. The approximate results presented in Table 2.2 were determined based on simple averages of the values for the lowest shear rates where viscosities and first normal stress coefficients exhibit approximate independence of shear rate.

3 Molecular Dynamics Simulation

In this chapter we discuss the preparation of initial molecular dynamics liquid bridge configurations and describe the simulation procedures. As in real experimental situations the problem of effective adhesion of the ends of fluid filaments to the end-plates arises. We discuss some possibilities for the structure of fluid-solid interfaces and their influence on the deformation of fluid filaments.

3.1 Preparation of Initial Liquid Bridge Configurations

The molecular dynamics liquid bridge configurations were initiated with a set of $n_{tot} = 6790$ atoms distributed over a simple cubic lattice enclosed in a cylindrical region. $n_s = 1290$ atoms were used to simulate the end-plates, and the remaining $n_l = 5500$ atoms were used in modeling the fluids whose general description was given in Chapter 2. The basic fluid formulation was the monodisperse polymer melt system comprised of linear chains with $N = 20$ atoms. The atoms were assigned random initial velocities from a Maxwellian velocity distri-

bution corresponding to a temperature, $k_BT \approx 1\ \epsilon_{LJ}$, which is well above glass transition temperature [41]. Since no attempt had been made to randomize the polymer chain atom sequences in labeling the atoms in the initial regular distribution, the resulting molten state was not appropriate for the filament stretching simulations due to pronounced alignment of the polymer chains.

To randomize the distribution of the polymer bond orientations and obtain an entangled system of polymer chains the system was diluted to a uniform density $\rho \approx 0.15$ by an instantaneous increase of the separation between the end-plates and use of a purely repulsive Lennard-Jones force between all atoms in the system. In this phase of preparation the system was enclosed in a cylindrical container coaxial with the desired orientation of the liquid bridge configuration. The walls of the container were simulated by the same repulsive potential used in interatomic interactions. After the system had reached dilution, the end-plates were slowly brought to the desired length of the initial liquid bridge configuration. The system was then equilibrated at the temperature $k_BT = 0.85\ \epsilon_{LJ}$ over the time interval exceeding the time constant found in the NEMD simulation of shear properties of the fluid.

The initial liquid bridge configuration for the model Newtonian fluid comprised of the short linear chains with $N = 4$ atoms was obtained from the monodisperse melt configuration by appropriate cutting of the chains with $N = 20$. The (semi-) dilute polymer solution system which contained three linear chains

of length $N = 40$ was obtained by connecting the ends of the initial chains separated enough as to give noninteracting long polymer chains in the Newtonian solvent. Strictly speaking, since all fluid atoms in our simulations were given the same mass, our solution models a 2.2 wt.% polymer solution. However with the size of the model liquid sample and the particular configuration used in our simulations the precise relation of this, and other model fluids, to real polymeric liquids is unclear. Finally in order to have flexibility in the exact formulation of the model polydisperse polymer melt, the ends of the polymer chains of the basic melt system were connected to give a giant ring molecule by the use of a linear elastic potential. Despite a large density of the monodisperse melt system this is easily accomplished in a couple of thousand time steps. The ring molecule was cut to give a linear polymer melt system consisting of

30 linear chains of length $N = 60$, 70 chains of length $N = 40$, 30 chains of length $N = 20$ and 20 chains of length $N = 13$. The system was then re-equilibrated for time $t = 7.5 \times 10^3$ Lennard-Jones time units.

3.2 Geometric Description and Deformation Strategy

A schematic view of the molecular dynamics representation of the basic experimental liquid bridge configuration, including a liquid filament and the bounding end-plates, is shown in Fig. 3.1. The end-plates were initially given the atomic structure of a solid by tethering the atoms to the lattice sites of the two planes at

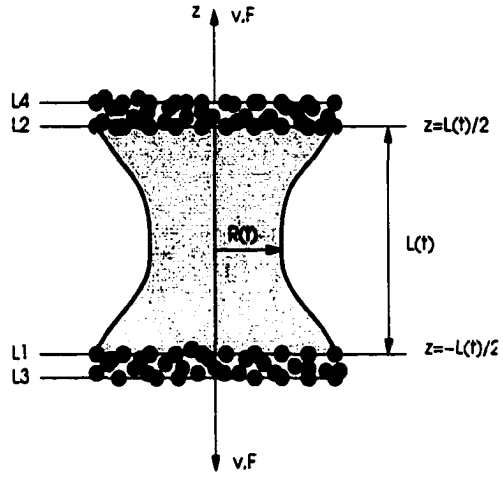

FIGURE 3.1: Schematic of the molecular dynamics liquid bridge configuration

the surface of an fcc solid by an elastic potential. The irregularly distributed circles represent the instantaneous locations of the end-plate atoms, while the lines L1 through L4 label the planes of the corresponding, regularly distributed lattice sites. The shaded area represents an axisymmetric fluid filament. Due to irregularities in the microscopic configuration we use an operational definition of the length of the fluid filament as the distance between the inner planes of the end-plates force centers

$$L(t) = z(L2) - z(L1). \tag{3.1}$$

Similarly the definition of the initial filament radius, R_0, is based on the uniform distribution of the end-plates atom force centers and the assumption that fluids completely cover the end-plates. The radius of initial, approximately cylindrical, configurations is taken to be the radial distance of the outermost force center from

the end plate center of mass. In all cases we used the initial configurations of same size with $R_0 = 10.98\sigma_{LJ}$ and $L_0 = 14.35\sigma_{LJ}$. Implicit in our definitions of L_0 and R_0 is the view of the liquid-wall interface and the free surface of the liquid filament as the minimal surfaces on which the fluid density is approximately zero.

As is the usual practice in real experiments, we use a constant imposed stretching rate,

$$\dot{\varepsilon}_0 = \frac{v_0}{L_0}, \tag{3.2}$$

as a basic characteristic of a particular simulation. In addition, since all test samples had the same initial length, $L_0 = 14.38\sigma_{LJ}$, we will often refer to a particular simulation by the initial velocity, v_0. The length deformation of the fluid filament will be characterized by the Hencky strain

$$\varepsilon = \dot{\varepsilon}_0 t = \ln \frac{L(t)}{L_0}. \tag{3.3}$$

and an aspect ratio,

$$\Lambda(t) = \frac{L(t)}{2R_0}. \tag{3.4}$$

With this definition the initial aspect ratio of all configurations is $\Lambda_0 = 0.654$. The nonuniform contraction of the filament will be characterized by a nondimensional

minimum radius of the filament,

$$R(t) = \frac{R_{min}(t)}{R_0}. \tag{3.5}$$

The fluid filaments were deformed by simultaneous motion of the end-plates in the opposite directions with velocities

$$v(t) = \begin{cases} 0 & \text{if} \quad t < 0, \\ \frac{1}{2}\dot{\varepsilon}_0 L(t) & \text{if} \quad t \geq 0. \end{cases} \tag{3.6}$$

The relative velocity of the end-plates corresponds then to the exponential variation of the length of the filament

$$L(t) = L_0 e^{\dot{\varepsilon}_0 t} \tag{3.7}$$

which is same to the length variation experienced by a material cylinder in the simple uniaxial elongational flow (eq. (1.2)). This deformation strategy was chosen to avoid asymmetries in the transient filament shapes with respect to the mid-plane of the filament caused by fluid inertia. In the experiments of Kröger *et al.* (1992) [7] in which the deformation of test samples was generated by the uniform motion of only one of the end-plates, large inertial asymmetries were observed in the deformations of both Newtonian and viscoelastic filaments in the initial phase of experi-

ments with higher end-plate velocity. This type of non-uniform deformation of the filament was found to be significant throughout deformation in our exploratory molecular dynamics simulations of all model fluids, at all but relatively small imposed rates of stretching. While the problem itself might be important in relation to the reliable interpretation of the transient extensional viscosity measurements, as discussed by Szabo (1997) [19], it is outside the scope of this work. The effect is generally considered to be negligibly small in the experiments with highly elastic dilute polymer solutions, which were almost exclusively studied during last decade, and in most experiments one of the end-plates was held fixed. The exception were the experiments by Tirtaatmadja and Sridhar (1993) [10] in which they systematically used a filament stretching apparatus with simultaneously moving end-plates.

3.3 Dimensionless Groups

The relative importance of the forces that affect the dynamics of the deformation of the fluid filament is described by several nondimensional combinations of parameters which characterize the test sample and the stretching deformation. The Reynolds number,

$$Re = R_0^2 \frac{\rho}{\eta_0} \dot{\varepsilon}_0, \tag{3.8}$$

characterizes the relative importance of inertial and viscous effects. The importance of surface tension relative to viscous forces is given by the capillary number,

$$Ca = R_0 \frac{\eta_0}{\alpha} \dot{\varepsilon}_0. \tag{3.9}$$

The dimensionless group appropriate for viscoelastic fluid samples, which may be interpreted as the ratio of elastic and viscous forces [1], is the Deborah number

$$De = \lambda \dot{\varepsilon}_0, \tag{3.10}$$

where λ is the characteristic relaxation time of the fluid.

Finally the gravitational body forces on the fluid filament are characterized by the Bond number

$$Bo = R_0^2 \frac{\rho}{\alpha} g. \tag{3.11}$$

The characteristics of typical simulations referred to in this work are compiled in Table 3.1. All simulations were performed in absence of gravity so the Bond number is identically zero. The characteristic capillary and Deborah numbers fall within the range of published values for experiments involving viscoelastic fluids [18, 21]. Relatively high values of Reynolds numbers characterize well the importance of fluid filament inertia observed in simulations of filament stretching gen-

FLUID	Newtonian		solution		melts	
v_0	0.09	0.3	0.3	0.6	0.09	0.3
$\dot{\varepsilon}_0$	0.006	0.02	0.02	0.04	0.02	0.04
Re	0.1	0.3	0.26	0.52	0.007	0.02
Ca	0.9	2.7	3.6	7.2	5.4	16.2
De	0	0	~ 0.7	~ 1.5	~ 3	~ 10
Bo	0	0	0	0	0	0

TABLE 3.1: Nondimensional groups for typical filament stretching simulations

erated with the motion of one of the end-plates. While our model Newtonian fluid may exhibit elastic properties at very high imposed stretching rates, the present simulations can safely be characterized by vanishing Deborah number.

3.4 Liquid-Wall Interface

Here we turn to the discussion of the liquid-wall interface properties which to some degree influence the dynamics of the filament deformation in the molecular dynamics simulations of uniaxial stretching of liquid filaments in the liquid bridge configuration.

It is been experimentally observed that the liquid structure at liquid-solid interfaces is characterized by formation of distinct liquid layers [42]. This layering effect is present in the molecular dynamics simulations involving solid boundaries, regardless of the specifics of the model for the boundary (Koplik *et al.* (1989) [43]). An illustration of the liquid layering effect at a solid end-plate in one of our

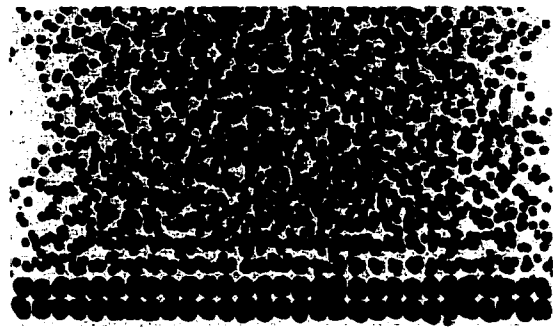

FIGURE 3.2: Layered liquid structure at the liquid-solid interface

equilibrium liquid bridge configurations is given in Fig. 3.2. Although entirely physical in origin, this liquid layering effect is not desirable in view of the small size of the simulated systems and the particular purposes of our simulations. A typical separation between liquid layers is of order $\mathcal{O}(\sigma_{LJ})$ so, in equilibrium, the presence of bounding end-plates drastically influences the structure of the liquid along about 25% of the length of the filament. Furthermore in liquid filament stretching simulations, high shear stresses at the liquid-solid interfaces may lead to violations of the no-slip boundary condition. The formation of the liquid layers at the solid end-plates might compromise attempts to ensure no-slip at the end-plates by means of a stronger attractive liquid-solid interaction, since this device just introduces a stronger liquid layering, with possible formation of additional layers. In the extreme cases the layers closest to the end-plates may act as an extension of the solid structure with the slip effectively occurring on one of the liquid layers. Both effects can occur in laboratory experiments as well, but there the size of the regions involved is quite small relative to that of the sample, and it is plau-

sible to neglect them in continuum-scale modeling. In the simulations reported here, the consequences of layering and possible slip are to add a bit of uncertainty to the interpretation. For example, the measurement of the liquid-wall force in our equilibrium liquid bridge configurations gives somewhat unexpected results which may be related to particular liquid structure at the planar solid boundaries and the small size of the simulated systems.

For static, axisymmetric Newtonian or non-Newtonian liquid bridges the equilibrium shapes are uniquely related to the liquid-wall force through the Young-Laplace equation,

$$F = \frac{2\pi\alpha R(z)}{\left[1+\left(\frac{dR(z)}{dz}\right)^2\right]^{\frac{1}{2}}} - \pi R(z)^2 P, \tag{3.12}$$

where P is the hydrostatic pressure inside the filament and $R(z)$ the position of the free surface. [1]

---

[1]More precisely this expression is the first integral of the Young-Laplace equation

$$P = \kappa\alpha \tag{3.13}$$

where κ is the mean curvature of a surface. In equilibrium $\kappa = const.$. In particular, for an axisymmetric surface

$$\begin{aligned}\kappa &= \frac{1}{R(1+R'^2)^{\frac{1}{2}}} - \frac{R''}{(1+R'^2)^{\frac{3}{2}}} \\ &= \frac{1}{RR'}\frac{d}{dz}\frac{R}{(1+R'^2)^{\frac{1}{2}}}.\end{aligned} \tag{3.14}$$

where $R' = \frac{dR}{dz}$. The equation (3.13) with the mean curvature given by the first expression in eq. (3.14) follows from the simple force balance analysis for a static axisymmetric free surface. In the equation (3.14) given in Szabo (1997) [19] R in the numerator of the second expression is missing.

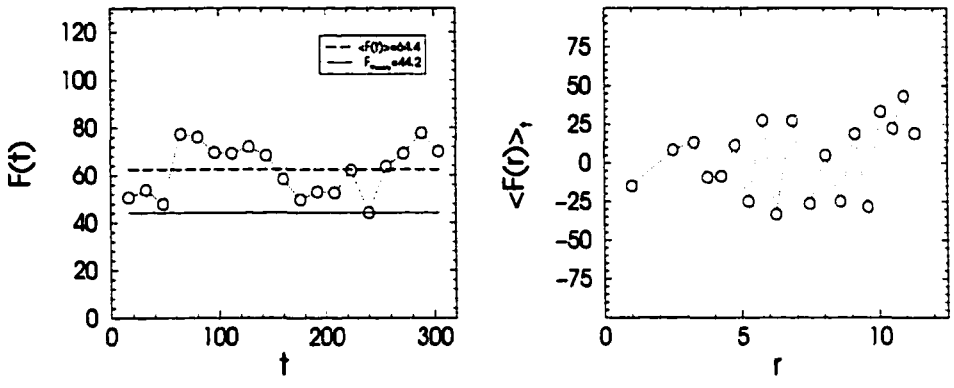

(a) (b)

FIGURE 3.3: (a) Variation of the liquid-wall force with time for the polydisperse melt filament in equilibrium. The solid line shows the Young-Laplace equation prediction based on the surface tension measurement in the planar surface geometry. (b) Distribution of the liquid-wall force across the end-plates.

In particular for cylindrical filaments,

$$R(z) = R_0 = const., \quad \text{and} \quad P = \frac{\alpha}{R_0} \tag{3.15}$$

lead to a simple relation between the tensile force and surface tension

$$F = \pi R_0 \alpha. \tag{3.16}$$

Instead the force measured in the approximately cylindrical liquid bridge configurations in equilibrium strongly depends on the strength of the interaction between the wall and liquid molecules. In the case of the monodisperse polymer melt bridge the force varies by approximately 30% around the value predicted by the

Young-Laplace equation (eq. (3.16)), and exhibits a strong time fluctuation. Similar behavior is exhibited by other model liquids. An illustration is presented in Fig. 3.3(a) which shows the variation of the liquid-wall force for the polydisperse melt filament in equilibrium. In this case, where the strengths of the repulsive and attractive contributions to the Lennard-Jones liquid-wall force are 0.6 and 1 respectively, the measured force, $F = 62 \pm 11$, is compared to the theoretical prediction $F_{theory} = 44.2$. The data have been obtained as time averages of the force over time intervals $\Delta t = 16$, which is fairly short compared to the longest relaxation time of the fluid, $\mathcal{O}(10^2 - 10^3)$, which may explain the large fluctuations of the measured force. However he averaging time is long compared to the characteristic time averaging intervals used in our filament stretching simulations, and Fig. 3.3(a) well illustrates the relative uncertainties involved in the force measurements. In Fig. 3.3(b) we show the distribution of the liquid-wall force across the end-plates for the same case of a polydisperse melt filament in equilibrium. The data shown are averages over the two end-plates, further averaged over the duration of the measurement $(\Delta t \approx 300)$. The strong fluctuations of the force in this case cannot be attributed to the short time averages, but rather characterize the liquid-wall interface itself. It appears that this behavior of the distribution of the liquid-wall force reflects the liquid structure near the planar boundary and does not significantly depend on the discreteness of the wall structure, since we observe the same result with very high density walls.

Thus far we have discussed some aspects of the liquid-solid interface in equilibrium, which have little qualitative dependence on the specific liquid-solid interaction. However the simulation of the liquid-solid interface in liquid bridge configurations subjected to extensions at high strain rates, in order to match experimental conditions in which one hopes to discern the extensional properties of test fluids, is non-trivial. Here we face the question, familiar to experimentalists, of just how to attach the ends of cylindrical fluid samples to the solid end fixtures effectively, so that particulars of the liquid-solid interaction do not interfere with reliable measurement of the response of fluid samples to the imposed deformation. In molecular dynamics simulations the problem is minor in case of simple model Newtonian or dilute polymer solution fluids. In these cases the no-slip condition at solid surfaces is well reproduced by a simple Lennard-Jones liquid-solid interaction, and the fast response of model Newtonian fluids to reasonable deformation rates ensures the integrity and uniform deformation of fluid samples. The situation is quite different in simulations involving models of polymer melts due to the strong tendency of long chains of atoms to slip on planar surfaces, as observed by Koplik and Banavar (1997) [44], for example. Indeed the effect can be so strong as to compromise the purpose of the simulation in the case of liquid bridge simulations at higher deformation rates. We illustrate this point in Fig. 3.4, where deformations of the model monodisperse polymer melt filament with (Fig. 3.4(a)) and without slip (Fig. 3.4(b)) are shown, in a simulation with constant stretching

(a) (b)

FIGURE 3.4: Influence of the slip at the liquid-solid interfaces on the liquid filament deformation in the filament stretching simulation.

rate $\dot{\varepsilon}_0 = 0.028$ (corresponding to the initial relative velocity of the end-plates $v_0 = 0.4$). In both cases the shifted Lennard-Jones interaction (eqs. (2.2),(2.3)) was used between liquid and solid atoms, but the two cases differ in the strength of the repulsive part: $a_r = 0.8$ giving slip in case Fig. 3.4(a), and $a_r = 0.6$ without apparent slip in Fig. 3.4(b). Physically, in the second case the reduced repulsion allows fluid atoms to "bind" more effectively to the solid. However, this approach to controlling the slip at solid surfaces cannot be reasonably extended very far because of the additional layering of the fluid near the surfaces and constraints on the choice of the integration time step imposed by the strong variation of the Lennard-Jones force with the interparticle distance.

There are additional features peculiar to molecular dynamics simulations of

small systems involving solid boundaries, which can influence the results for a liquid bridge subject to strong deformation by impulsive motion of the solid end-plates. One such issue is the influence of the specific formulation of the forcing and structure of the solid end-plates on the structure of the liquid at the solid surfaces and, more importantly, on the dynamics of the deformation of the fluid filament. In these simulations the solid boundaries are usually collections of oscillators tethered to a regular lattice of force centers by an elastic force

$$V_H = \frac{1}{2} k_H (\vec{r} - \vec{r}_e), \tag{3.17}$$

where $\vec{r}_e$ is the position of the force center of the solid atom at $\vec{r}$, and k_H is the force constant. Both the choice of the structure of the force centers and the strength of the force constant affect the structure of the fluid-solid interface. It was found that regularity of the lattice of force centers accompanied with large force constant, which results in a "hard"wall with smooth surface, induces particular regular molecular ordering in the adjacent fluid layers [43]. In addition such a wall is conducive to slip of the fluid at its surface. On the other hand "soft" walls with a regular structure, while not considerably reducing the fluid ordering may be penetrated by fluid atoms [45]. Moreover at the microscopic level the soft walls perform non-negligible oscillatory motion which may affect the dynamics of the liquid bridges subjected to a high rate elongation. A typical profile of the relative velocity of the

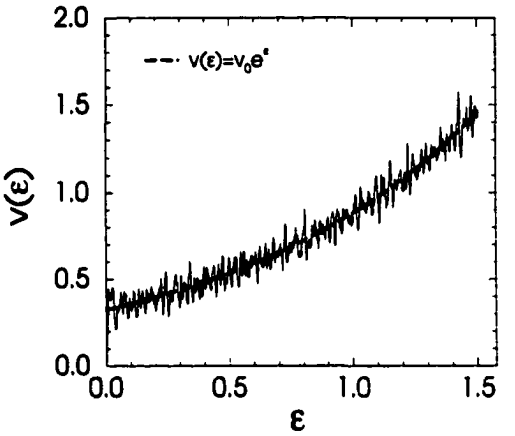

FIGURE 3.5: Velocity of the moving end plates as a function of Hencky strain ε. The dashed line represents the desired velocity profile for the rate of elongation $\dot{\varepsilon}_0 = v_0/L_0$ corresponding to the initial velocity $v_0 = 0.325$.

end-plates (defined in terms of the motion of the center of mass of each plate), where the motion of the end-plates is generated by appropriate translations of the force centers, is shown in Fig. 3.5. Although the similar collective motion is present in other molecular dynamics simulations of fluid flows in presence of solid boundaries without pathological consequences [46], it may be the source of uncertainties in the measured quantities that are important for the reliable description of the molecular dynamics simulation of the liquid bridge stretching experiment. In particular the measurement of the tensile force needed to generate the desired motion of the end-plates, which is measured as the total force between the fluid and solid atoms, may be adversely affected.

In order to address concerns regarding the stability of the fluid-solid interface, in the stretching simulations we have used irregular rigid end-plates with certain

number of fluid atoms explicitly attached to the end-plates. This structure was obtained by fixing the positions of solid atoms and involved fluid atoms (typically about 200 per wall) in an instantaneous configuration. This arrangement stabilizes the interface against the slip, reduces the fluid ordering next to the walls and avoids fluctuations in the end-plates velocity profile. It can be thought of as a solid-liquid interface where the liquid chemically reacts and sticks to disordered solid.

The influence of different arrangements of the liquid-solid interface on the dynamics of stretching of the polydisperse melt filament at stretching rate $\dot{\varepsilon}_0 = 0.02$ is illustrated in Fig. 3.6. The variations of the tensile force *vs.* Hencky strain for

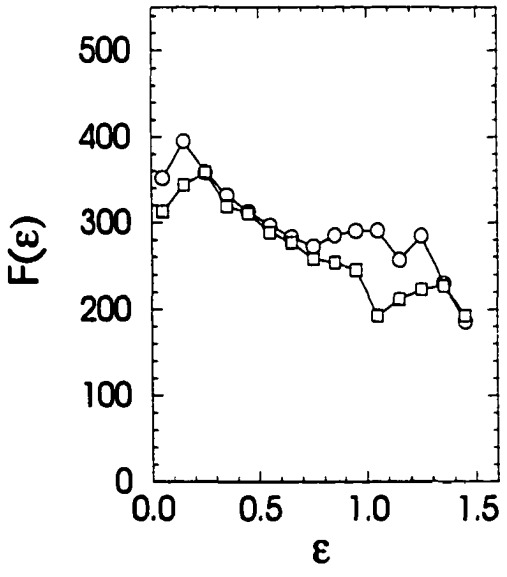

FIGURE 3.6: Liquid-wall force for the polydisperse melt filament for the cases where some liquid atoms are rigidly moved with the rigid walls (circles) and where the filament is deformed due to Lennard-Jones interaction with the solid walls constructed as set of oscillators (squares).

the cases with irregular rigid walls, and the usual solid walls comprised of the regularly distributed oscillators are compared. While the slow monotonic decrease of the tensile force characteristic for polydisperse polymer melts is well reproduced in both cases significant differences are seen at the beginning of stretching and at larger Hencky strains when the deforming filament becomes very thin. The variation of the tensile force at larger Hencky strains is particularly important for ascertaining strain-hardening properties of the fluid. While the configuration with the rigid walls leads to an increasing tensile force for Hencky strains $\epsilon \gtrsim 0.8$ indicating weak strain-hardening of the filament consistent with the results of the exploratory simulations at lower stretching rates, the irregular variation of the tensile force in the other case, observed for this and similar stretching rates, precludes reliable conclusion.

3.5 Numerical Algorithm

There is no general set of criteria for adequacy of numerical algorithms used in molecular dynamics simulations. In simulations of equilibrium or steady-state non-equilibrium properties, the important consideration is the of states from appropriate statistical ensembles. To achieve this goal, one does not need to generate exact classical trajectories. Instead the conservation of physical quantities which define the statistical ensemble is of primary importance and the choice of an appropriate numerical algorithm is based on its robustness and simplicity. For long

simulations, such as measurement of the material functions of model fluids for the steady planar shear flow, the velocity Verlet algorithm is probably the best choice. The algorithm requires the particle positions, velocities and accelerations at the same time t. First the particle velocities,

$$\vec{v}(t+\frac{1}{2}\delta t) = \vec{v}(t) + \frac{1}{2}\vec{a}(t)\delta t, \tag{3.18}$$

and positions are advanced,

$$\vec{r}(t+\delta t) = \vec{r}(t) + \vec{v}(t)\delta t + \frac{1}{2}\vec{a}(t)\delta t^2. \tag{3.19}$$

The forces $m\vec{a}(t+\delta t)$ are then calculated from eq. (3.19) and the velocity move to $t+\delta t$ completed,

$$\vec{v}(t+\delta t) = \vec{v}(t+\frac{1}{2}\delta t) + \frac{1}{2}\vec{a}(t+\delta t)\delta t. \tag{3.20}$$

The most important part of our simulations, the filament stretching experiment, is a transient process and here accuracy of the numerical algorithm is of primary importance. Following common practice, we have chosen a fifth order Gear predictor-corrector algorithm for second-order differential equations. Based on the comparison of performance of various numerical schemes in the measurement of the tensile force applied on the moving end-plates, this method offered the

most stable variation of the force. The variables in the method are scaled derivatives of the particle positions

$$x_\alpha^{(n)} = \frac{1}{n!}\frac{d^n x_\alpha}{dt^n}\delta t^n \qquad (x_\alpha = x, y, z; \quad n = 0, \ldots, 5). \tag{3.21}$$

First the values of the variables at the time $t + \delta t$ are predicted from their values at the time t,

$$x_{\alpha P}^{(k)}(t + \delta t) = \sum_{j=k}^{5} \binom{j}{k} x_\alpha^{(j)}(t). \tag{3.22}$$

The accelerations are then calculated from the predicted positions and used to correct the predicted values

$$x_\alpha^{(k)}(t + \delta t) = x_{\alpha P}^{(k)}(t + \delta t) + c_k^5[x_\alpha^{(2)}(t + \delta t) - x_{\alpha P}^{(2)}(t + \delta t)]. \tag{3.23}$$

The coefficients $c_n^5, (n = 0, \ldots, 5)$, are determined so as to ensure maximum accuracy and stability of the algorithm and their values depend on the particular definition of the variables, such as eq. (3.21). [2]

[2]There is some ambiguity about the value of the first corrector coefficient in this version of the algorithm. In his original work Gear [47] gives $c_0^5 = 3/20$, the value often cited in literature (e.g. van Gunsteren and Berendsen (1977) [48] and Allen and Tildesley (1987) [3]). Reference [3] gives another value, $c_0^5 = 3/16$, as the most appropriate for the systems with interactions that depend on particle velocities. Other authors (Evans and Morriss (1984) [49]) claim the former value to be erroneous and recommend the latter as the only value to use with the algorithm. Without claiming to have resolved the issue we have used $c_0^5 = 3/16$ which, under same initial conditions, yielded qualitatively the same but much smoother variation of the liquid-wall force.

4 Measurement and Calculation Procedures

In a typical molecular dynamics simulation, the quantities of interest are calculated as time averages over spatial sampling bins of finite size, whose definition is based on the macroscopic symmetries of the investigated system. Since typical simulations involve small systems, they are subject to significant statistical fluctuations, and this double averaging is usually needed to produce a robust signal above the noise. In case of equilibrium systems, the sequence of configurations generated by a molecular dynamics simulation is expected to fully sample the phase space of the relevant statistical ensemble, given enough time, since by the ergodic principle time averages are equivalent to ensemble averages. In non-equilibrium but steady-state processes, there is no equivalent principle with quite the same status, but it is believed on the basis of simulations and some experiments that *local* thermodynamic equilibrium is attained, and operationally one may proceed in much the

same way. In the case of transient processes, such as those treated in this work, the system is expected to change its macroscopic state in a finite time, and it is inappropriate to perform a long-time average. To obtain statistically stable results, one may instead average over ensembles of configurations generated from different but dynamically equivalent initial equilibrium configurations. This however demands considerable computational resources, and is unfortunately not feasible in the present work. The time averages used in our simulation of transient processes then correspond simply to the finite time resolution in macroscopic measurements.

The most important parameters in the uniaxial elongation of liquid filaments are the filament shape, and the external force needed to generate the desired motion of the end-plate(s). The measurement of the force is straightforward and has been already described. In the following we describe the measurement of the dynamical shapes of the elongating filaments along with the pressure and stress fields, the latter being particularly important since it has been recognized that the flow generated within the filament is not the ideal uniaxial elongational flow. The measurement of the stress distribution is then important for reliable interpretation of the experimental results, and a particular advantage of molecular simulation is that the stress is difficult to measure in the laboratory.

4.1 Sampling and Approximation of Simulation Data

Before discussing the procedures used in measurement and analysis of the filament shape and the pressure fields, we give a short account of the definition of the sampling bins that are necessary in spatial averaging as well as the data smoothing procedures employed.

Although the instantaneous configurations of the filaments are highly nonuniform we assume that they are axially symmetric on average and, during simulation, define the sampling bins as the axisymmetric regions enclosed between appropriately defined coaxial cylindrical surfaces and a family of planes parallel to the end-plates. The symmetry axis of the filament extending in the z-direction is the instantaneous z-axis through the center of mass of the entire filament at each time step. We define the family of equidistant bounding planes at the beginning of each time averaging interval and thereon treat them as the material planes of the filament. This means that during stretching of the filament with an externally imposed rate of elongation $\dot{\varepsilon}_0$, the position of the bin bounding planes is given by,

$$z(t) = z(0)e^{\dot{\varepsilon}_0 t} \tag{4.1}$$

where $z(0)$ is the initial position of a plane and t time elapsed since the beginning of the time interval. The physical basis for this choice is that in the case of ideal uniaxial elongational flow, the bin would contain the same Lagrangian element of

the filament in its axial dimension, over the time averaging interval. The practical advantage of this choice, over for example static bins, is that the bins can be defined so that all the bins adjacent to the liquid-solid interfaces are fully occupied at all times.

The resulting data is still noisy, particularly the pressure fields data and the distribution of the liquid-wall force, and these are approximated by their smoothed spline regressions. For this purpose we follow Dierckx [50], and make use of the Fortran routines supplied in this book. The procedure may be illustrated for the case of raw noisy data $z(x_i, y_i)$ defined a region of the x-y plane. An approximating spline $s_{k_x k_y}(x_i, y_i)$ of degrees k_x and k_y is determined by the requirement,

$$\sum_{i,j}\{[z(x_i, y_i) - s_{k_x k_y}(x_i, y_i)]^2\} \leq s \tag{4.2}$$

where s is a nonnegative constant which determines the smoothness of the approximant. In the extreme case of large s, the approximation returned is the least-square regression of corresponding order, while $s = 0$ gives a smooth interpolating spline. Therefore there is certain arbitrariness involved in the analysis and s is chosen so as to give reasonable balance between smoothness and faithfulness of the approximation. As an example consider the distribution of the liquid-solid force across the end-plates. Macroscopic considerations involved in the Young-Laplace equation state that the force that holds the bounding walls in equilibrium

is entirely due to surface tension of the liquid filament. At the same time surface tension creates the hydrostatic pressure in the filament, which tends to separate the end-plates. For the cylindrical filament this can be expressed in the following form

$$F = 2R_0\pi\alpha - R_0\pi\alpha \tag{4.3}$$

where α is the surface tension and R_0 the radius of the filament. The first term is the surface tension contribution and the second term is the hydrostatic pressure contribution. The force is directed inward, and consequently the force per unit area will be very small in the interior of the end-plate surface, with a sharp peak at the rim of the end-plate. This means that fluctuations in the force distribution in the inner part of the end-plates, as shown in Fig. 3.3(b), are macroscopically

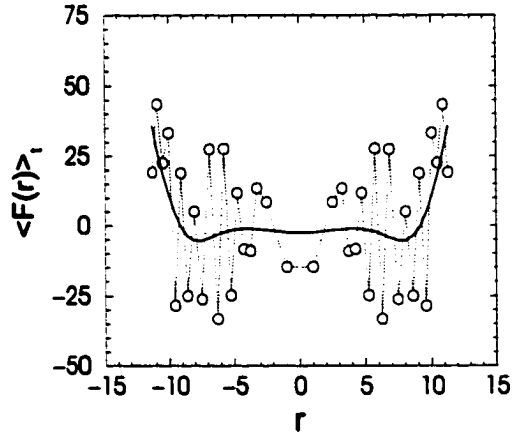

FIGURE 4.1: Smoothing approximation for the radial distribution of the liquid-wall force; $(s = 15250)$.

averaged out, while the peak at the rim of the end-plates remains. This serves as guidance in choosing the parameters of the spline approximation. The smoothing of the data shown in Fig. 3.3(b) is presented in Fig. 4.1. Here we use symmetrically distributed data in order to avoid the distortion of the approximant at the lower values of the data points array and to explicitly show the axial symmetry assumed in the measurement.

4.2 Shape and Minimum Radius of Fluid Filaments

Shapes and minimum radii of the stretching filaments were determined from the instantaneous configurations recorded at the beginning of each time averaging interval. This approach is analogous to imaging techniques used in real experiments, but in molecular dynamics simulations the particle distributions are clearly resolved and one has to somehow define the position of the free surface interface. The usual determination of the free surface position from an appropriate fit to the density profile quickly breaks down for the fast thinning fluid filaments. For a given resolution in the radial direction, which for axially symmetric filaments is determined by the radial width of the sampling bins, number of particles in a bin decreases roughly as the mean radius of the bin. As a consequence the radius of thin filaments cannot be reliably determined because of strong fluctuations in the density profile at small radii.

We chose to view the filament as a cluster of particles contained between the

end-plates, where a particle in the cluster has neighbors within distance $r_{cl} = 1.6\sigma_{LJ}$. The need for the treatment of a liquid element as a cluster of particles arose in studies of small spherical drops of a monatomic Lennard-Jones liquid. A discussion of the problem along with recommendations for the choice of the critical particle separation r_{cl} are given in Allen and Tildesley [3]. For the monatomic case, the simplest definition of r_{cl} could be based on the requirement that a particle moving in the radial direction with the average velocity will not get outside the range of interaction with the other particles in the cluster. We have avoided this problem by using chains of bonded atoms for both Newtonian and non-Newtonian liquids. The particular value of r_{cl} we use ensures that, in most cases, a whole chain is in the cluster if one of its atoms is in the cluster. However the instantaneous configurations may contain the chains protruding from the free surface. In order to avoid the inclusion of atoms on the far end of such chains in the cluster we require that a member of the cluster has at least three neighbors. Once the cluster is defined it is "scanned" through a moving window with a width of approximately σ_{LJ}. The exact thickness of the window is determined from the requirement that the whole filament be covered symmetrically with respect to the axial mid-plane. With the assumption that the filament is axisymmetric, a local radius is defined as the average of the radial distances of the four outermost particles in the four quadrants from the center of mass of the liquid slab contained in the window, and assigned to the center of the window. This definition is open to criticism as

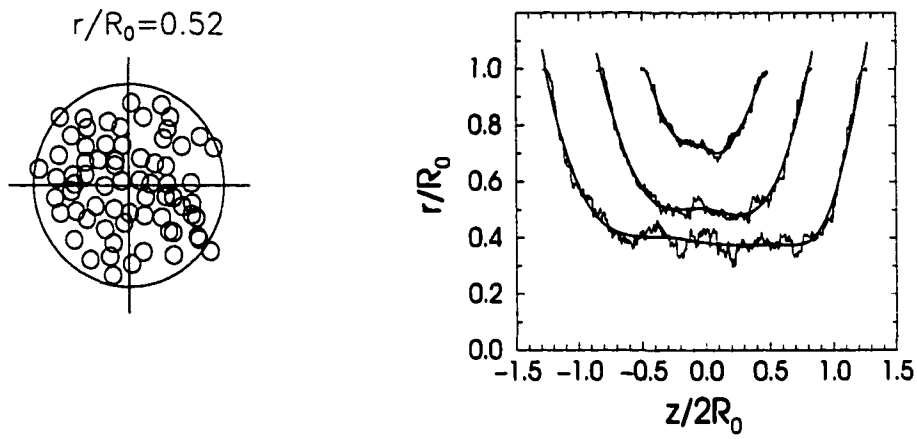

(a) (b)

FIGURE 4.2: Determination of the shape of a filament

too liberal but we found it necessary to be able to define a radius for very thin filaments. Eventually the shape of the bridge and associated minimum radius are obtained from cubic spline regressions. The whole procedure is illustrated in Fig. 4.2. The part (a) of the figure shows the axial view of a central slab of the solution filament subject to stretching with an overall stretching rate $\dot{\varepsilon}_0 = 0.042$ at Hencky strain $\varepsilon = 0.5$ while the part (b) shows 'raw' and smoothed shapes for the same simulation at Hencky strains $\varepsilon = 0.5, 1,$ and 1.4, respectively.

4.3 Pressure Tensor

The straightforward calculation of the microscopic Irving-Kirkwood pressure tensor, $P_{\alpha\beta}$, defined by eq. (2.9), gives directly the Cartesian components of the tensor, which are not the most appropriate for the stress within axially symmet-

ric fluid filaments. Noting that the microscopic pressure tensor is the sum of the single-particle contributions,

$$P_{\alpha\beta}(\vec{r}_B) = \frac{1}{V_B}\sum_{i\epsilon B} p_{i\alpha\beta}(\vec{r}_i), \tag{4.4}$$

the transformation to cylindrical components can be conveniently performed during the course of a run through the transformation

$$p'_{i\alpha\beta} = T_{\alpha\gamma}T_{\beta\delta}p_{i\gamma\delta}, \tag{4.5}$$

where the transformation matrix is given in terms of the azimuthal coordinate of the particle, φ,

$$T = \begin{bmatrix} \cos\varphi & \sin\varphi & 0 \\ -\sin\varphi & \cos\varphi & 0 \\ 0 & 0 & 1 \end{bmatrix}. \tag{4.6}$$

In particular,

$$\begin{aligned} p_{rr} &= p_{xx}\cos^2\varphi + p_{yy}\cos^2\varphi + 2p_{xy}\cos\varphi\sin\varphi \\ p_{rz} &= p_{xz}\cos\varphi + p_{yz}\sin\varphi. \end{aligned} \tag{4.7}$$

As with all other quantities, the pressure tensor was averaged over time interval corresponding to a constant increment in the Hencky strain, $\Delta\varepsilon = \dot{\varepsilon}_0 \Delta t = 0.1$.

In the analysis, the standard decomposition of the pressure tensor into isotropic pressure and the extra pressure tensor has been employed

$$P_{\alpha\beta} = P_{iso}\delta_{\alpha\beta} + \pi_{\alpha\beta} \tag{4.8}$$

where

$$P_{iso} = \frac{1}{3} Tr P_{\alpha\beta}, \quad \text{and} \quad \delta_{\alpha\beta} = \begin{cases} 1 & \text{if} \quad \alpha = \beta \\ 0 & \text{if} \quad \alpha \neq \beta. \end{cases} \tag{4.9}$$

Even more so than in analysis of the filament shapes, we are forced to rely on the macroscopic symmetries of the filament in the measurement and the analysis of the notoriously noisy components of the pressure tensor. (The origin of the noise is that the intermolecular force enters directly, and this quantity is a rapidly varying function of atomic position.) The assumed axial symmetry of the filament allowed us to use axially symmetric bins in the measurement of the pressure tensor, as well as other quantities of interest, such as velocity, density and temperature fields. To minimize the fluctuations in the measured pressure field, fairly large bins had to be used. The size of the bins was chosen so that the contents of the full bins be about $20 - 30$ particles. This was especially important to ensure a reliable calculation of

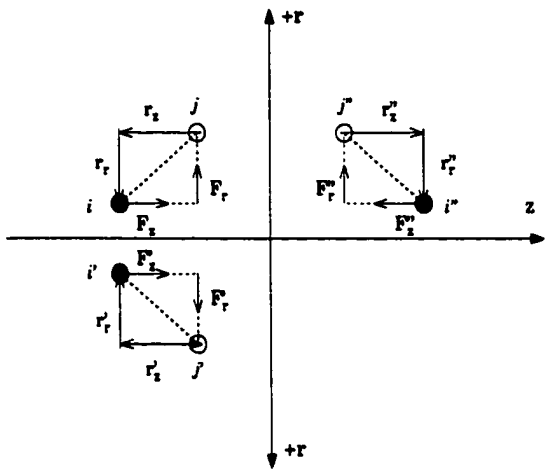

FIGURE 4.3: Symmetries of the filament stretched by simultaneous motion of both end-plates and associated transformation of quantities defining the configurational part of the pressure tensor. The r-axis is in the mid-plane of the filament and the z-axis is the axis of the filament.

the streaming velocity needed in the kinetic part of the pressure tensor, which we calculated at each time step. To further minimize the noise we use the symmetries of the pressure tensor components stemming from the symmetry of the filament stretched by the simultaneous motion of both end-plates with respect to the axial mid-plane. The symmetries of the filament along with corresponding transformations of the components of interparticle distance and force are illustrated in Fig. 4.3. On reflection with respect to the mid-plane,

$$
\begin{aligned}
r_r &\longmapsto r_r \\
r_z &\longmapsto -r_z \\
F_r &\longmapsto F_r \\
F_z &\longmapsto -F_z
\end{aligned}
\qquad (4.10) \qquad \Longrightarrow \qquad
\begin{aligned}
F_r r_z &\longmapsto -F_r r_z \\
F_z r_z &\longmapsto F_z r_z \\
F_r r_r &\longmapsto F_r r_r
\end{aligned}
$$

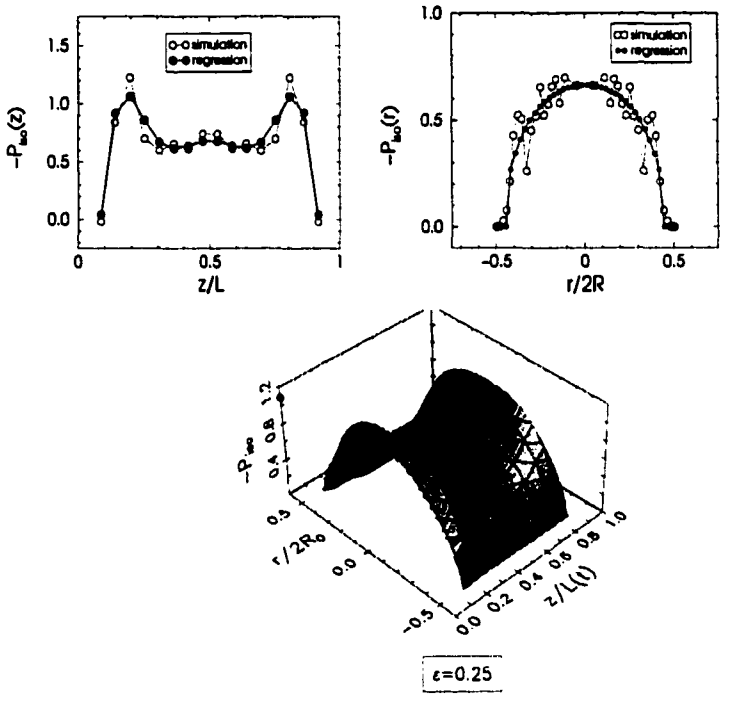

FIGURE 4.4: An illustration of the results of stress field data analysis

meaning that the radial and axial components of the pressure tensor, P_{rr} and P_{zz} are macroscopically symmetric, while the shear component P_{rz} is antisymmetric with respect to the mid-plane of the filament. In the analysis the data for these components have been averaged over bins placed symmetrically with respect to the mid-plane of the filament. Therefore our final results pertain to a quarter of the axial section through the center of the filament. However for the presentation purposes the distribution of the components of the stress tensor over the whole axial cross section of the filament will be shown for clarity. An example is shown in Fig. 4.4, along with the one-dimensional graphs of the stress distribution along the filament axis and across the mid-plane of the filament. These distributions were used as a graphical aid in the approximation of the stress distribution data.

4.4 Trouton Ratio

The goal of the filament stretching experiments and simulations is to extract the uniaxial extensional properties of fluid samples. Consider an idealized situation in which a cylindrical fluid sample undergoes an ideal extensional deformation, with a rate of extension $\dot{\varepsilon}_0$. The sample remains cylindrical throughout deformation and the time variation of its length and radius are given by eqs. (1.2) and (1.3),

$$\begin{aligned} L(t) &= L_0 e^{\dot{\varepsilon}_0 t} \\ R(t) &= R_0 e^{-\frac{1}{2}\dot{\varepsilon}_0 t}, \end{aligned} \tag{4.11}$$

respectively. The external tensile force, F, applied on the ends of the elongating filament, the outside pressure, P_{ext}, and surface tension forces are supported by the nonzero normal components of the pressure tensor within the filament,

$$\begin{aligned} P_{zz} &= -\frac{F}{R^2\pi} + P_{ext} + \frac{2\alpha}{R} \\ P_{rr} &= P_{ext} + \frac{\alpha}{R}. \end{aligned}$$

Uniaxial elongational viscosity, η_e, is then given by,

$$\begin{aligned} \eta_e &= -\frac{P_{zz} - P_{rr}}{\dot{\varepsilon}_0} \\ &= \frac{F}{R^2\pi\dot{\varepsilon}_0} - \frac{\alpha}{R\dot{\varepsilon}_0}, \end{aligned} \tag{4.12}$$

and, under these idealized conditions, could be determined from the measurement of the tensile force and the radius of the filament.

In real experiments with the filament stretching device, the situation is complicated by presence of gravity, inertial effects within the filament and the no-slip boundary condition at the bounding end-plates, which lead to nonuniform deformation of the fluid filament, further exacerbated by surface tension. As a result, the desired variations of the filament length and radius as given in eq. (4.11) can not be generated and the measurement strategy and the analysis of the experimental data have to be carefully investigated. In particular, the quantities to be measured and expressions analogous to eq. (4.12) must be identified. On the assumption that the gravitational and inertial effects are negligible, the simplest, and the least reliable approach is the straightforward application of eq. (4.12),

$$\eta_e^+ = \frac{F}{R^2\pi\dot{\varepsilon}_0} - \frac{\alpha}{R\dot{\varepsilon}_0}, \tag{4.13}$$

This assumption allows the determination of the elongational stress growth function, η_e^+, which is the appropriate material property to characterize the fluid response to transient flow generated in the device. Here $\dot{\varepsilon}_0$ is the stretching rate derived from the imposed exponential variation of the length of the filament and R is the radius of the fluid cylinder undergoing corresponding ideal uniaxial elongation.

Szabo (1997) [19] showed that the mean normal pressure difference $< P_{zz} - P_{rr} >$ across the mid-plane of the filament is related to the tensile force applied on the ends of the non-uniformly deforming filament by an expression similar to eq. (4.12), provided that the filament remains symmetric with respect to its mid-plane and axially symmetric throughout experiment. The meaning of this result is that the filament stretching device may provide reliable measurement of the uniaxial extensional properties of fluids, based on the response of the fluid element around the mid-plane of the test sample. Notice that, with the assumed symmetries, the mid-plane filament radius corresponds to the minimum radius of the filament. Two refinements to eq. (4.13) are then possible, demanding correspondingly more detailed measurements. Firstly the approximation of the ideal radial deformation of the filament can be replaced by the actual variation of the minimum filament radius, which is the characteristic radius of the deforming filament,

$$\eta_e^+ = \frac{F}{R_{min}^2 \pi \dot{\varepsilon}_0} - \frac{\alpha}{R_{min} \dot{\varepsilon}_0}. \tag{4.14}$$

Secondly, in the analysis of the measurement, the constant imposed stretching rate $\dot{\varepsilon}_0$ can be replaced by an effective rate of elongation derived from the measured minimum radius variation,

$$\dot{\varepsilon}_{eff} = -\frac{2}{R_{min}} \frac{dR_{min}}{dt} \tag{4.15}$$

giving

$$\eta_e^+ = \frac{F}{R_{min}^2 \pi \dot{\varepsilon}_{eff}} - \frac{\alpha}{R_{min} \dot{\varepsilon}_{eff}}. \tag{4.16}$$

The numerical investigation by Kolte *et al.* (1997) [20] showed that the expression (4.16) provides the best comparison to theoretical predictions for the measurements of the elongational stress growth function involving both strain-hardening, constant shear viscosity and shear thinning viscoelastic fluids, in the experiments with a constant imposed stretching rate $\dot{\varepsilon}_0$.

For this reason the expression (4.16) will be used exclusively in the analysis of the simulation results in this work in its usual nondimensional form,

$$Tr = \frac{\eta_e^+}{\eta_0} \tag{4.17}$$

called the transient Trouton ratio, in honor of Trouton (1906) who found that the elongational viscosity of mixture of pitch and tar was independent of the rate of elongation and equaled three times shear viscosity of the sample in agreement with the theoretical prediction for Newtonian fluids [51].

5 Results

5.1 Model Newtonian Liquid

In this section we present the results of the filament stretching simulation of the N=4 Newtonian model liquid.

5.1.1 Filament Shape Deformation

The instantaneous stretched configurations of the N=4 filament for various Hencky strains, up to breakup, are shown in Fig. 5.1. In this case overall stretch rate was $\dot{\varepsilon}_0 = 0.02$ ($Ca \approx 3, Re \approx 0.3$), corresponding to initial relative velocity of the end-plates $v_0 = 0.3$. Due to the no-slip boundary condition at the liquid-solid interfaces, the filament deforms non-uniformly throughout stretching. A cylindrical shape which would indicate the desired pure uniaxial elongation never develops at any portion of the deforming filament. The deformation is characterized by rapid thinning ('necking') in the central part of the filament, and the

(a) $\epsilon = 0.2$ (b) $\epsilon = 0.6$ (c) $\epsilon = 1$ (d) $\epsilon = 1.2$

FIGURE 5.1: Instantaneous configurations of the N=4 liquid filament

filament eventually breaks up in a manner classified characteristic of ductile failure. Qualitatively identical behavior was observed in a simulation that involved the same filament and the same microscopic initial configuration, with an initial end-plate relative velocity of $v_0 = 0.09$. (Note that all dimensionless numbers characterizing a simulation are proportional to v_0.) The variation of the minimum radius of the filament is presented in Fig. 5.2. In both cases the minimum radius decreases faster than it would in case of pure elongational flow within a filament, shown in the figure by the dashed line. Instead, at the beginning of stretching the minimum radius follows the curve corresponding to pure elongation with the higher rate of elongation $3\dot{\varepsilon}_0/2$, up to Hencky strain $\varepsilon \approx 0.4$. At larger Hencky

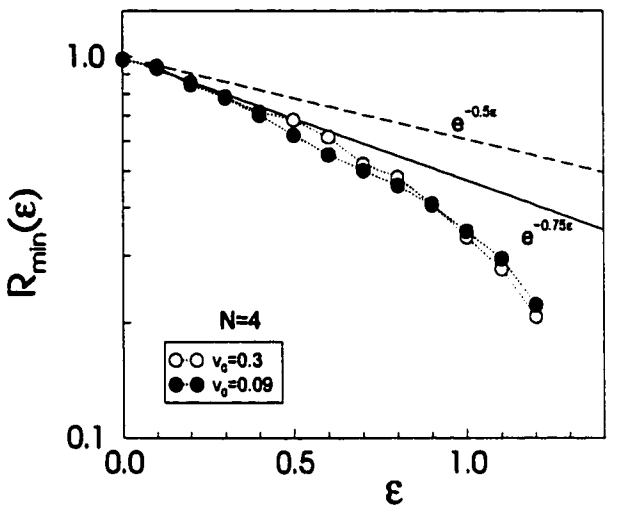

FIGURE 5.2: Minimum radius *vs.* Hencky strain for the Newtonian filament. The dashed line represents desired minimum radius variation corresponding to pure uniaxial elongation with the elongation rate implied by the variation of the filament length. The solid line is the variation predicted by lubrication model.

strains the minimum radius decreases even faster. This behavior, along with the overall shape dynamics, indicates that pure elongation does not occur during our filament stretching experiments with Newtonian filaments, except possibly at the center of the filament. Furthermore, even if that is the case, the elongation rate is not the one implied by the variation of the filament length but has to be derived from the variation of the minimum radius. The minimum radius variation is in excellent agreement with experimental observations of Spiegelberg *et al.* [11] and Solomon and Muller [12], as well as with numerical simulations results of Kolte *et al.* [20] and Sizaire and Legat [17]. It was recognized by Spiegelberg *et al.* [11] that the initial variation of the filament minimum radius is consistent with a re-

verse squeeze flow field within the filament, which can be satisfactorily described within the lubrication approximation. Experiments on number of Newtonian and polymeric liquids show that this type of initial behavior in a filament stretching experiment is largely independent of the rheological properties of the filament. Our simulations are in complete agreement with this observation.

As Fig. 5.2 shows, there is little or no difference in the variation of the minimum radius of the Newtonian filament for two overall rates of stretching, $\dot{\varepsilon}_0 = 0.007$ and 0.02, in the initial and final stages of deformation. The only difference is that the transition from the lubrication model prediction, to fast decrease in the filament radius leading to filament failure, is somewhat delayed in case of larger overall rate of stretching. A systematic investigation of the stretching behavior of polymer

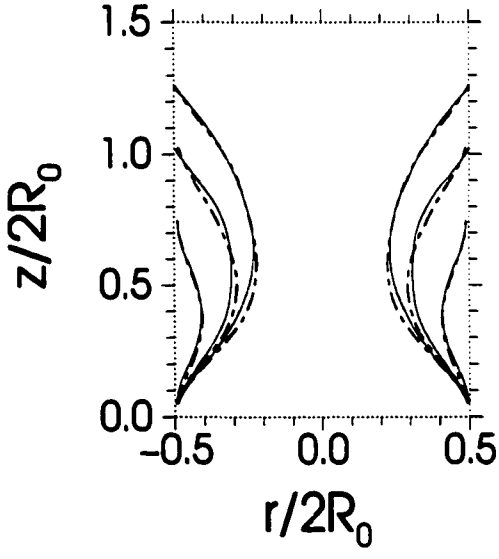

FIGURE 5.3: Comparison of the Newtonian filament shapes in $\dot{\varepsilon}_0 = 0.007$ (dot-dashed line) and $\dot{\varepsilon}_0 = 0.02$ (solid line) simulations

solutions and Newtonian liquids with viscosities matched to zero-shear viscosities of the solutions were performed by Kröger *et al.* [7] and Kröger and Rath [8]. Based on their experiments in which the liquid filaments were subjected to uniform stretching, they argue that the main parameter of experiment influencing the shape dynamics of the stretched filament is the capillary number. Experiments on any type of liquid, characterized with a larger capillary number yielded more uniform shapes accompanied with delayed transition to fast thinning leading to the filament breakup. Our results agree with their observation. The fact that the filament radii decrease identically prior to breakup can be explained by the small size of the filament. The filament shapes for the two stretching simulations of the Newtonian filament are compared in Fig. 5.3. Since both simulations were performed at relatively high capillary numbers the difference in the filament shapes is not large but is in qualitative agreement with the experimental results.

5.1.2 Force on the End-plates

The variation of the force exerted on the end-plates by the filament as a function of Hencky strain in the Newtonian simulations is presented in Fig. 5.4. In both cases the force is a monotonically decreasing function of strain, in qualitative agreement with both experimental observations and the results of numerical simulations. There is a difference in comparison to the initial stages of experiments, however. In experiment, the force reaches a maximum after an initial delay caused

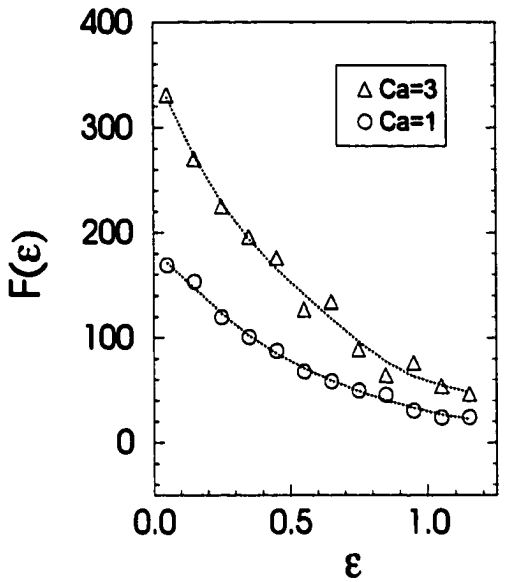

FIGURE 5.4: The force on the end-plates in Newtonian simulations. The dotted lines are smoothing regressions used in calculation of Trouton ratio.

by the inertia of the end-plate driving device. The effect is absent in our results since the initial velocity is set up abruptly at $t = 0$. Of course, the response of the filament is not ideal and instantaneous, but is fast enough to be absorbed in the time average.

The distribution of the force across the end-plates is shown in Fig. 5.5, for two values of Hencky strain. At the beginning of stretching, as can be seen from the $F(r)$ curve at Hencky strain $\varepsilon = 0.25$, surface tension is important and $F(r)$ has a sharp maximum at the rim of the end-plates. The distribution is much more uniform at later times, as illustrated by the $F(r)$ curve at $\varepsilon = 0.85$. In experiments in which the stretching of the filament is generated by the motion of one end-plate, the numerical simulation of Yao and McKinley (1998) [18] indicates the formation

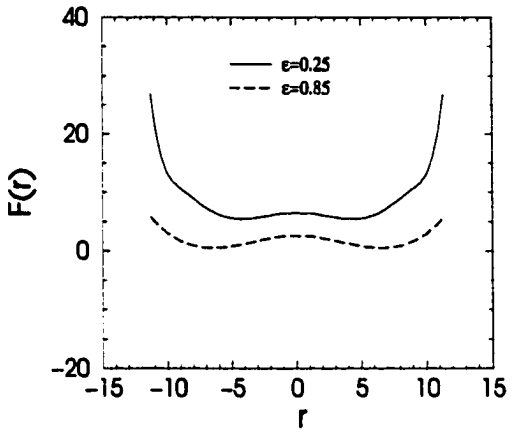

FIGURE 5.5: Variation of the tensile force across the end-plates in the Newtonian $Ca = 3$ simulation.

of static liquid reservoirs near the bounding plates in both Newtonian and elastic dilute polymer solution situations, which may lead to the negative sign in the liquid-wall force at late stage of stretching. We observe this effect in simulations where one of the end-plates is held stationary in the force on the stationary plate. The effect, however, is not likely at the moving plates since they continuously drag the adjacent fluid.

5.1.3 Axial Flow Kinematics

The radial component, $u_r(r)$, of the flow field can be discerned from the filament shape data. Here we present the results for the experimentally less tractable axial component, $u_z(z)$, of the flow field. Kröger and Rath (1995) [8] measured the velocity field within filament in a filament stretching experiment, but their experiments were conducted with an uniformly moving end-plate. In Fig. 5.6 we show

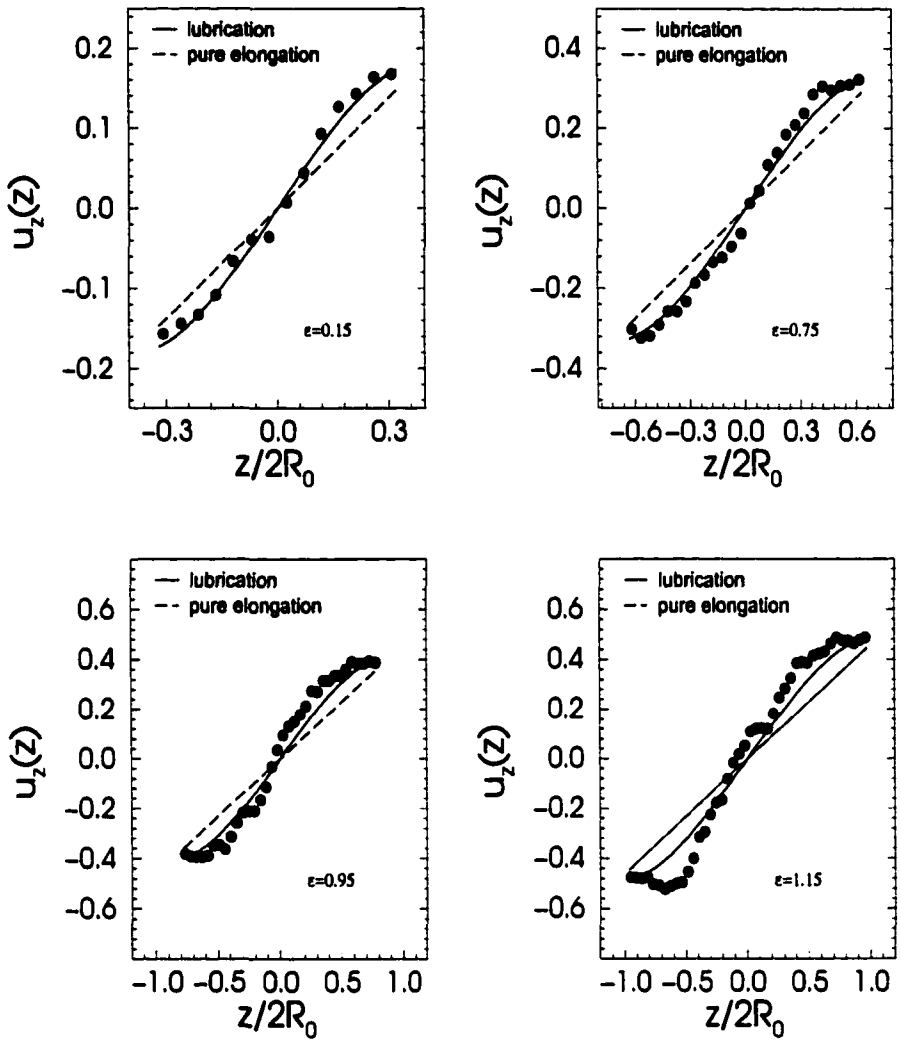

FIGURE 5.6: Axial velocity profiles for the Newtonian $\dot{\varepsilon}_0 = 0.02$ simulation.

the variation of u_z along the filament axis for our Newtonian simulation with the overall rate of elongation $\dot{\varepsilon}_0 = 0.02$; the data points were obtained by radial averaging over coaxial cylinders with radius $3\sigma_{LJ}$. The profiles of axial velocity are compared to the desired profiles corresponding to pure uniaxial elongation and to the lubrication model profiles given in Yao and McKinley (1998) [18], adapted

to the boundary conditions in our simulations were the filaments are stretched by simultaneous motion of both end-plates,

$$u_z(z) = v\left[3 - 2\frac{z+\frac{L}{2}}{L}\right]\left[\frac{z+\frac{L}{2}}{L}\right]^2 - \frac{v}{2}. \tag{5.1}$$

Here v is the relative velocity of the end-plates and L the length of the filament at time t. Agreement with the lubrication theory prediction is excellent for Hencky strains $\varepsilon \lesssim 1$. As the filament thins the static liquid reservoirs develop next to the end-plates and the axial velocity profile becomes steeper than both the pure elongation profile and the lubrication model prediction. This can be seen as a consequence of effective shortening of the portion of the filament that is being stretched.

5.1.4 Stress Distribution

The spatial and temporal variations of the stress tensor within a filament in course of the stretching experiment generally are not available experimentally. In the filament stretching experiment, the stress is not distributed uniformly due to the non-uniform deformation of the filament that results from the boundary conditions at the liquid-solid and free-surface interfaces. These conditions are also the source of numerical difficulties in the numerical simulations of the experiment, based on constitutive models. For this reason, a complete description of the stress field in the filament undergoing stretching deformation has not yet been given.

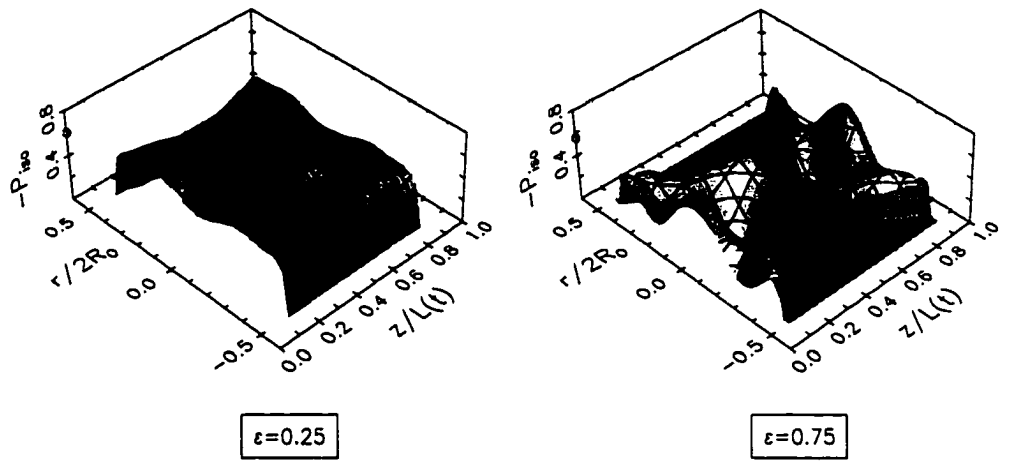

FIGURE 5.7: Distribution of the isotropic stress within Newtonian filament in $\dot{\varepsilon}_0 = 0.02$ simulation.

The uncertainties associated with the inherently strongly fluctuating stress in microscopic molecular dynamics systems notwithstanding, we believe that we are able to give a fairly complete and at least qualitatively reliable description of the stress field. In the following we will present the distributions of the stress components associated with the deformations of the Newtonian filament at early and late stages of the stretching experiment.

The isotropic stress distributions are shown in Fig. 5.7. As expected from the non-uniformities in the transient filament shapes, the distributions are spatially and temporally nonuniform. At early stages of the experiment, the isotropic stress is large and approximately uniform, along the central portion of the filament and at the free surface, indicating that at early times the viscous forces are strong enough to give a uniform deformation along the entire filament but nonuniform in the radial direction. The maximum at the free surface illustrates the importance of sur-

face tension, which is amplified by no-slip on the end-plates. The situation is very different at later times when the filament goes through accelerated thinning. The isotropic stress is still large and fairly uniform at the free surface, but nonuniform within the filament in both axial and radial directions. In the axial direction, $-P_{iso}$ has a sharp maximum located at the center of the filament, while deep minima develop in the regions next to the end-plates. These minima in the stress are related to formation of quasi-static liquid reservoirs at the end-plates at later stages of deformation. As the minima in the stress correspond to maxima in the pressure the presence of the quasi-static reservoir may result in the negative tensile force at the center of the liquid-solid interface at the stationary plate in the filament stretching experiments with one moving end-plate. In the simulations of these experiments, which we do not discuss in this document, we observed this effect in the simulations performed at relatively low stretching rates. The same result was obtained in the numerical simulation of the uniaxial stretching of Newtonian liquid bridges generated by the motion of one of the end-plates at a constant velocity by Gaudet *et al.* (1996).

The shear stress results are shown in Fig. 5.8. Due to the no-slip condition on the end-plates, at the beginning of stretching the shear stress is localized near the surface of the filament at the liquid-solid interface. As the stretching progresses, the surface layers of shear stress form in regions of high surface curvature.

The normal components of the total extra stress tensor, and the normal stress

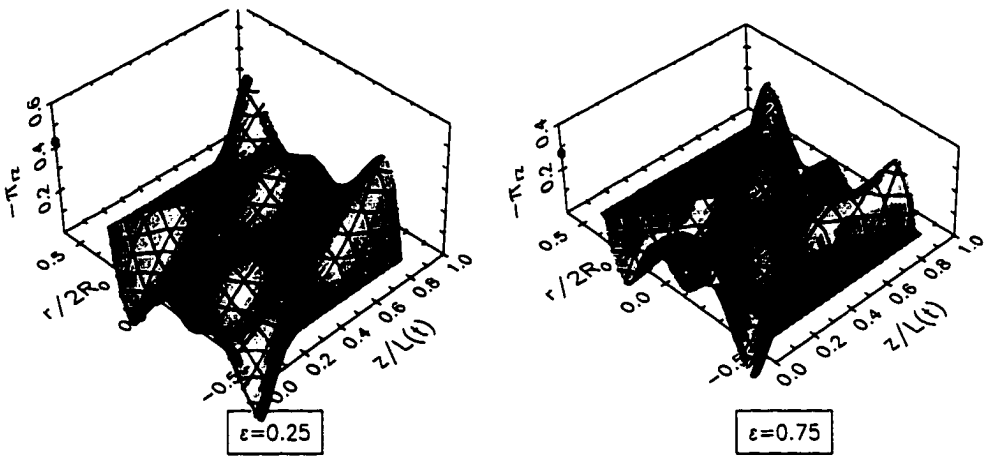

FIGURE 5.8: Distribution of the shear stress within Newtonian filament in $\dot{\varepsilon}_0 = 0.02$ simulation.

difference, $-(P_{zz} - P_{rr})$, are shown in Figs. 5.9, 5.10 and 5.11. The distributions of the normal components, $-\pi_{zz}$ and $-\pi_{rr}$, of the total extra stress tensor, are qualitatively similar to each other in shape throughout the stretching. They are characterized by surface layers of high positive stress, in the case of $-\pi_{zz}$, and high negative stress, in the case of $-\pi_{rr}$. The difference in sign comes from the different nature of deformation in axial (tension) and radial (compression) directions. The variation of both, $-\pi_{zz}$ and π_{rr}, within the filament along the filament axis is characterized my a maximum at the mid-plane of the filament and zero magnitude at the end-plates. As follows from its definition, and the similarity of distributions of $-\pi_{zz}$ and π_{rr}, the distribution of the normal stress difference is similar to those of $-\pi_{zz}$ and π_{rr}.

The distributions of the shear stress and the axial component of the total extra stress within Newtonian and highly elastic solution filaments are given in Yao and

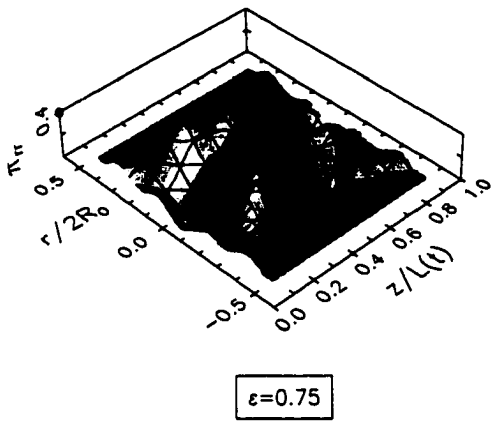

FIGURE 5.9: Distribution of the radial component of the extra pressure tensor within Newtonian filament in $\dot{\varepsilon}_0 = 0.02$ simulation.

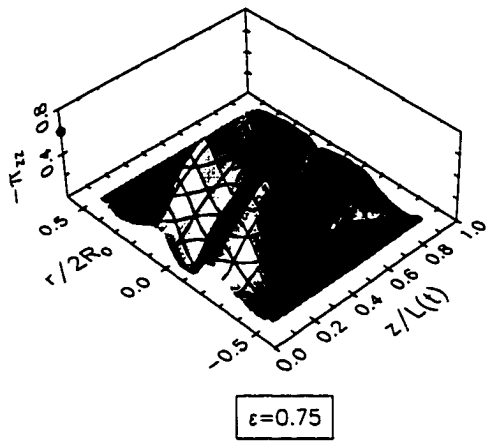

FIGURE 5.10: Distribution of the axial component of the extra stress tensor within Newtonian filament in $\dot{\varepsilon}_0 = 0.02$ simulation.

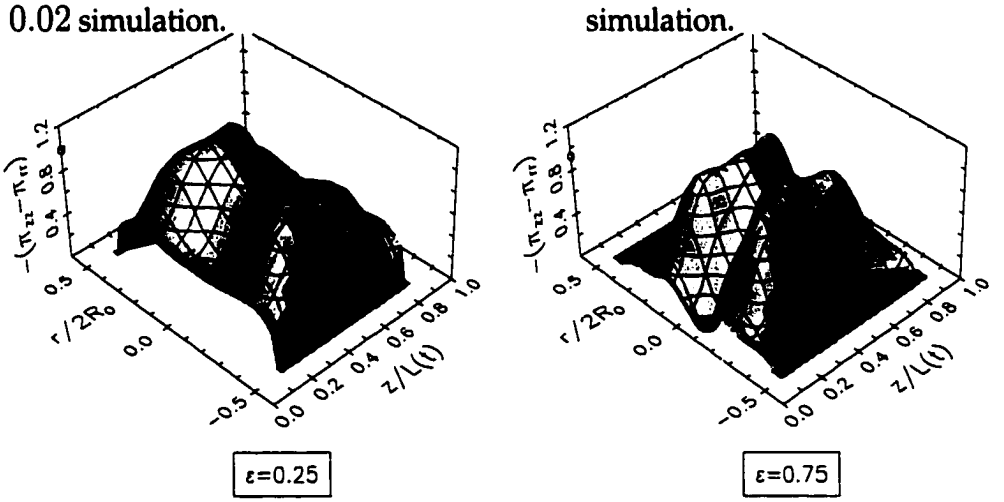

FIGURE 5.11: Distribution of the normal stress difference $-(P_{zz} - P_{rr})$ within Newtonian filament in $\dot{\varepsilon}_0 = 0.02$ simulation.

McKinley(1998) [18]. Our results agree qualitatively with their Newtonian result. Their calculation gives a surface layer of high $-\pi_{zz}$, which is more localized at the center of the filament along the surface than the corresponding layer obtained in our simulation. Also they obtained a parabolic axial profile of $-\pi_{zz}$ along the centerline with $-\pi_{zz} = 0$ at the end-plates.

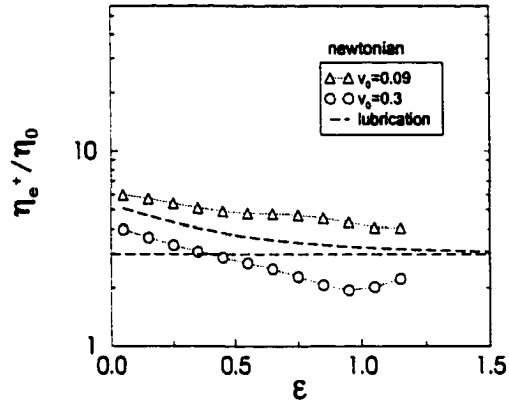

FIGURE 5.12: Elongational stress growth coefficient for the Newtonian model fluid. $v_0 = 0.09$ corresponds to $\dot{\varepsilon}_0 = 0.007$, and $v_0 = 0.3$ corresponds to $\dot{\varepsilon}_0 = 0.02$

An important characteristic of the isotropic stress and normal extra stress component distributions at relatively high strain levels is a fairly weak radial variation of stress at the mid-plane of the filament. According to the force balance analysis for the filament stretching device given by Szabo (1997) [19] this is enough for the filament stretching device to provide a reliable measurement of elongational viscosity of viscous Newtonian liquids.

5.1.5 Elongational Viscosity

Finally, in Fig. 5.12, we give the results for the elongational viscosity of our model Newtonian liquid. As can be seen, in the range of deformation available in our simulations, the Newtonian value for Trouton ratio $Tr = \eta_e^+/\eta = 3$ has not been obtained. Actually $Tr(\varepsilon)$ does not reach any constant value for either of overall rates of elongation employed in the simulations. However, for the simu-

lated range of Hencky strains, $\varepsilon \lesssim 1.2$, the results are in excellent agreement with the experimental results of Solomon and Muller (1996) [12], and Spiegelberg *et al.* (1996)[11] for viscous Newtonian oils. In the experiments of Spiegelberg *et al.*, after an initial overshoot the Trouton ratio decreases and eventually reaches the value $Tr = 3$ at Hencky strains $\varepsilon \gtrsim 1.5$, while in the experiments of Solomon and Muller, after the overshoot and subsequent decrease the Trouton ratio increases without ever reaching a constant value. Detailed investigation by Spiegelberg *et al.* indicates that the initial overshoot in Trouton ratio is a result of the small initial aspect ratio of the test samples and can be reduced by use of the longer samples.

5.2 MODEL SOLUTION

In this section we present the results of the filament stretching simulations involving the model solution filament. Instantaneous configurations of the filament with an imposed rate of elongation $\dot{\varepsilon}_0 = 0.04$ are shown in Fig. 5.13. The filament shapes at small strains are similar to those of the Newtonian filament at corresponding strains, as illustrated by the snapshot at $\varepsilon = 0.2$. However at strains $\varepsilon \gtrsim 0.6$, the shape of the solution filament evolves in a very different manner, leading to shapes characterized by an essentially cylindrical section extending over most of the filament length. This qualitative difference in the shape evolution of the Newtonian and solution filaments is starkly reflected in the time

(a) $\varepsilon = 0.2$ (b) $\varepsilon = 0.6$ (c) $\varepsilon = 1.2$ (d) $\varepsilon = 1.5$

FIGURE 5.13: Instantaneous configurations of the solution filament

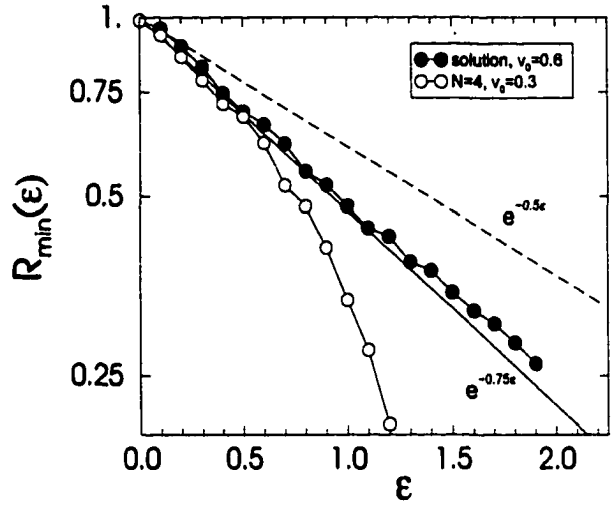

FIGURE 5.14: Minimum radius *vs.* Hencky strain for the solution filament in $\dot{\varepsilon}_0 = 0.04$ simulation. The corresponding data for the Newtonian $\dot{\varepsilon}_0 = 0.02$ simulation are shown for comparison

evolution of the corresponding minimum radii, contrasted in Fig. 5.14. At Hencky strains $\varepsilon \lesssim 0.6$, both filaments thin in the manner predicted by the lubrication model. At larger strains, however, the necking of the Newtonian filament accelerates, leading to breakup at Hencky strain $\varepsilon \approx 1.3$, while the solution filament in the same range of Hencky strains continues to thin at the rate predicted by the lubrication model. Simultaneously, the initially-developed depression in the mid-section of the filament becomes less and less pronounced. Eventually, at the strain level at which the Newtonian filament fails, the thinning of the solution filament slows down and the minimum radius *vs* Hencky strain curve acquires a constant slope closer to to the slope corresponding to pure elongation. This type of filament shape evolution is characteristic of the evolution of highly elastic dilute solution

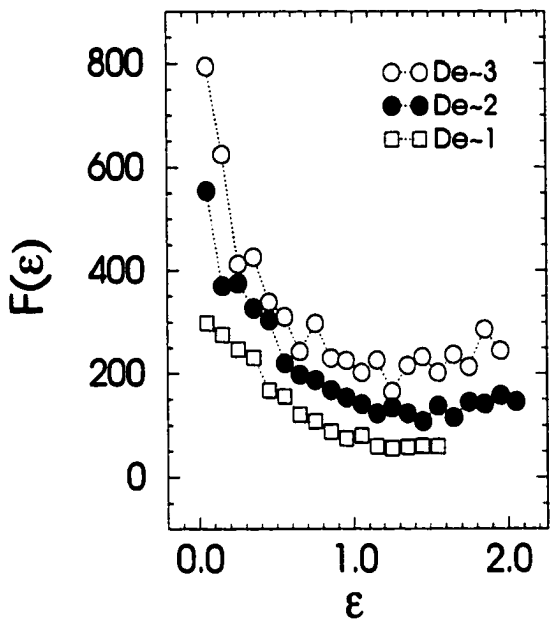

FIGURE 5.15: The force on the end-plates in the solution simulations.

filaments, where the development of the cylindrical shape is accompanied with an increase in the tensile force needed to maintain exponentially increasing velocity of the end-plate(s).

The time evolution of the tensile force in our simulations of solution filament stretching with different imposed rates of elongation is shown in Fig. 5.15. Again we see a similarity to the Newtonian case at small strains when the force decreases monotonically, and different behavior at Hencky strains $\varepsilon \gtrsim 1$ where the force stops decreasing, and for imposed rates of elongation $\dot{\varepsilon}_0 = 0.04, 0.06$ becomes an increasing function of imposed strain at strain levels $\varepsilon > 1.5$. The behavior of the solution filament in the $\dot{\varepsilon}_0 = 0.02$ stretching simulation is different in that the development of the cylindrical shape is slower and the filament fails at Hencky

strain $\varepsilon \approx 1.5$. As much as the filament failure is associated with the necking in the mid section of the filament, as in the Newtonian case, based on the trend in the force evolution we believe that the filament fails primarily because of the small amount of liquid present in the simulations.

The development of the cylindrical shape and an increasing tensile force are usually viewed as simultaneous processes and attributed to strain hardening. For strain hardening materials, the force needed to further deform the material increases with the strain level. In the case of a strain hardening filament the segment of the filament with the smallest radius experiences highest strain and becomes more resistant to further deformation than the rest of the filament. As a consequence the stresses tend to distribute uniformly over the filament leading to the more cylindrical shape. At the same time, as the strain level of the entire filament increases an increasing tensile force is needed to support the deformation. At a more fundamental level, the process is associated with uncoiling of long polymer molecules which simultaneously results in the more cylindrical shapes and larger forces needed to further stretch the polymer chains. Our simulations offer a slightly different mechanism, in which the formation of cylindrical shape associated with uncoiling of polymers precedes the increase in tensile force. Moreover, in simulations with filaments in solution, where the polymer chains were embedded in less viscous monatomic solvent, the cylindrical filaments developed without an associated increase in the tensile force.

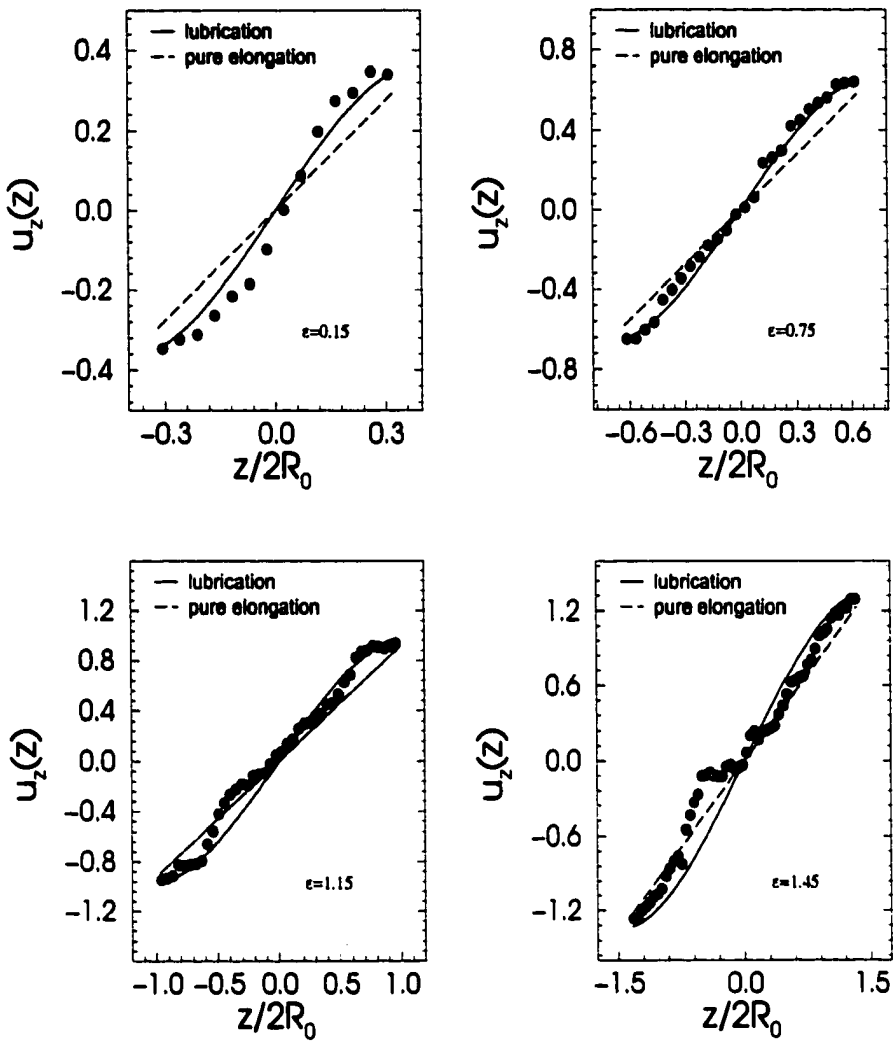

FIGURE 5.16: Axial velocity profiles for the solution $\dot{\varepsilon}_0 = 0.04$ simulation.

5.2.1 Velocity Field

The variation of the axial component, u_z, of the flow field along the axis of the filament at different strain levels is presented in Fig. 5.16. As in the Newtonian case at Hencky strains $\varepsilon \lesssim 1$, the axial velocity profile is given by the lubrication model. At larger strains, however, coinciding with the development of the

cylindrical section in the filament shape, the velocity profile becomes close to pure uniaxial elongation.

The axial and time variation of the axial velocity agree with the Oldroyd-B numerical simulation of Yao and McKinley (1998) [18].

5.2.2 Stress Field

We begin the exposition of the stress tensor distribution within the solution filament with the isotropic stress distributions shown in Fig. 5.17. The similarity to the corresponding distributions within the Newtonian filament at small Hencky strains are not obvious from the distribution of $-P_{iso}$ at the Hencky strain $\varepsilon = 0.25$. This point is emphasized in Fig. 5.17(b) where the corresponding radial variations of $-P_{iso}$ in the mid section of the filaments are compared. Although the variation is well captured qualitatively in the two-dimensional fit of isotropic stress data for the Newtonian case in Fig. 5.7, Fig. 5.17(b) offers more detailed insight. Both cases are characterized by surface layers of high stress and a maximum on the axis of the filaments. The differences between the two distributions, the broader maximum in the bulk of the filament in the radial direction and the more pronounced maxima at the end plates in the solution, case can be attributed to a larger imposed rate of deformation. This suggests that larger imposed rates of elongation might be preferable in a filament stretching experiment as they give a more uniform deformation across the filament, in view of the uncertainties in

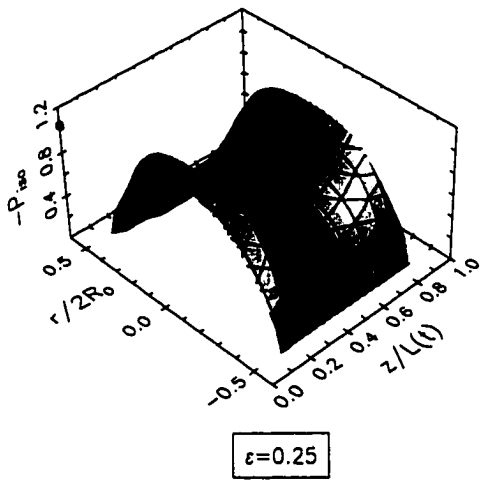

(a) Characteristic distribution of the isotropic stress within the solution filament at small Hencky strains

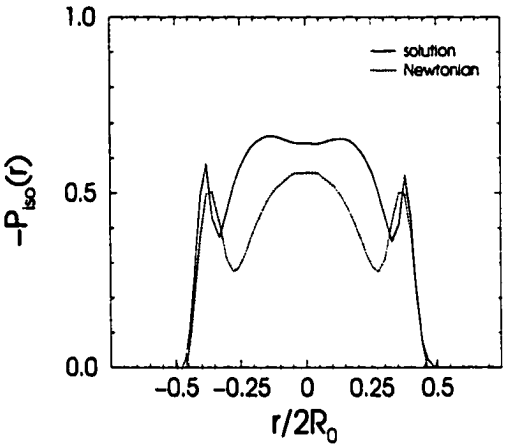

(b) Comparison of radial variation of $-P_{iso}$ at small Hencky strains for the solution and Newtonian case.

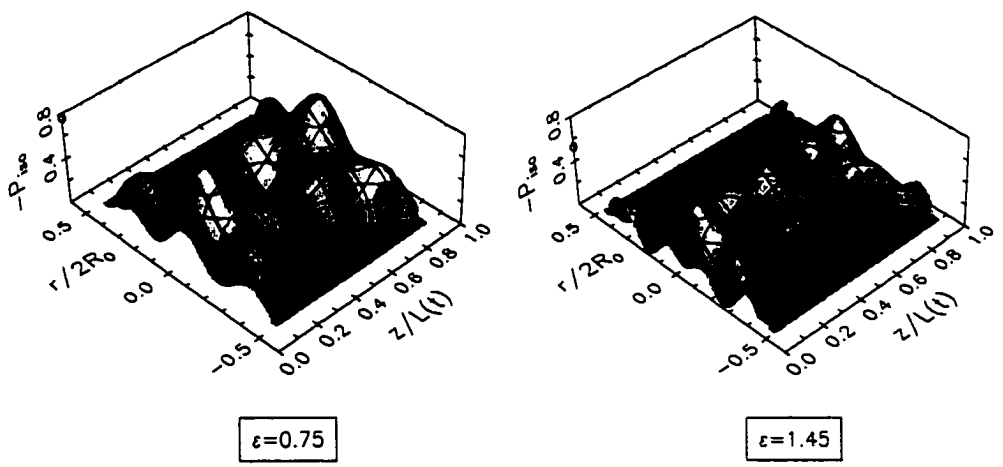

FIGURE 5.17: Distribution of the isotropic stress within the solution filament in $\dot{\varepsilon}_0 = 0.04$ simulation.

the interpretation of the experimental result introduced by the inhomogeneities of deformation in radial direction. At higher values of Hencky strain the broad minima at the end-plates reflecting the formation of the quasi-static liquid reservoirs observed at $\varepsilon \gtrsim 0.7$ in the Newtonian case become significant at much higher

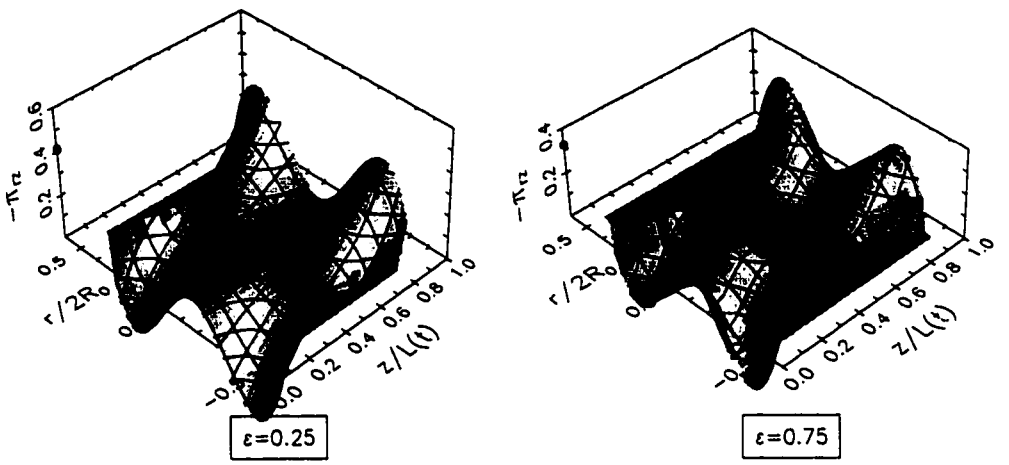

FIGURE 5.18: Distribution of the shear stress within the solution filament in $\dot{\epsilon}_0 = 0.04$ simulation.

strains in the solution case as illustrated in Fig. 5.17.

The shear stress distributions for the solution simulation is shown in Fig. 5.18. In comparison to the Newtonian case we see the absence of shear stress deep within the filament even at small strains. At higher strains the cylindrical section of the filament is essentially shear free. As in the Newtonian case, the shear stress is localized at the surface region of high curvature. However in this case the part of the free surface with high curvature does not extend into the filament as far from the end-plates as in the case of the Newtonian filament. This observation contradicts the results of the numerical simulation of Yao and McKinley (1998) [18] which predicts complete disappearance of the shear stress surface layer in the Newtonian case at larger strains.

The distributions of the normal components of the total extra stress tensor and the normal stress difference is presented in Figs. 5.19 and 5.20. The trend of time

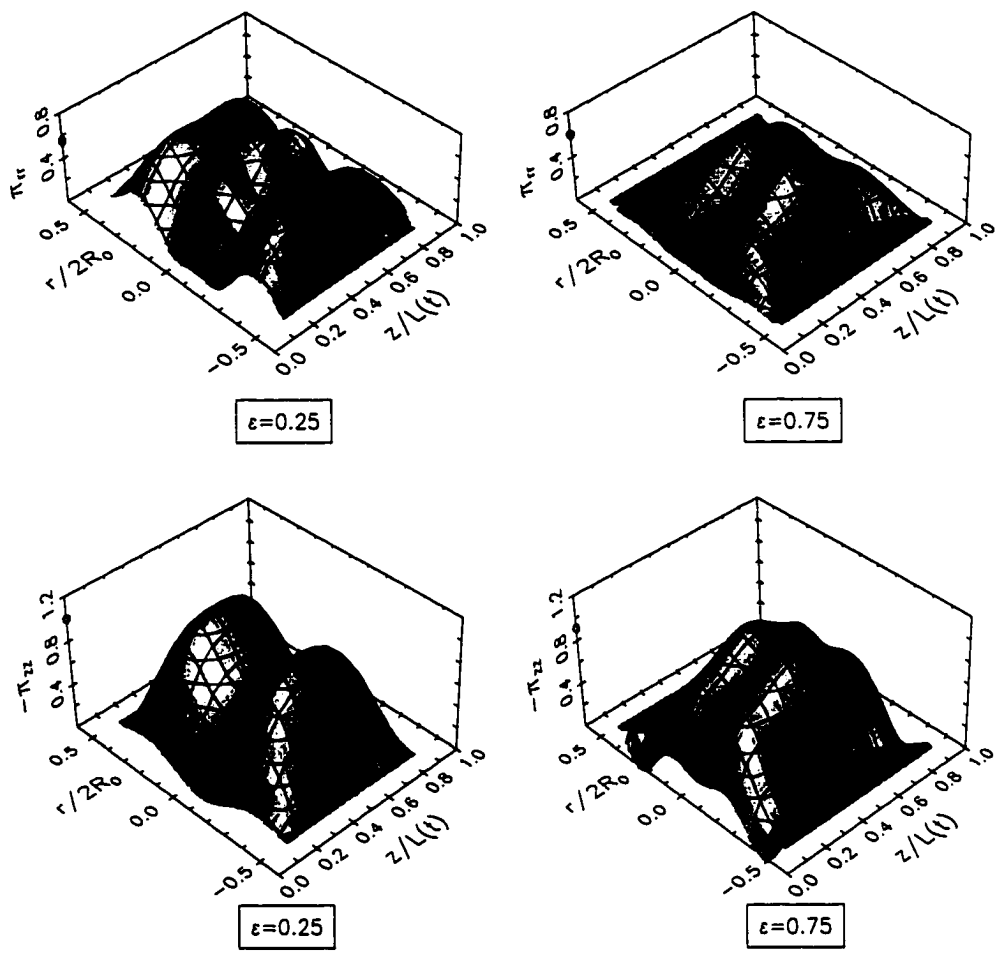

FIGURE 5.19: Distribution of normal components of the total extra stress tensor within the solution filament in $\dot{\varepsilon}_0 = 0.04$ simulation.

variation of stress distribution in comparison with the corresponding Newtonian distributions seen in the previous cases remains the same. Here we point to more pronounced surface layers in the solution case in the mid section of the filament in comparison to stress levels on the axis of the filament. This behavior agrees with the Oldroyd-B numerical simulation of Yao and McKinley (1998). Further agreement can be seen in the axial variation of the axial component of the total

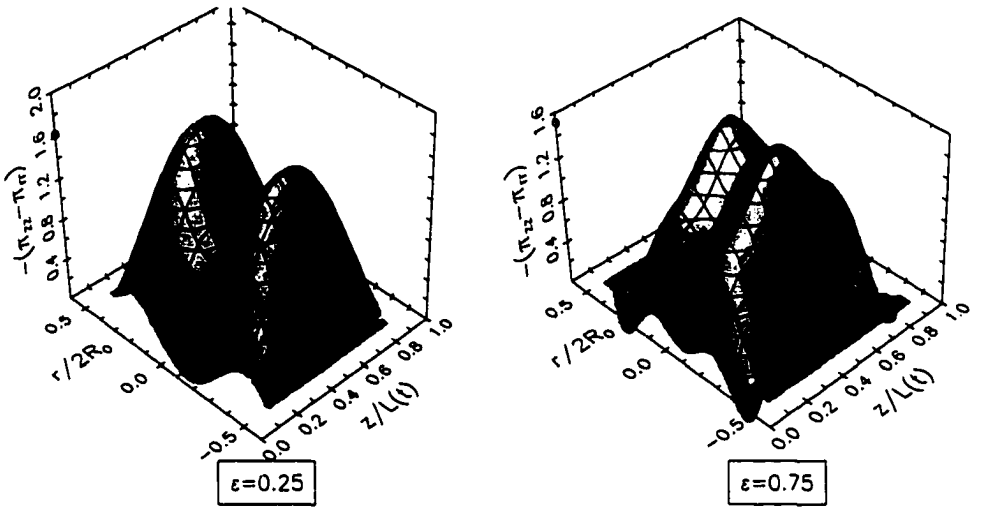

FIGURE 5.20: Normal components of the total extra stress tensor and normal stress difference within the solution filament in $\dot{\epsilon}_0 = 0.04$ simulation.

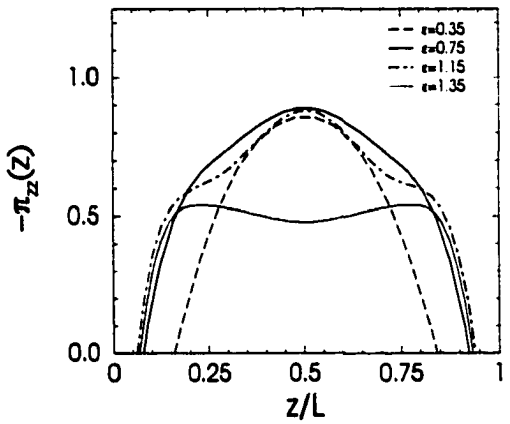

FIGURE 5.21: Variation of the axial component of the total extra stress tensor $-\pi_{zz}$ along the axis of the solution filament.

extra stress tensor, $-\pi_{zz}(z)$, shown in Fig. 5.21, where the initial parabolic variation predicted by the lubrication model at small Hencky strains followed by the formation of additional stress boundary layers near the end-plates is observed. However, significant qualitative and quantitative differences exist. The numerical simulation predicts a maximum in $-\pi_{zz}(z)$ located at the center of the filament

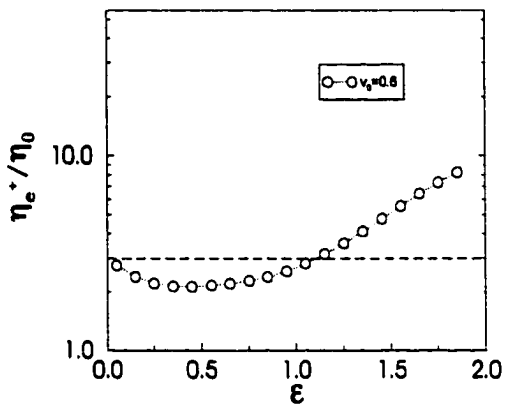

FIGURE 5.22: Elongational stress growth coefficient for the model solution in $\dot{\epsilon}_0 = 0.04, De \approx 2$ simulation

with a temporally monotonically increasing magnitude. Our simulation gives a constant maximum in the middle of the filament throughout the initial phase and during the phase of deformation where the cylindrical section of the filament is being formed. The $-\pi_{zz}(z)$ curve is much more uniform within the cylindrical section of the filament, with a minimum in the middle of the filament. According to the numerical simulation, this distribution is typical for large Hencky strains in viscoelastic experiments with large initial aspect ratio filaments.

5.2.3 Transient Elongational Viscosity

Transient elongational viscosity for the solution simulation with the imposed stretching rate is shown in Fig. 5.22. For small Hencky strains, $\varepsilon \lesssim 0.5$, the Trouton ratio decreases in agreement with the Newtonian character of deformation at small strains. Qualitatively, the variation of Trouton ratio reinforces the agreement

with the experiments of Spiegelberg *et al.* (1996) [11] on Newtonian oils, where the initial overshoot of the Newtonian value is inversely proportional to the imposed stretching rate. Incidentally, in this case we do not observe an overshoot but the initial variation is qualitatively the same to the variations of Trouton ratio for the Newtonian simulations shown in Fig. 5.12. For the range of strains available in our simulation, the variation of the Trouton ratio is in an excellent agreement with experimental results of Spiegelberg *et al.* [11] except that the upturn in $Tr(\varepsilon)$ curve is shifted to smaller Hencky strains. The same qualitative behavior is obtained in numerical Oldroyd-B (Yao and McKinley (1998) and Kolte *et al.* (1997)) and FENE-CR (Sizaire and Legat (1997)) constitutive models numerical simulations.

(a) $\epsilon = 0.4$ (b) $\epsilon = 0.7$ (c) $\epsilon = 1.2$ (d) $\epsilon = 1.4$

FIGURE 5.23: Instantaneous configurations of the polydisperse melt filament

5.3 MODEL MELTS

In this section we discuss the simulation results for the model polymer melts. The instantaneous configurations of the systems for different strain levels in $\dot{\varepsilon}_0 = 0.02$ simulations are shown in Figs. 5.23 and 5.24. The filaments deform very similarly at small Hencky strains and, as will be demonstrated shortly, in the manner the predicted by the lubrication model of Spiegelberg *et al.* (1996) to describe the initial response of Newtonian and highly elastic dilute solution filaments to stretching deformations. In neither case does the cylindrical section characteristic of the deformation of strain hardening materials appear. In that respect the deformation is more similar to that of the Newtonian filaments than to that of the dilute polymer solutions. However, at larger Hencky strains, the melt fila-

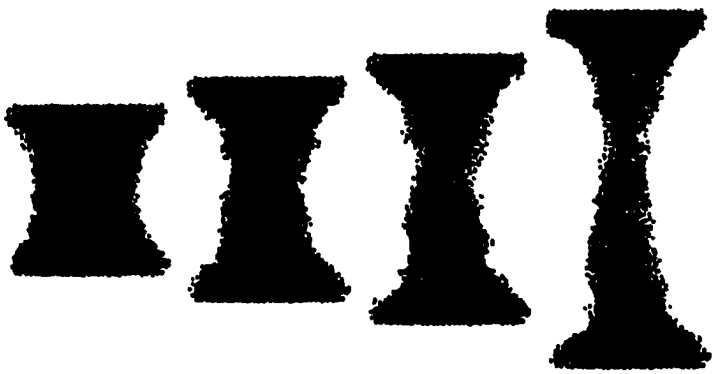

(a) $\epsilon = 0.4$ (b) $\epsilon = 0.7$ (c) $\epsilon = 0.9$ (d) $\epsilon = 1.2$

FIGURE 5.24: Instantaneous configurations of the monodisperse melt filament

ments develop more cylindrical shapes than the Newtonian filament under same imposed stretching rate. At larger Hencky strains, $\varepsilon \gtrsim 1$, there are significant differences in the deformation of the two melt filaments. As is indicated by the configuration at Hencky strain $\varepsilon = 1.4$, Fig. 5.23(d), although the polydisperse melt filament can be stretched to high Hencky strains (up to $\varepsilon = 2.5$), the density distribution within filament becomes progressively more nonuniform as the stretching progresses. Monodisperse melt deformation at this range of stretching rates and Hencky strains is characterized by the development of ruptures in the free surface, as can be seen in Figs. 5.24(c) and (d). This effect is reminiscent of ruptures of narrow molecular weight distribution polymer melts, where the rupture of the sample, with or without necking, had been observed earlier. The effect has not been systematically investigated experimentally and is not well

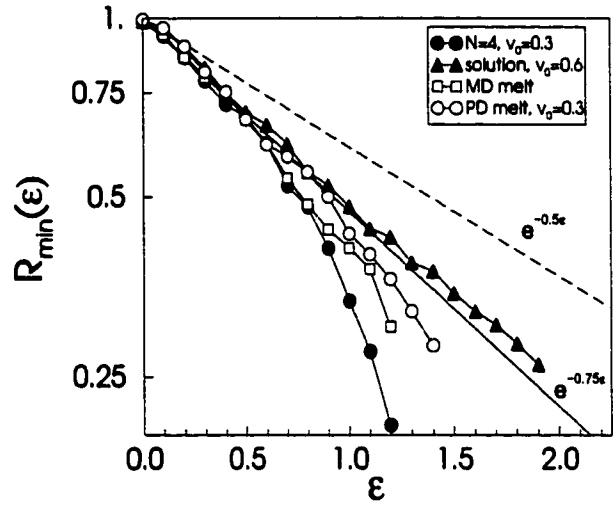

FIGURE 5.25: Minimum radius *vs.* Hencky strain for the melt filaments.

understood theoretically. The systematic investigation of stretching behavior of monodisperse melts has also been outside the scope of this work. However our simulations indicate that a molecular dynamics investigation of the subject might be worth pursuing.

The minimum radius variation during stretching of the model melt filaments is shown in Fig. 5.25. For comparison we include the corresponding data for the Newtonian and solution filaments. As can be seen the rate at which the minimum radii of the melt filaments decrease falls between those of the strain hardening solution and fast-thinning Newtonian filaments. The slight upturn in the slope of the monodisperse melt curve in the range of Hencky strains $0.7 \leq \varepsilon \leq 1.1$ should not be interpreted as strain hardening effect, since it comes from the different depth of the rupture in the free surface of the filament.

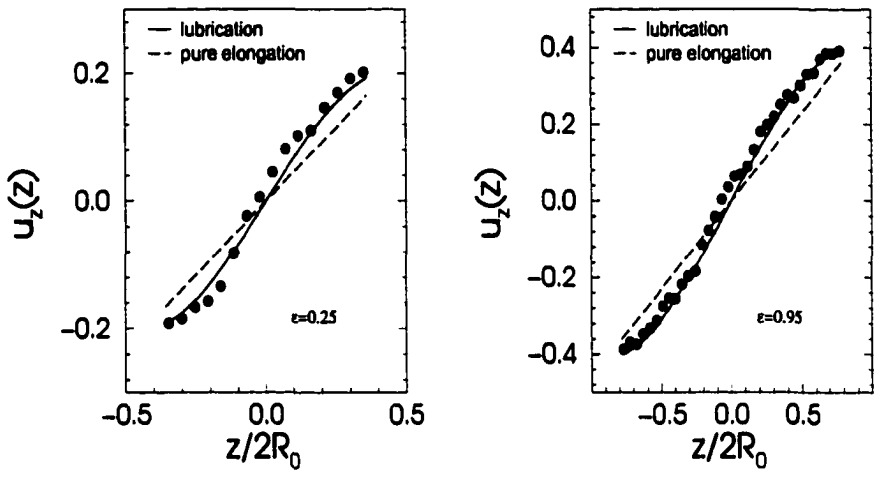

FIGURE 5.26: Axial velocity profiles for the polydisperse melt in $\dot{\varepsilon}_0 = 0.02$ simulation.

Before we turn to discussion of the tensile force and the stresses within the melt filaments, we wish to point to further similarities between the stretching deformation of the melt filaments and the Newtonian filament, exhibited in the flow kinematics within the filament. As shown in Fig. 5.26 the axial velocity profile along the axis of the filaments, which is very similar for both model melts, is that predicted by th lubrication model for the Newtonian filament response to stretching deformation.

The tensile force variation *vs.* Hencky strain for the two melt cases is presented in Figs. 5.27(a) and (b). Notice the similarity of the tensile force variation of the monodisperse melt to that of the Newtonian case. Indeed, it had been observed experimentally that besides peculiarities in the behavior of the monodisperse polymer melts at high imposed stretching rates and high levels of strain they exhibit, an almost linear viscoelastic stretching behavior. At least qualitatively the results

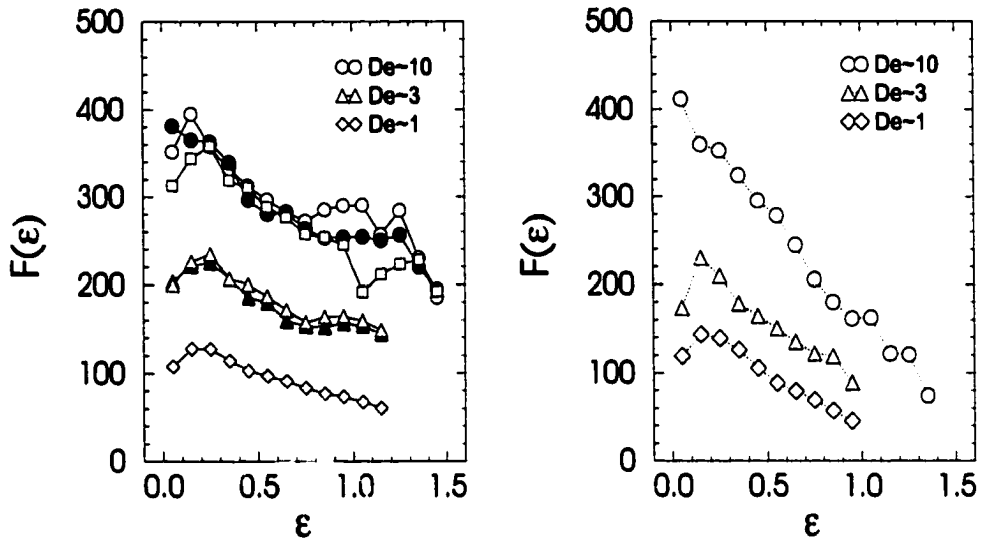

(a) Polydisperse melt (b) Monodisperse melt

FIGURE 5.27: Tensile force *vs.* Hencky strain for model melts

of our simulations for the tensile force are in agreement with this observation. A significant differences with respect to the tensile force behavior for the two melts can be seen at both early and late stages of stretching deformations in the simulations with high imposed stretching rates. The early response of the monodisperse melt is faster than that of the polydisperse melt, which can be attributed to the spectrum of long time constants characterizing the polydisperse melt.(Kolte *et al.* (1997)). While the tensile force needed to maintain the constant stretching rate decreases monotonically throughout stretching of the monodisperse filament for all investigated imposed stretching rates, the variation of the tensile force in the polydisperse melt simulations at higher imposed stretching rates ($De \gtrsim 3$) indicates

weak strain hardening of the filament. Once more we remark on the uncertainties in the extensional properties contained in the tensile force variation due to the structure of the liquid-solid interface, and slightly different polymer content employed in the stretching simulations of the polydisperse melt filament. We show three cases for the $\dot{\varepsilon}_0 = 0.02$ and two cases for the $\dot{\varepsilon}_0 = 0.007$ pertaining to different conditions employed in the simulations in Fig. 5.27(a). The open circles in the $De \approx 10$ simulations show the variation of the tensile force in the simulation, where a certain number of liquid atoms were explicitly bound to the end-plates and one long chain stretched along the filament, one of its atoms fixed at one end-plate. In this case, as well as in the $De \approx 3$ simulation shown with open triangles, the filament clearly exhibits an increase in the tensile force at Hencky strain $\varepsilon = 0.8$. The corresponding filled symbols pertain to same liquid-solid interface but the long chain cut in half. While in this case no difference was observed in the tensile force variation at $De \approx 3$ simulations the behavior of the tensile force in the $De \approx 10$ simulations is inconclusive. The third case in the $De \approx 10$, shown by the open squares pertains to a simulation with the long chain but a Lennard-Jones interaction at the liquid-solid interfaces. Again the increase in the tensile force had been observed but after a significant drop in its magnitude as compared to the previous data point. Also in this case a shift in the tensile force curve to higher strains is observed as compared to the case where the liquid atoms were explicitly fixed to the end-plates.

5.3.1 Stress Fields

The distributions of the components of the stress tensor within model melt filaments are cataloged in Figs. 5.28, 5.29, 5.30, 5.31 and 5.32. In the range of Hencky strains where a meaningful two-dimensional approximation of stress data could be made, the measured stress field for the two model melt fluids exhibit similar overall distributions. In comparison to corresponding stress distributions within Newtonian and solution filaments, differences due to the elastic properties of the filaments can be seen. First, the surface layers of high stress concentrations at the mid-filament region are relatively weaker in the melt filaments than in both Newtonian and solution cases. The regions of large isotropic pressure that develop in the Newtonian and solution filaments as a consequence of the formation of the quasi-static fluid reservoirs at the regions adjacent to the end-plates are, at the same strain levels, completely absent in the melt filaments. Instead high stresses are observed. Furthermore the radial distribution of isotropic stress is characterized by pronounced maxima on the axes of the filaments. A highly elastic response, characterized by pronounced maxima in the distributions of the normal stress components located in the center of the filaments, was observed at the beginning of stretching. Our results indicate that relatively weak high stress surface layers in the distribution of the normal stress difference are primarily contributed by the radial component of the stress tensor. Indeed, the measurements indicate surprisingly uniform radial distribution of the axial component of the extra stress tensor

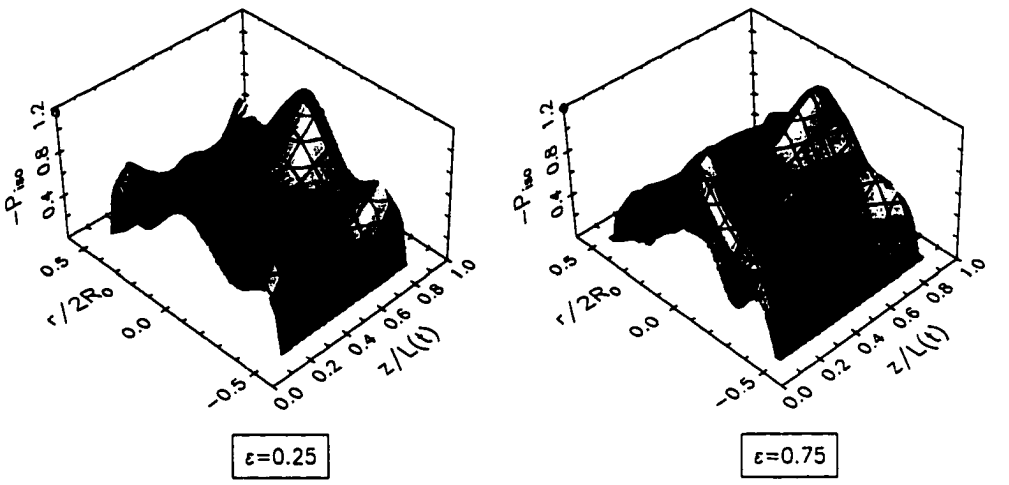

(a) Polydisperse melt

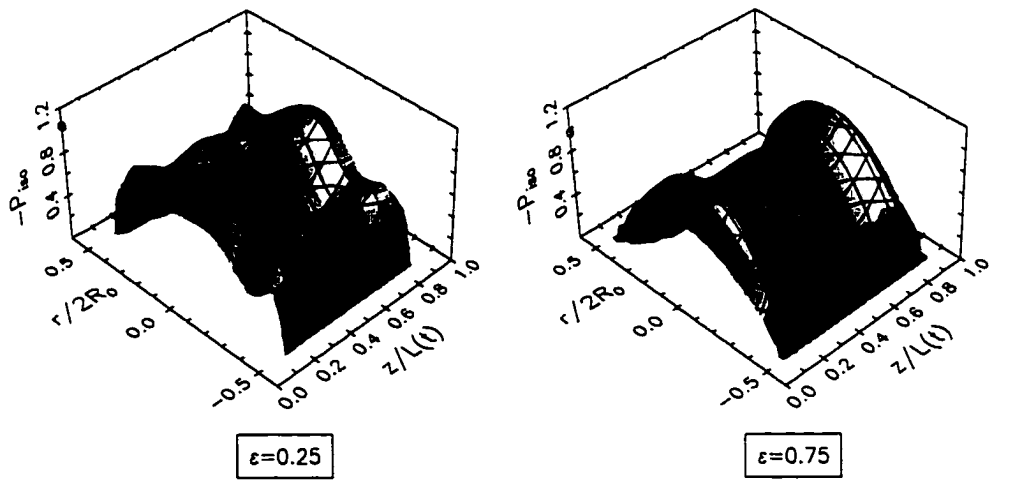

(b) Monodisperse melt

FIGURE 5.28: Isotropic stress within melt filaments in $\dot{\varepsilon}_0 = 0.02$ simulations.

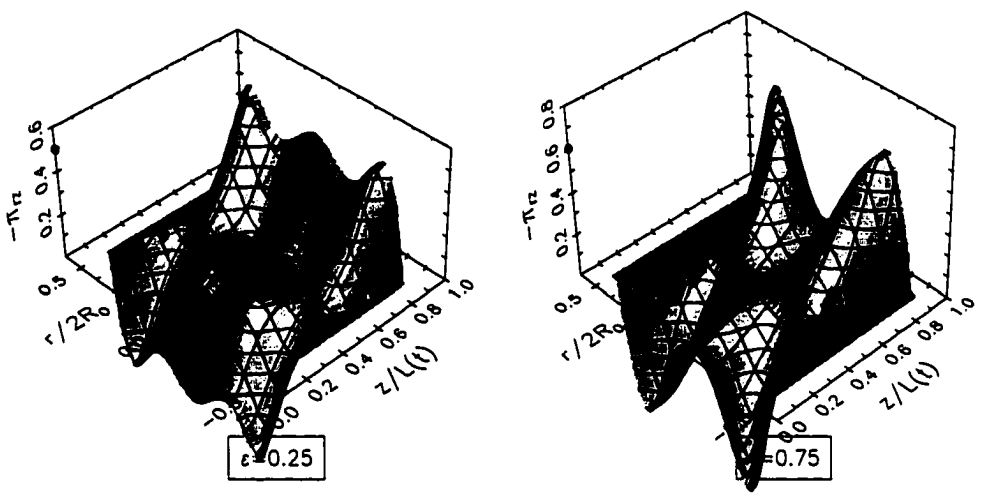

(a) Polydisperse melt

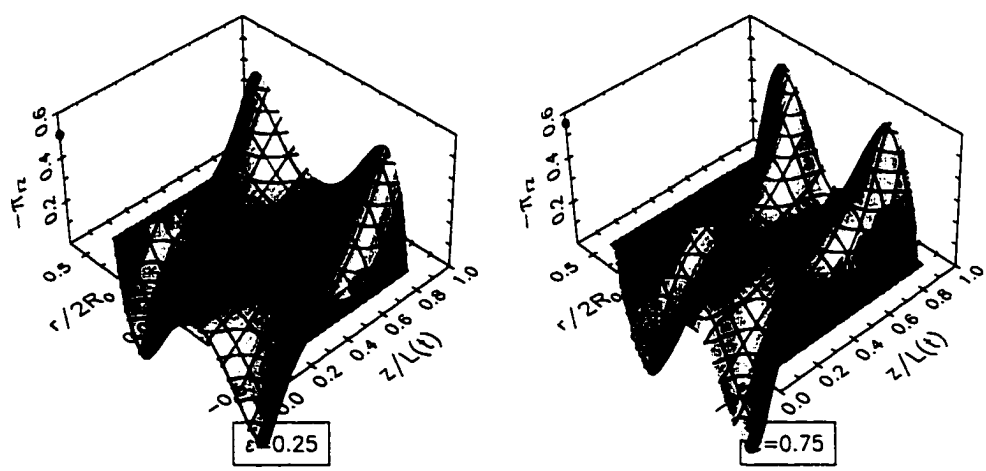

(b) Monodisperse melt

FIGURE 5.29: Shear stress within melt filaments in $\dot{\varepsilon}_0 = 0.02$ simulations.

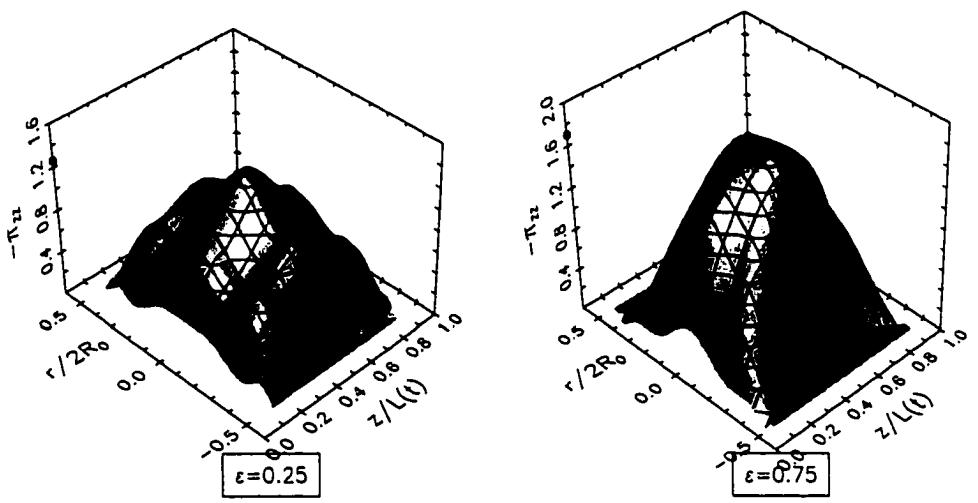

(a) Polydisperse melt

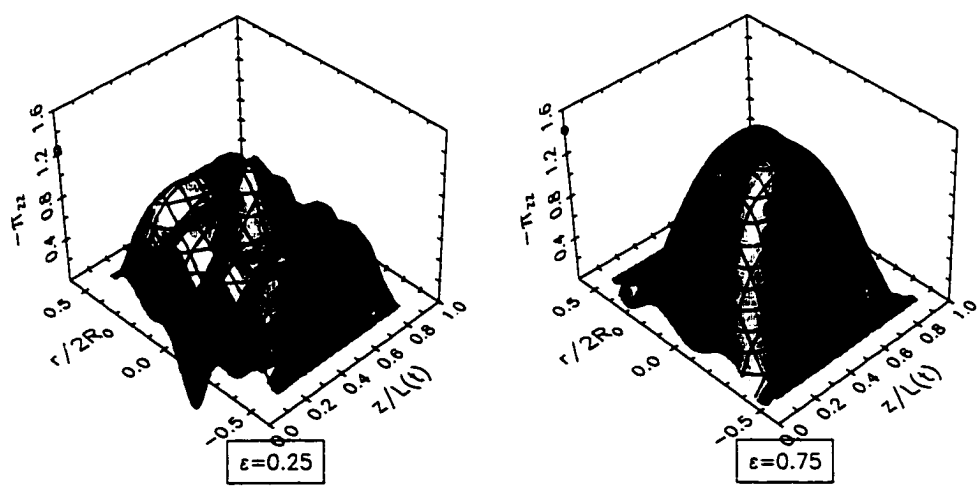

(b) Monodisperse melt

FIGURE 5.30: Axial component of the total extra stress tensor within melt filaments in $\dot{\varepsilon}_0 = 0.02$ simulations.

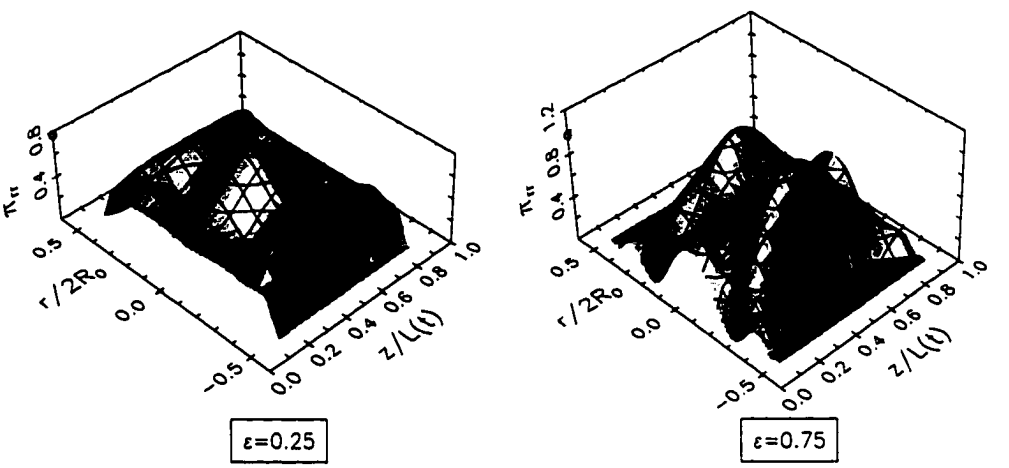

(a) Polydisperse melt

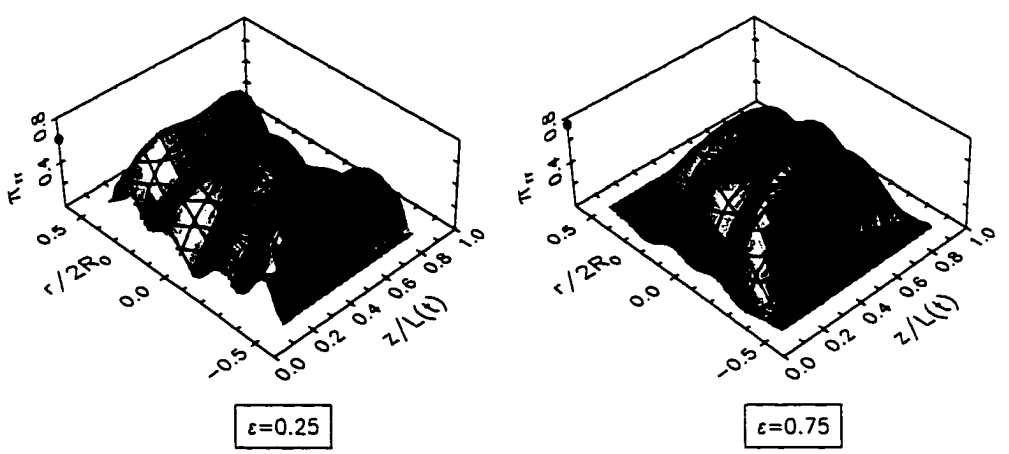

(b) Monodisperse melt

FIGURE 5.31: Radial component of the total extra stress tensor within melt filaments in $\dot{\epsilon}_0 = 0.02$ simulations.

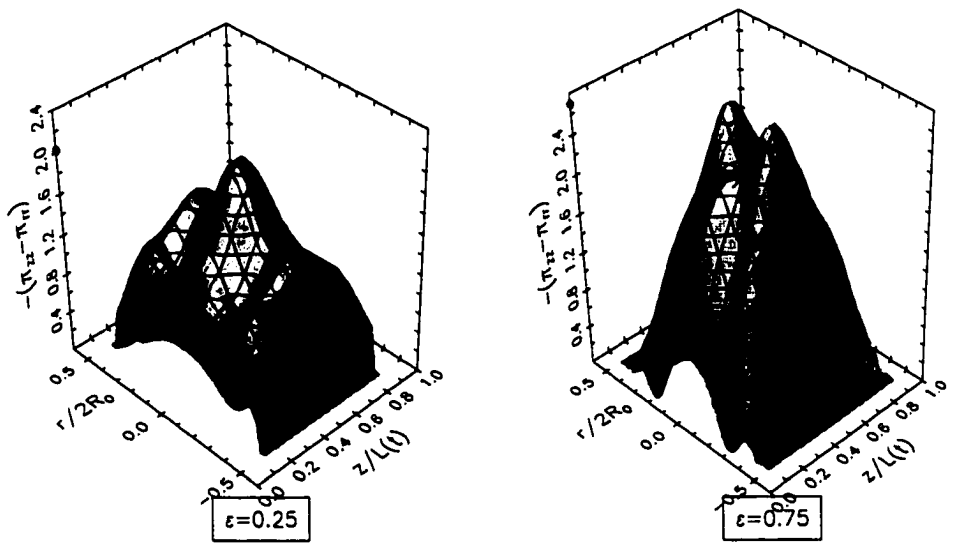

(a) Polydisperse melt

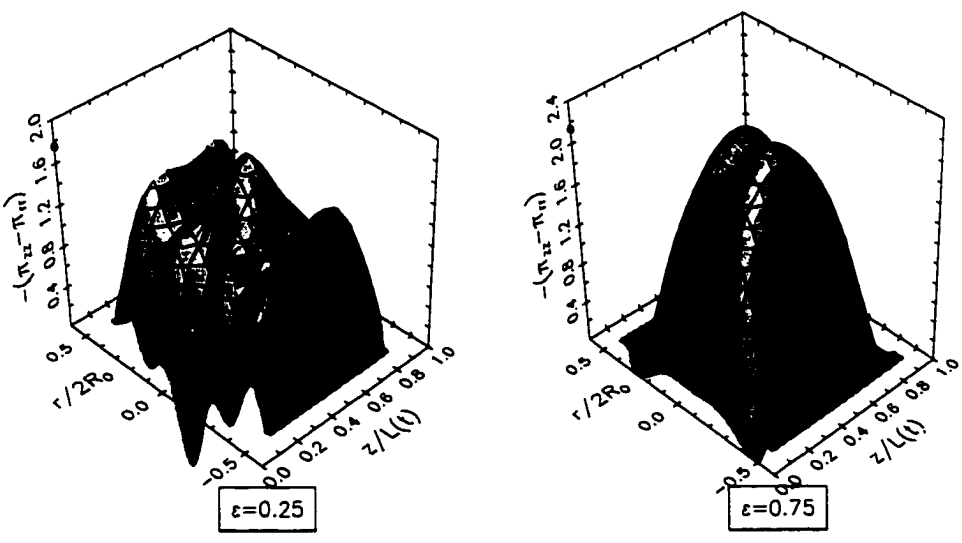

(b) Monodisperse melt

FIGURE 5.32: Normal stress difference within melt filaments in $\dot{\varepsilon}_0 = 0.02$ simulations.

across mid-plane of the melt filaments. This behavior can be contrasted to the case of the solution filament where the main contribution to the surface layer comes from the axial component of the stress tensor.

The distribution of shear stress within melt filaments is qualitatively similar to distributions observed in other cases, especially at small Hencky strains. At higher strains the central part along the axis of the filaments is free from shear deformations.

5.3.2 Elongational Viscosity

The transient Trouton ratio for the two model melts, determined from the simulation of filament stretching at an overall stretching rate $\dot{\varepsilon}_0 = 0.02$, is shown in Fig. 5.33. Except at the very beginning of deformation, $\varepsilon \lesssim 0.5$, the variation

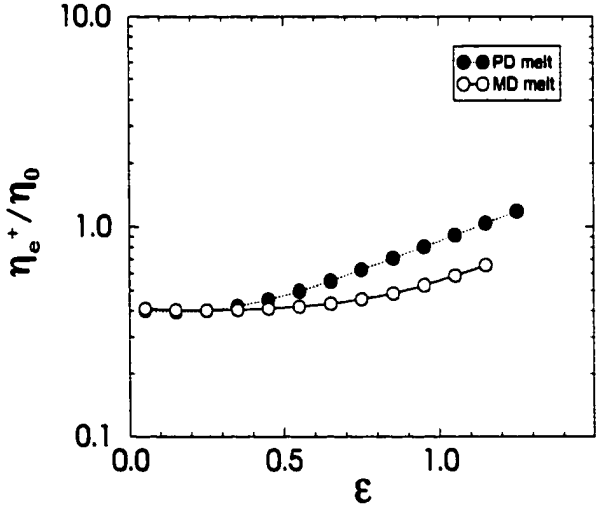

FIGURE 5.33: Trouton ratio for the model melts in $\dot{\varepsilon}_0 = 0.02, De \approx 10$ simulation

of Trouton ratios for the model polymer melts is in a very good qualitative agreement with the experimental results obtained by Tirtaadmadja and Sridhar (1993) [10] for shear-thinning semi-dilute solutions. The qualitative similarity in uniaxial extensional viscosities between shear-thinning polymer solutions and melts is in agreement with experimental observations (Sridhar *et al.* (1991) [4]).

5.4 Flow Reversal in Uniaxial Stretching Experiment

To conclude, we present our findings on a possible physical mechanism underlying the accelerated thinning of the fluid filament in the filament stretching experiment, found by Shipman *et al.* (1991) [15] in a numerical simulation of a Sridhar *et al.* (1991) [4] experiment. In presence of gravity, the surface tension of the fluid was found to be able to generate a reverse flow within the filament. The reverse flow first appeared next to the stationary end-plate and later migrated toward the center of the filament. The phenomenon was accompanied by a change in the pressure gradient across the stationary end-plate. The pressure was initially low in the center and high along the edge; the reverse was true in the later stages of deformation as the reverse flow developed. The phenomenon was later found in a numerical simulation of uniaxial stretching of Newtonian liquid filaments by Gaudet *et al.* (1996) [16] and experimental measurements of the velocity field within stretching Newtonian and non-Newtonian fluid filaments by Kröger and Rath (1995) [8]. However in both works the uniaxial deformations generated

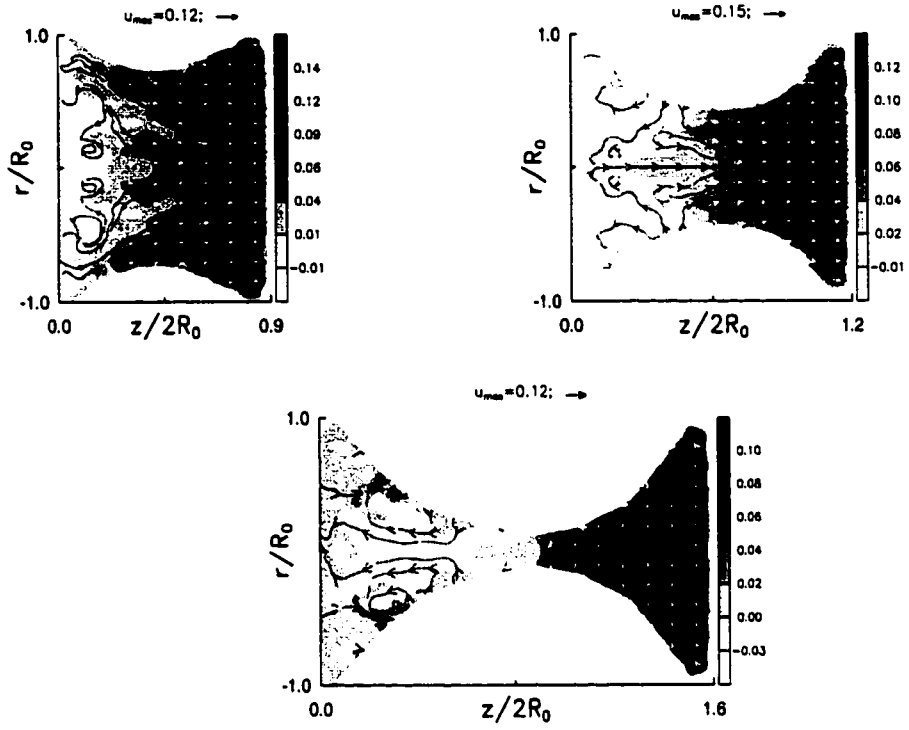

FIGURE 5.34: Velocity fields inside monatomic fluid undergoing undergoing uniform stretching; $v_0 = 0.1$.

by a uniformly moving end-plate were investigated and the flow reversal was found in the late stages of deformation characterized by a highly developed neck in the mid-filament region. The molecular dynamics simulations of the experiments with one uniformly moving end-plate, with both Newtonian and non-Newtonian model fluid filaments, give the spatial and temporal variation of the velocity field within the filament in excellent qualitative agreement with the Shipman *et al.* prediction. A typical example is presented in Fig. 5.34 where the velocity fields within monatomic Lennard-Jones fluid filament are shown. With an appropriate defini-

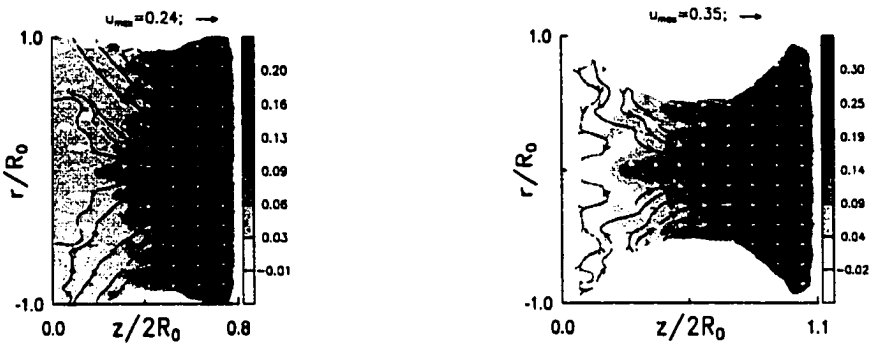

FIGURE 5.35: Velocity fields inside monatomic fluid undergoing a constant imposed stretching rate deformation; $\dot{\varepsilon}_0 = 0.014$.

tion of the capillary number [16]

$$Ca = \frac{\eta_0}{\alpha} v_0 \tag{5.2}$$

the simulation is characterized by $Ca = 0.7$, which corresponds to the constant velocity of the moving end-plate, $v_0 = 0.1$ Lennard-Jones units. In addition to qualitative description of the fields by streamlines, the magnitudes of Eulerian velocities represented by the arrows and the distribution of the axial component, u_z, of the fluid velocity represented by the contour plots are given. Unlike the work cited above, we observe flow reversal from the outset.

However, in simulations using the same fluid in experiments in which one end-plate moves with an exponentially increasing velocity, as in the Shipman *et al.* simulation, we do not observe the flow reversal phenomenon, except possibly at large Hencky strains just prior to breakup of the filament. The velocity fields within the filament are presented in Fig. 5.35 for the simulation characterized by the capillary

number (as defined in eq. (3.9)) $Ca = 1.1$, overall stretching rate $\dot{\varepsilon}_0 = 0.014$ and the initial velocity $v_0 = 0.2$. Since we have not performed simulations at lower capillary numbers our results do not exclude the possibility of the flow reversal in constant imposed stretching rate experiments. Rather they indicate that, in the absence of gravity, the phenomenon is not generally responsible for the initial thinning of the fluid filament at a rate exceeding the imposed stretching rate.

The effect is plausible in the deformations of the fluid filaments generated by the uniform motion of one of the end-plates since in this case the viscous effects are important only at the beginning of deformation.

6 Conclusions

In this work we have presented molecular dynamics simulation of extending liquid bridges with simple microscopic model fluids, whose design incorporates the most essential physics necessary to reproduce the generic properties of Newtonian and non-Newtonian polymeric liquids. Besides nicely complementing numerical simulations based on constitutive models of liquid rheology in elucidating the underlying dynamics of experimentally observed phenomena, the molecular dynamics simulations have a far-reaching goal of providing a truly microscopic insight into origins of macroscopic phenomena. Within the limited scope of the present simulation we have demonstrated that many aspects of fluid response to stretching deformation induced by the motion of the solid end-plates in liquid bridge configuration are reproduced on microscopic scale in both Newtonian and polymeric fluid samples. In particular quantitative agreement with experimental observations has been found at early stages of deformation, characterized by the variation of the minimum radius of the fast thinning filaments, for all fluids

investigated. The response can be adequately described by a lubrication approximation of Newtonian 'reverse squeeze flow', as demonstrated by Spiegelberg *et al.* (1996) [11]. The time variation of the tensile force applied on the end-plates in order to sustain stretching deformation at a constant stretching rate was found to be in excellent qualitative agreement with experimental observations for all fluid models. As a consequence, the Trouton ratio, which characterizes fluid response to transient uniaxial extensional deformation and is determined from the minimum radius and tensile force measurements, was found to be in good qualitative agreement with experimental data as well. In view of the simplicity of the models, perhaps the most surprising aspect of the simulation is the strain-hardening response of the model solution, which is characteristic of constant shear viscosity dilute polymer solutions (Boger fluids). Our results support the idea that a very uniform flow field results from the increased alignment of the long polymer molecules, which in the particular process investigated in this work, leads to the formation of an axially very uniform deformation over most of the flow regime. The molecular dynamics simulation offers insight into aspects of the dynamics of deformation which are experimentally largely inaccessible, such as the flow kinematics within the deforming filament and the accompanying stress distributions.

Investigations of these aspects of the filament stretching device have been scarce even in the numerical simulations of the device based on constitutive models appropriate for particular fluids. The most detailed study was performed by Yao and

McKinley (1998) [18] on an Oldroyd-B model for dilute polymer solutions. In the range of Hencky strains achievable in our simulations excellent agreement with their results was found for the axial variation of the axial component of the flow field for both Newtonian and solution filaments. Broad qualitative agreement was found for the distributions and time variation of the shear and axial components of the extra stress tensor given in [18]. We have been able to give a very detailed description of the complete stress tensor within fluid filaments. While we consider it a welcome insight into the complex response of Newtonian and non-Newtonian fluids to uniaxial stretching deformation these results should be treated cautiously due to limited temporal and spatial resolution of our simulations, as well as the inherently noisy nature of stress data. A more accurate description could be obtained in larger scale molecular dynamics simulations involving large configurations and large statistical ensembles of dynamically equivalent states originating from different equilibrium configurations.

We touched upon an interesting aspect of the underlying dynamics of the filament stretching deformation obtained in the numerical simulation of Oldroyd-B fluids by Shipman *et al.* (1991) [15]. They found that the initial accelerated thinning of the fluid filament was caused by the reversed flow which, in the beginning of deformation, develops near the end-plates. The reverse flow patterns were found in experiments (Kröger *et al.* (1995) [8]) and numerical simulations (Gaudet *et al.* (1996) [16]) of filament stretching generated by uniformly separating end-plates

characterized by a small capillary numbers. However similar findings have neither been reported nor discussed in subsequent research of the filament stretching device with exponentially separating end-plates. Although our simulations do not support occurrence of reversed flows in the experiments with exponentially separating end-plates at relatively high stretching rates, they indicate the existence of flow reversal in the type of filament stretching experiments studied by Kröger *et al.* [8] and Gaudet *et al.* [16].

We believe that the results of this simulation offer grounds for optimism for further application of molecular dynamics techniques in the field of extensional rheometry. In particular, the simulation provides groundwork for simulations of other experimental techniques based on liquid bridge configurations. The simulation of the version of the filament stretching experiment with an adjustable diameter of the moving end-plates is straightforward, as is the simulation of the stress relaxation experiment. The use of larger simulated configurations, accompanied by more refined model fluids, and possibly more sophisticated numerical algorithms, will immensely help our understanding of the breakup mechanisms of fluid filaments. Moreover the merits of different experimental techniques in determining the extensional properties of fluids can be reliably determined from the comparison with the results for model fluids, which can be obtained from easily realized nonequilibrium molecular dynamics simulations of pure extensional flows.

References

[1] R. B. Bird, R. C. Armstrong, and O. Hassager, *Dynamics of Polymeric Liquids*, vol. 1, Wiley, New York, 2nd ed., 1987.

[2] C. Macosko, *Rheology: Principles, Measurement and Applications*, VCH, New York, 1993.

[3] M. P. Allen and D. J. Tildesley, *Computer Simulations of Liquids*, Clarendon Press, Oxford, 1987.

[4] T. Sridhar, V. Tirtaatmadja, D. A. Nguyen, and R. K. Gupta, "*Measurement of extensional viscosity of polymer solutions*", J. Non-Newtonian Fluid Mech. **40**, 271 (1991).

[5] F. N. Cogswell, Plast. Polym. **36**, 109 (1968).

[6] J. E. Matta and R. P. Tytus, "*Liquid stretching using a falling cylinder* ", J. Non-Newtonian Fluid Mech. **35**, 215 (1990).

[7] R. Kröger, S. Berg, A. Delgado, and H. J. Rath, "*Stretching behaviour of large polymeric and Newtonian liquid bridges in plateau simulation*", J. Non-Newtonian Fluid Mech. **45**, 385 (1992).

[8] R. Kröger and H. J. Rath, "*Velocity and elongation rate distributions in stretched polymeric and Newtonian large bridges*", J. Non-Newtonian Fluid Mech. **57**, 137 (1995).

[9] S. Berg, R. Kröger, and H. J. Rath, "*Measurement of extensional viscosity by stretching large bridges in microgravity*", J. Non-Newtonian Fluid Mech. **55**, 307 (1994).

[10] V. Tirtaatmadja and T. Sridhar, "*A filament stretching device for measurement of extensional viscosity*", J. Rheol. **37**, 1081 (1993).

[11] S. H. Spiegelberg, D. C. Ables, and G. H. McKinley, "*The role of end-effects on measurements of extensional viscosity in filament stretching rheometers*", J. Non-Newtonian Fluid Mech. **64**, 229 (1996).

[12] M. J. Solomon and S. J. Muller, "*The transient extensional behavior of polystyrene-based Boger fluids of varying solvent quality and molecular weight*", J. Rheol. **40**, 837 (1996).

[13] J. van Nieuwkoop and M. M. O. Muller von Czernicki, "*Elongation and Subsequent Relaxation Measurements on Dilute Polyisobutylene Solutions*", J. Non-Newtonian Fluid Mech. **67**, 105 (1996).

[14] H. Chang and A. S. Lodge, "*A possible mechanism for stabilizing elongational flow in certain polymeric liquids at constant temperature and composition*", Rheol. Acta **10**, 448 (1971).

[15] R. W. G. Shipman, M. M. Denn, and R. Keunings, "*Mechanics of the "falling plate" extensional rheometer*", J. Non-Newtonian Fluid Mech. **40**, 281 (1991).

[16] S. Gaudet, G. H. McKinley, and H. A. Stone, "*Extensional Deformation of Newtonian Liquid Bridges*", Phys. of Fluids **8**, 2568 (1996).

[17] R. Sizaire and V. Legat, "*Finite element simulation of a filament stretching extensional rheometer*", J. Non-Newtonian Fluid Mech. **74**, 47 (1998).

[18] M. Yao and G. H. McKinley, "*Numerical simulation of extensional deformations of viscoelastic liquid bridges in filament stretching devices*", J. Non-Newtonian Fluid Mech. **74**, 47 (1998).

[19] P. Szabo, "*Transient filament stretching rheometer I: Force Balance Analysis*", Rheol. Acta **36**, 277 (1997).

[20] M. I. Kolte, H. K. Rasmussen, and O. Hassager, "*Transient filament stretching rheometer*", Rheol. Acta **36**, 285 (1997).

[21] M. Yao, S. H. Spiegelberg, and G. H. McKinley, "*Dynamics of Weakly Strain-Hardening Fluids in Filament Stretching Devices*", J. Non-Newtonian Fluid Mech. **80**, 345 (2000).

[22] S. Hess, "*Rheological Properties via Nonequilibrium Molecular Dynamics: from Simple towards Polymeric Liquids*", J. Non-Newtonian Fluid Mech. **23**, 305 (1987).

[23] A. Berker, S. Chynoweth, U. C. Klomp, and Y. Michopoulos, "*Non-equilibrium Molecular Dynamics (NEMD) Simulation and Rheological Properties of Liquid n-Hexadecane*", J. Chem. Soc. Faraday Trans. **88(13)**, 1719 (1992).

[24] M. Kröger, W. Loose, and S. Hess, "*Rheology and structural changes of polymer melts via nonequilibrium molecular dynamics*", J. Rheol. **37**, 1057 (1993).

[25] M. Kröger and S. Hess, "*Rheological evidence for a dynamical crossover in polymer melts via Nonequilibrium Molecular Dynamics*", Phys. Rev. Lett. **85**, 1128 (2000).

[26] H. R. Warner, Ind. Engng. Chem. Fund. **11**, 379 (1972).

[27] K. Kremer and G. S. Grest, "*Dynamics of entangled linear polymer melts: A molecular-dynamics simulation*", J. Chem. Phys, **92**, 5057 (1990).

[28] F. Bueche, *Physical Properties of Polymers*, Interscience, New York, 1962.

[29] J. Gao and J. H. Weiner, "*Screened Intermolecular Forces and Covalent Bond Forces in Polymer Melts*", J. Chem. Phys. **98**, 8256 (1993).

[30] J. Gao and J. H. Weiner, "*Nature of Stress on the Atomic Level in Dense Polymer Systems*", Science **266**, 748 (1994).

[31] J. Yang, J. Koplik, and J. R. Banavar, "*Terraced spreading of simple liquids on solid surfaces*", Phys. Rev. A **46(12)**, 7738 (1992).

[32] B. Dünweg and K. Kremer, *"Microscopic Verification of Dynamic Scaling in Dilute Polymer Solutions: A Molecular-Dynamics Simulation"*, Phys.Rev.Lett. **61**, 2996 (1991).

[33] A. W. Lees and S. F. Edwards, *"The computer study of transport processes under extreme conditions"*, J.Phys. C **5**, 1921 (1972).

[34] D. J. Evans, *"The frequency dependent shear viscosity of methane"*, J. Chem. Phys. **37**, 1745 (1979).

[35] D. J. Evans and G. P. Morriss, *Statistical Mechanics of Nonequilibrium Liquids*, Academic, London, 1990.

[36] J. H. Irving and J. G. Kirkwood, *"The Statistical Mechanical Theory of Transport Processes. IV. The Equations of Hydrodynamics"*, J. Chem. Phys. **18**, 817 (1950).

[37] J. S. Rowlinson and B. Widom, *Molecular Theory of Capillarity*, Oxford University Press, Oxford, 1982.

[38] D. J. Evans and B. L. Holian, *"The Nose-Hoover thermostat"*, J. Chem. Phys. **83**, 4069 (1985).

[39] M. Doi and S. F. Edwards, *The Theory of Polymeric Dynamics*, Clarendon Press, Oxford, 1986.

[40] R. I. Tanner, *Engineering Rheology*, Clarendon Press, Oxford, 1988.

[41] K. Kremer and G. S. Grest, *"Molecular Dynamics Simulation for Polymers in the Presence of a Heat Bath"*, Phys. Rev. A **33**, 3628 (1986).

[42] J. N. Israelachvili, *Intermolecular and Surface Forces*, Academic, London, 1985.

[43] J. Koplik, J. R. Banavar, and J. F. Willemsen, *" Molecular Dynamics of Fluid Flow at Solid Surfaces"*, Phys. Fluids A **1 (5)**, 781 (1989).

[44] J. Koplik and J. R. Banavar, " *Reentrant Corner Flows of Newtonian and non-Newtonian fluids*", J. Rheol. **41(3)**, 787 (1997).

[45] B. D. Todd, D. J. Evans, and P. J. Daivis, "*Pressure tensor for inhomogeneous fluids*", Phys. Rev. A **52**, 1627 (1995).

[46] J. Koplik and J. R. Banavar, "*Continuum Deductions from Molecular Hydrodynamics nonequilibrium molecular dynamics*", Annu. Rev. Fluid Mech. **27**, 257 (1995).

[47] C. W. Gear, *Numerical Initial Value Problems in Ordinary Differential Equations*, Prentice-Hall, Englewood Cliffs, NJ, 1971.

[48] W. F. van Gunsteren and H. J. C. Berendsen, "*Algorithms for macromolecular dynamics and constraint dynamics*", Molecular Phys. **34**, 1311 (1977).

[49] D. J. Evans and G. P. Morriss, "*Non-equilibrium molecular dynamics*", Comput. Phys. Rep. **1**, 297 (1984).

[50] P. Dierckx, *Curve and Surface Fitting with Splines*, Oxford University Press, New York, Oxford, 1993.

[51] F. T. Trouton, "*On the Coefficient of Viscous Traction and its Relation to that of Viscosity*", Proc. R. Soc. A **77**, 426 (1906).